UNIVERSITAT POLITÈCNICA DE CATALUNYA BARCELONATECH

Exploring flatland nano-optics with graphene plasmons

by

Achim Woessner

Exploring flatland nano-optics with graphene plasmons

by

Achim Woessner

Thesis Advisor:
Prof. Dr. Frank H.L. Koppens

ICFO – Institut de Ciències Fotòniques
UPC – Universitat Politècnica de Catalunya

May 2017

Thesis committee:

Prof. Dr. Harald Giessen (University of Stuttgart, Germany)
Prof. Alexey Kuzmenko (University of Geneva, Switzerland)
Prof. Dr. Javier García de Abajo (ICFO – Institut de Ciències Fotòniques, Spain)

Contents

Preface

Plasmons are charge oscillations coupled to electromagnetic radiation. One of their most intriguing properties is their deep subwavelength confinement resulting in strongly enhanced light-matter interaction.[1,2] Metal plasmons have received tremendous interest over the last few decades[3] and have sparked the development of a range of new fields such as plasmonic nanophotonic components,[4] metamaterials,[5] metasurfaces[6] and more exotic research areas such as quantum plasmonics.[7] Some of the main drawbacks of conventional metal plasmonics are that the plasmon lifetime is extremely short when the light is confined to deep subwavelength scales and that their properties are not tunable *in situ*.[8,9]

This is where graphene, a one atom thick semimetal consisting of carbon atoms arranged in a two dimensional honeycomb lattice, comes into play.[10] In graphene, plasmons can be confined to extreme subwavelength scales while still having a long lifetime and their wavelength is tunable *in situ*.[8] Graphene plasmonics is a relatively new research area but has already attracted a lot of attention.[11–17] This is undoubtedly due to the fact that graphene plasmons are extremely versatile. They are a unique platform for exploring the limits of light-matter interaction,[12,18,19] two dimensional transformation optics,[20] biosensing,[21] and mid-infrared integrated optics.[11] Their first technological applications have already been shown by using them to tune the output frequency of quantum cascade lasers.[22,23]

At the start of my work on this thesis at the end of 2012 the research area of graphene plasmonics was just in the beginning, especially concerning experiments. A vast amount of theoretical work was already available on general graphene plasmonics.[8,18,24–26] Based on these fundamental studies the first theoretical proposals for exploiting graphene plasmons in unique devices appeared. Graphene plasmonic circuits have been proposed as building blocks for optical signal processing.[20,27] Also more exotic proposals such as two dimensional transformation optics[20] and single photon non-linearities[28] were appearing. However experiments were just starting to catch up with these theoretical proposals. Earlier published work showed both propagating[29,30] as well as localized graphene plasmons.[31,32] However the plasmon lifetime was well below what was expected from theoretical studies[8,18] and there was a big debate in the community about the origin of this discrepancy.[32,33] Without the anticipated long plasmon lifetime a lot of the device proposals were not feasible. This is why the search for a longer plasmon lifetime was a very important topic in the graphene plasmon community.

Luckily around the same time a new layered material, hexagonal boron nitride (h-BN), entered the stage.[34,35] Graphene encapsulated by h-BN shows far superior carrier lifetime compared to the previously used silicon dioxide substrate.[34,35] Indeed for graphene fully encapsulated by h-BN the transport carrier lifetime reached its absolute limit at room temperature. The limitation is acoustic graphene phonons, or in other words: charge carriers scattering off the vibrations of the graphene lattice itself.[35] It was however not clear how this increase in transport carrier lifetime would translate to the lifetime of plasmons, charge oscillations at much higher frequencies.

The goal of this thesis is to explore the frontiers of graphene plasmonics both to under-

stand the fundamental properties and limitations as well as to use the gained understanding to develop new concepts towards applications. For the studies presented here I mainly used scattering-type scanning near-field optical microscopy (s-SNOM)[29,30,36] as well as a technique based on s-SNOM we developed called near-field photocurrent nanoscopy. These techniques provide great insight into the working mechanisms of graphene plasmons and graphene opto-electronics with a nanometer resolution over a broad frequency range from the mid-infrared to the terahertz. Their main advantage compared to other techniques is that they allow to perform measurements in real space rather than frequency space which makes for easy and straight forward interpretation of the data. Moreover the fact that in principle no nano structuring of the devices is necessary allows the direct study of the plasmonic properties without them being affected by fabrication imprecisions, contaminations and artifacts.

With these tools and the h-BN material system at hand we set out to explore what was possible with graphene plasmons.

Outline

This thesis is split into a general introduction chapter and two main parts with experimental results. In the beginning I will give an introduction to graphene and its opto-electronic properties, graphene devices and their fabrication. Furthermore hexagonal boron nitride (h-BN), a dielectric layered material commonly used as substrate for graphene, is introduced (Chapter 1). In the first main part of the the background and fundamentals of graphene plasmons needed for the subsequent experimental chapters are introduced (Chapter 2). This is followed by a chapter where I introduce an experiment exploring the limitations of the graphene plasmon lifetime at room temperature for graphene encapsulated in h-BN (Chapter 3). I will then show an optical phase modulator which is capable of tuning the phase *in situ* from 0 to 2π with a footprint of only 350 nm exploiting the unique capability of tuning the graphene plasmon wavelength (Chapter 4). In the second part of the thesis I will give a background on photodetection with graphene (Chapter 5). I will then introduce a new measurement technique called infrared photocurrent nanoscopy (Chapter 6) and show how it can be used to study the opto-electronic properties of a variety of graphene devices in the infrared at the nanoscale (Chapter 7). Then I will show how graphene plasmons can be detected electrically using this technique, which constitutes a first step in engineering fully on-chip graphene plasmonic circuits (Chapter 8). As the last chapter of this part I will introduce a way of detecting phonon polaritons in hexagonal boron nitride electrically using graphene and show how this can be used to greatly enhance the photoresponse of graphene photodetectors in the mid-infrared (Chapter 9). Finally I will provide a summary of the achievements of this thesis and an outlook (Chapter 10).

1. Basic opto-electronic properties of graphene and hexagonal boron nitride

In this chapter gives a general overview of the properties of graphene, with a focus on its electronic and especially opto-electronic properties. The basic properties that govern the way graphene behaves when you shine light on it and how light is absorbed are introduced. A special focus is put on its optical conductivity and the different models used to describe it. An advanced fabrication method of ultra clean graphene devices is presented and compared to previously used techniques. Furthermore the optical properties of hexagonal boron nitride, the substrate of choice for high quality graphene devices, are introduced.

Graphene is a one-atom thick semimetal which is arranged in a two dimensional honeycomb lattice of sp^2 hybridized carbon atoms (Fig. 1.1a).[37] It attracted a lot of attention right after it was isolated for the first time by Andre Geim and Kostya Novoselov in 2004[38] as it has many unique properties. Geim and Novoselov consequently won the Nobel prize in Physics for their "for groundbreaking experiments regarding the two-dimensional material graphene" in 2010.[39,40]

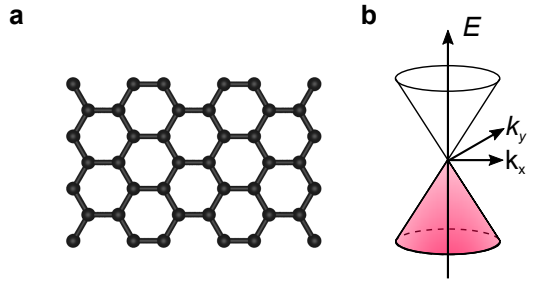

Fig. 1.1.: Graphene lattice and electron dispersion of graphene. **a**, The graphene lattice consists of carbon atoms arranged in a hexagonal honeycomb structure. The position of carbon atoms are shown as disks and the bonds as lines. **b**, Graphene electron dispersion showing the typical Dirac cone, indicating that graphene is a zero gap two dimensional semimetal. The colour indicates that the valence band is filled up to the charge neutrality point and that the Fermi energy $E_F = 0\,\text{eV}$.

As the energy-momentum dispersion of graphene is linear for small energies (Fig. 1.1b) charge carriers in graphene have zero effective mass, or in other words behave as massless particles. The carrier dynamics can therefore be described by a massless Dirac equation and charge carriers in graphene are often referred to as massless Dirac fermions[41,42] with the charge carrier Fermi velocity $v_F \approx c/300$, where c is the speed of light in vacuum.[37] In the energy-momentum dispersion of graphene the valence and conduction band touch at a point known as the Dirac point and thus graphene can be referred to as a zero-gap semiconductor or a zero-overlap semimetal.[10] In graphene the Fermi energy E_F with respect to the Dirac point can be tuned by changing the carrier density n_s:[37]

$$E_F = \hbar v_F k_F = \hbar v_F \sqrt{\pi n_s} \tag{1.1}$$

here $\hbar$ is the reduced Planck constant and k_F the Fermi wavevector.

1.1. Transport properties of graphene

Fig. 1.2a shows a sketch of a typical graphene device. In the depicted two-probe configuration the electric current between source (S) and drain (D) can be measured, typically using a current amplifier. The carrier density n_s of the graphene can be tuned *in situ* by applying a backgate voltage V_{BG} between a layer of highly conductive silicon (Si^{++}) and the graphene. The applied voltage will drop over the substrate dielectric (here SiO_2) and due to the backgate Si^{++} and the graphene forming a plate capacitor charge carriers will accumulate in the graphene as a function of the applied V_{BG}. We can calculate n_s due to

this capacitive effect as a function of applied V_{BG} using a simple plate capacitor model for the system:

$$n_s = \sqrt{((V_{BG} - V_0)C_{ox}/e)^2 + n_0^2}, \tag{1.2}$$

where V_{BG} is the applied backgate voltage. V_0 is the backgate voltage at which the charge neutrality point appears and is introduced phenomenologically. It represents the voltage needed to overcome intrinsic doping of the graphene from different origins. $C_{ox} = \varepsilon_0\varepsilon_{sub}/t_{sub}$ is the capacitance of the substrate which depends on the DC permittivity ε_{sub} and the thickness t_{sub} of the substrate and ε_0 is the free space permittivity. e is the elementary charge and n_0 is the phenomenologically introduced residual carrier density at the charge neutrality point which depends on the graphene quality and mobility. Thus for 300 nm SiO_2 substrates which typically allow the application of voltages of up to $V_{BG} = \pm 100\,V$ before they break due to leakage Fermi energies of $E_F = \pm 0.3\,eV$ are feasible.

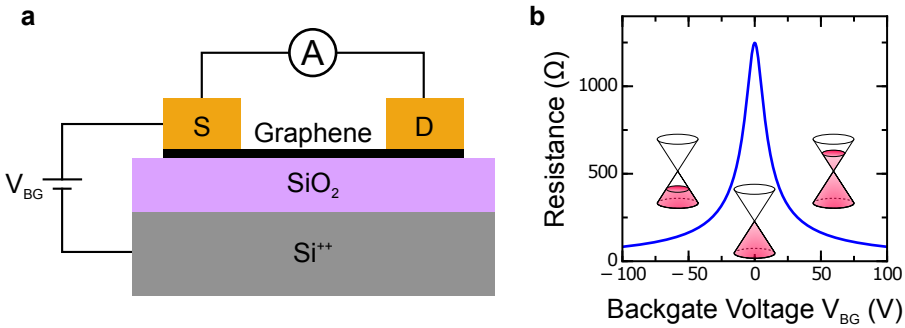

Fig. 1.2.: Typical graphene device and backgate dependent resistance. **a** A typical two probe graphene device schematic with a highly doped Si backgate to tune the carrier density in graphene. The carrier density and thus the resistance can be tuned in graphene by applying an electrostatic voltage to a graphene device. **b** Ambipolar electric field effect in graphene.[10] The inset shows the change of the Fermi energy E_F by changing the backgate voltage V_{BG}. In this case a charge carrier mobility of μ =10 000 $cm^2\,V^{-1}\,s^{-1}$ was used.

We can then calculate the conductivity of graphene using $\sigma = n_s e\mu$ with μ being the charge carrier mobility of the graphene. In Fig. 1.2b the resistance R of the graphene is then calculated using:

$$R = \frac{L}{W\sigma} \tag{1.3}$$

where L is the channel length and W the width. For this we assume a constant mobility μ with carrier density, which is not fully justified (see section 1.1.1).

As shown before the carrier density n_s in graphene can be tuned *in situ* by the electric field effect continuously from electron to hole doping. This means it is possible to add electrons or holes to the graphene, or in other words dope the graphene as E_F depends on n_s (eq. (1.1)). Fig. 1.2b shows the simple case of the electric field effect where the resistance of a graphene sheet changes by applying different V_{BG}. At the Dirac point, or charge neutrality point, the resistance of the device is highest as the carrier density is lowest. As graphene does not have a bangdap the conductivity never drops to zero and

thus the resistance at the charge neutrality point is finite. The inset shows the changing E_F with changing V_{BG} from hole doping for negative V_{BG} over neutral graphene to electron doping at positive V_{BG}.

1.1.1. Graphene transport mobility

Charge carriers in graphene travel through the graphene lattice without any effective mass due to the energy-momentum dispersion of graphene. Their mobility is however limited. Charge carriers interact with phonons in the substrate and the graphene itself and can scatter with charged particles and other scattering centers.[43] These events limit the related transport mobility μ and scattering time τ_{scat}.

For different device geometries and substrates different scattering mechanisms are known to limit the mobility of graphene.[43] In order to differentiate between the different mechanisms temperature and carrier dependent measurements are the most common techniques.

Coulomb scattering is due the charge carriers scattering with charged impurities, typically due to long-range variations of the electrostatic potential. It is governed by the impurity density n_i. These type of impurities can be scattering centers in the graphene itself, in the substrate or trapped ions between graphene and substrate.[44] The scattering time scales with $\sqrt{n_s}/n_i$ and thus the mobility is independent of carrier density. The increased scattering time for increasing n_s is due to the increased screening of the charge carriers at higher carrier densities.[43,45] For long range charged impurity scattering it is possible to use substrates with higher permittivity to increase the screening and lower the Coulomb scattering.[44,45]

Short-range scattering is due to atomic scale neutral scatterers, e.g. lattice defects.[43] It is governed by the defect density n_d and the associated conductivity is independent of carrier density. It leads to a sublinear increase of the graphene conductivity with carrier density.[44] It has for example been observed in suspended graphene sheets at high carrier densities.[46]

Graphene acoustic phonons impose an intrinsic limit to the mobility by charge carrier scattering with the lattice vibrations of the graphene lattice itself.[47] In the absence of other scattering mechanisms this is the ultimate limit of the graphene mobility at room temperature. This mechanism shows a decrease of mobility with $1/n_s$,[47] which is in excellent agreement with measurements of graphene at high carrier density, encapsulated in hexagonal boron nitride (h-BN) by the van der Waals assembling technique described in sec. 1.3.1.[35] Acoustic phonon limited devices have shown ballistic transport at low temperatures over distances of more than ten micrometers.[35,48] For more details on the fabrication procedure and a short overview of its history see section 1.3.

1.2. Optical properties of graphene

Graphene is a broadband opitcal absorber due to its missing bandgap. Indeed graphene is well-known for absorbing 2.3% of the optical illumination from the ultraviolet to the near-infrared region of the spectrum.[49] This value is independent of material parameters and is thus often referred to as the universal optical absorption constant of graphene. It

is due to interband absorption of charge carriers in graphene. But much like the transport properties of graphene its optical properties can also be tuned *in situ* by changing n_s.[50,51]

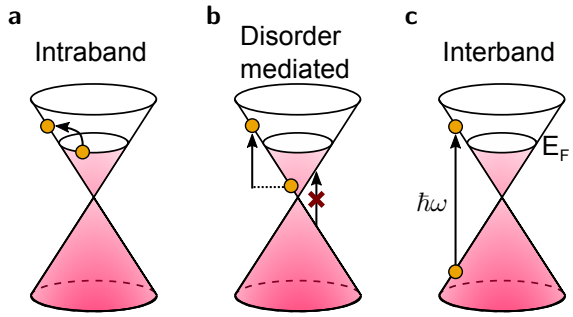

Fig. 1.3.: Optical absorption regimes of graphene. **a** In the intraband regime free carriers are responsible for the graphene absorption as described by the Drude response of graphene. **b** In the regime where no direct absorption of photons is allowed, due to Pauli blocking, disorder in the graphene can provide the necessary momentum to allow absorption. **c** In the interband regime the photon energy E_{ph} is high enough to allow direct absorption of photons.

For the optical absorption of plane waves in graphene three different regimes exist:[15]

Intraband: For a photon energy $E_{ph} = \hbar\omega \ll E_F$ and $\omega\tau \ll 1$ we are in the so called intraband absorption regime. In this case τ is the scattering time of graphene charge carriers. Here free carriers are responsible for the graphene absorption and the absorption is well described by a Drude response of the graphene. This absorption mechanism is mainly responsible for the absorption in the terahertz frequency regime.[52] (Fig. 1.3a)

Disorder mediated: When $E_{ph} < 2E_F$ a direct transition of an electron from the valence to the conduction band and thus the absorption of a photon is not allowed due to the Pauli exclusion principle. Graphene is said to be in the Pauli blocking regime. However a photon can still be absorbed when the necessary momentum is provided by disorder in the graphene. This leads to a non-zero absorption for low quality graphene[50,51] and the residual absorption is greatly reduced for high quality encapsulated graphene, such as the one described in the following section 1.3. (Fig. 1.3b)

Interband: When $E_{ph} > 2E_F$, photons can be absorbed directly in the graphene by promoting an electron from the valence to the conduction band which leads to the universal graphene absorption of 2.3% described above. It is important to note that this universal absorption value is only valid for free standing graphene. Graphene on a substrate can have greatly different values of absorption due to thin film interference effects.[53,54] In fact, interference is responsible for seeing single layer graphene so nicely under a microscope on the typical 300 nm SiO_2 substrates.[55] (Fig. 1.3c)

1.2.1. Optical conductivity

The processes qualitatively described above can be described mathematically by the so-called optical conductivity function of graphene. The optical conductivity of graphene is at the heart of many calculations in the following chapters. Here I will outline different models that are typically used from the simple Drude response over local to non-local random phase approximation (RPA).

Drude model

A simple description of the local response conductivity of graphene taking into account the free carriers is the Drude model:[8,18]

$$\begin{aligned}\sigma(\omega, \tau, n_s) &= \frac{2e^2 v_F \sqrt{\pi n_s}}{h} \frac{i}{\omega + i/\tau} \\ &= \frac{e^2 E_F}{\pi \hbar^2} \frac{i}{\omega + i/\tau}\end{aligned} \tag{1.4}$$

Here ω is the angular frequency of the excitation light and τ the carrier scattering time of the graphene. h and $\hbar$ are the Planck and reduced Planck constant respectively. This term arises from intraband processes and the Drude response describes the graphene conductivity fairly well for situations in which $E_{ph} \ll E_F$. As n_s is *in situ* tunable by changing V_{BG} it is evident from eq. (1.4) that it is possible to tune the Drude response of graphene.

Local random phase approximation

In the random phase approximation (RPA) of graphene we add up the response of all electrons independently without including electron-electron interactions.[18,24–26,56] Just like the Drude model it is only fully valid for small momenta $q \to 0$ but in contrast to the Drude model it does include interband transitions. At finite temperature T the local RPA of graphene can be written in a closed form as:[56]

$$\begin{aligned}\sigma(\omega, T) =& \frac{2e^2 T}{\pi \hbar} \frac{i}{\omega + i/\tau} \log\left[2\cosh\left(E_F/2k_B T\right)\right] \\ &+ \frac{e^2}{4\hbar}\left[H(\omega/2) + \frac{4i\omega}{\pi}\int_0^\infty d\epsilon \frac{H(\epsilon) - H(\omega/2)}{\omega^2 - 4\epsilon^2}\right]\end{aligned} \tag{1.5}$$

where k_B is the Boltzmann constant. The first part of the term is due to the intraband scattering of charge carriers (cf. eq. (1.4)) while the second part is due to interband absorption. Fig. 1.4a,b show the real and imaginary part of the optical conductivity of graphene as a function of incident light wavelength calculated using the local RPA. We can clearly see the three different regimes described in sec. 1.2.

In the equation before $H(\epsilon)$ is given by:

$$H(\epsilon) = \frac{\sinh(\hbar\epsilon/k_B T)}{\cosh(E_F/k_B T) + \cosh(\hbar\epsilon/k_B T)} \tag{1.6}$$

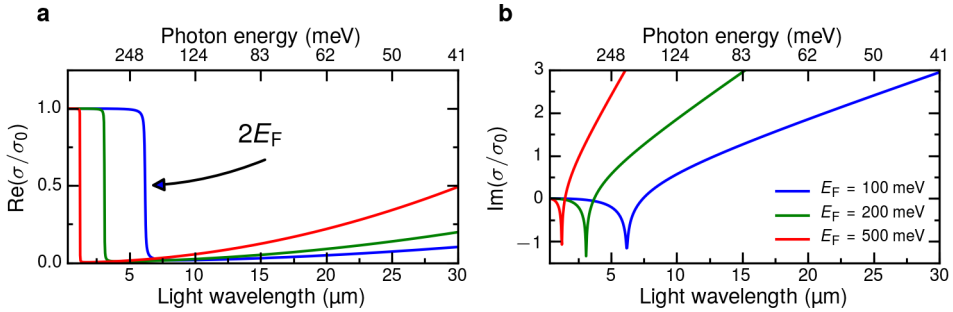

Fig. 1.4.: Optical conductivity of graphene. **a** Real part of the graphene conductivity and **b** imaginary part calculated using the local random phase approximation (eq. (1.5)). Calculated at $T = 0\,\mathrm{K}$ with an effective scattering rate of $\tau = 500\,\mathrm{fs}$ incorporated through the Mermin relaxation approximation.[18] The normalization is done to the universal conductance value of graphene at high frequencies $\sigma_0 = \pi e^2/2h$.[49–51]

The optical absorption A of graphene is proportional to the real part of the conductivity: $A \propto \mathrm{Re}\,\sigma$. For short wavelengths we can see the interband absorption plateau and the associated universal absorption. The drop in absorption and the onset of the Pauli blocking for photon energies smaller than $2E_\mathrm{F}$ is clearly visible. The absorption decreases from 2.3% to close to zero and the onset of the Pauli blocking can be tuned by changing E_F. The increasing absorption for increasing wavelength due to intraband absorption is nicely observed. Furthermore the dependence of the Drude absorption on E_F is observed like expected from eq. (1.4).

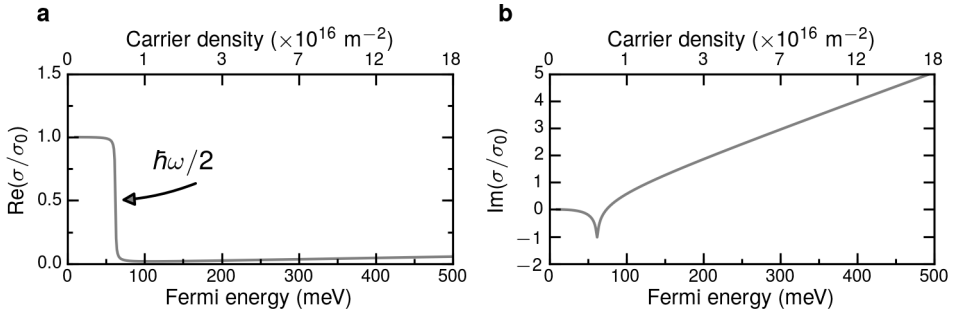

Fig. 1.5.: Optical conductivity of graphene as a function of Fermi energy. **a** Real part of the graphene conductivity and **b** imaginary part calculated using the local random phase approximation (eq. (1.5)) with a scattering time of $\tau = 500\,\mathrm{fs}$ and a photon energy of $\hbar\omega = 124\,\mathrm{meV}$ ($f = 30\,\mathrm{THz}$). The normalization is done to the universal conductance value of graphene at high frequencies $\sigma_0 = \pi e^2/2h$.[49–51]

Fig. 1.5 shows the carrier density dependent σ. Again a plateau is visible and by increasing the Fermi energy it is possible to change the graphene from absorbing to transparent, as indicated by the drop of the real part of σ close to zero. The residual absorption is again determined by the graphene quality.

Non-local random phase approximation

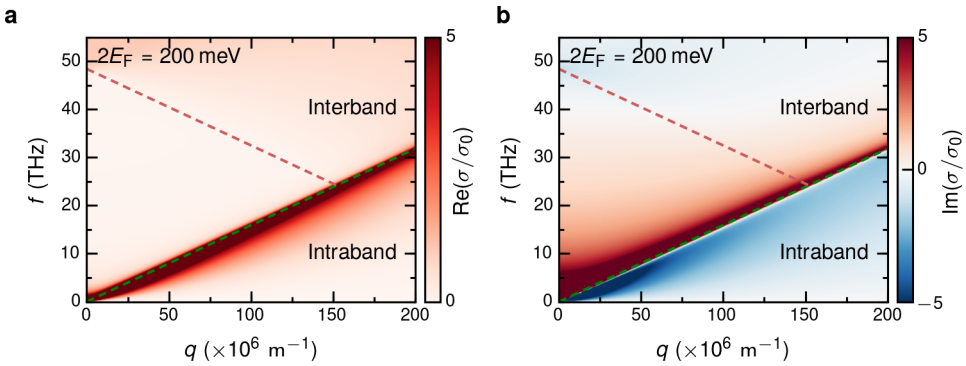

Fig. 1.6.: Non-local graphene conductivity. **a** Real part of the non-local graphene conductivity and **b** imaginary part calculated using the random phase approximation (eq. (1.5)) with a scattering time of $\tau = 500\,\text{fs}$. The Fermi energy is $E_F = 200\,\text{meV}$. The interband and intraband regime are lined out. The normalization is done to the universal conductance value of graphene at high frequencies $\sigma_0 = \pi e^2/2h$.[49–51]

While the local RPA $\sigma(\omega)$ is valid for a carrier momentum $q \to 0$, the non-local RPA is more general. It is also valid for $q \neq 0$ yielding a momentum dependent $\sigma(\omega, q)$. Especially for plasmons that have a very large q this can be very important (see Chapter 3 and 4). For the reader interested in all the details of the non-local RPA the following references allow a great overview: 24–26

Fig. 1.6a and b show the real and imaginary part of the non-local graphene conductivity calculated using non-local RPA. It is evident from the shown calculation that for higher momenta q the q-dependent non-local effects become non-negligible and need to be taken into account. From the dispersion of graphene it is clear that the onset of intraband transitions depends on momentum q and has a slope of v_F.

Permittivity of graphene

It is possible to convert the optical surface conductivity σ into a volumetric permittivity by assuming a finite thickness for the graphene.[57] This can be useful for simulating graphene in various simulation software such as Lumerical FDTD. The conversion is done using:

$$\varepsilon(\omega) = \varepsilon_r + i\frac{\sigma(\omega)}{\varepsilon_0 \omega t} \tag{1.7}$$

where ε_r is the relative background permittivity and t is the thickness of the graphene in the simulation software. Typical values used are $t = 1\,\text{nm}$, slightly thicker than the 0.3 nm measured thickness of graphene in order to reduce the amount of mesh cells needed which can significantly speed up the simulation process. Convergence tests comparing the simulation results of different thicknesses t have to be done to find the desired trade off between accuracy of the simulations and speed.

1.3. Graphene encapsulated in hexagonal boron nitride (h-BN)

Traditionally the substrate of choice for graphene devices is silicon dioxide. This is because graphene on a 300 nm thick silicon dioxide substrate is nicely visible after exfoliation due to interference.[55] However graphene on silicon dioxide has the major drawback that the carrier scattering time is limited by the substrate. This can be due to charged impurities in the substrate leading to Coulomb scattering, ripples and unevenness in the graphene due to the roughness of the substrate or surface phonons of the silicon dioxide.[34,58–60] (An overview of the different scattering mechanisms for different substrates is given in sec. 1.1.1) One way to overcome this limitation is by suspending the graphene without a substrate.[46,61] But these devices are difficult to fabricate and tend to break more easily and are typically contaminated with resist and other chemicals and need to be cleaned by tedious current annealing processes, which can even lead to device destruction.[62] Furthermore, suspended devices have a very limited size and are not practical for the envisioned mass fabrication and commercialization of graphene.[63]

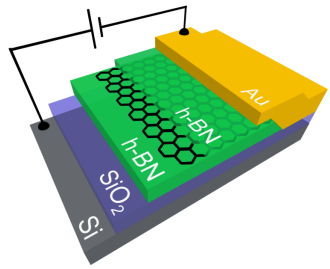

Fig. 1.7.: Encapsulated graphene device with one dimensional edge contact. Graphene fully encapsulated in h-BN shows superior electrical properties of graphene including room temperature scattering limited by acoustic phonons[35] in the graphene and ballistic transport over tens of micrometers at low temperature.[64] The layered structure of h-BN/graphene/h-BN transferred onto a SiO_2 substrate is shown. The typical thickness of the bottom h-BN directly in contact with the substrate is on the order of tens of nanometers.

In the search for the perfect substrate for graphene hexagonal boron nitride (h-BN) turned out to be an ideal candidate.[34] It is a layered insulator that offers an atomically flat surface without dangling bonds or charged impurities and a lattice constant that is similar to the one of graphene. All these properties give graphene on h-BN a high carrier mobility, a low roughness and small intrinsic doping.[34] In the case of graphene on SiO_2 it is known that so called charge puddles form.[59] These are spatial inhomogeneities of the local charge carrier density due to disorder. On h-BN the charge puddle size is increased and the magnitude of charge carrier density variation is decreased which also leads to a reduced scattering of charge carriers and thus a higher mobility.[65]

These devices where graphene is on top of a h-BN substrate still do not reach the ultimate limit of carrier scattering time. This is because even though the graphene is on a flat substrate still its top surface is exposed to air and vapor and more importantly during the fabrication graphene gets into contact with all types of chemicals and resists. To

overcome this limitation the so-called polymer-free van der Waals assembling technique was invented.[35] Using this technique the graphene is never exposed to any chemicals and is safely encapsulated between two layers of h-BN (see Fig. 1.7). In this type of devices graphene shows a carrier lifetime at room temperature which is only limited by scattering with acoustic phonons of the graphene lattice. In other words the graphene mobility has reached the limit at room temperature and is only limited by the unavoidable lattice vibrations of the graphene lattice itself reaching mobilities well over 100,000 cm^2/Vs at low carrier densities.[35] These types of devices also show ballistic transport of charge carriers at low temperatures over distances of tens of micrometers.[35,48,64] The devices also show an extremely low contact resistance,[35] which can be important for some applications such as fast modulators.[66,67]

Also more sophisticated ways of this transfer technique have recently been developed where the amount of bubbles can be reduced using a heated transfer stage.[68] Furthermore it has also been shown that it is possible to achieve the same high mobilities with this technique using graphene grown by CVD,[64] which indicates that in the future high quality graphene transfer could be achieved in a scalable process for mass fabrication.

This transfer technique can also be used to engineer more sophisticated van der Waals heterostructures consisting of many different material layers with unique properties.[69,70] Devices that have already been realized include tunnel transistors,[71,72] solar cells,[73] light emitting diodes[74] and many more. It was also employed to fabricate encapsulated devices made of materials that are unstable at ambient conditions, such as black phosphorus.[75]

1.3.1. Device fabrication

The encapsulated graphene devices explored in this thesis were fabricated using the polymer-free van der Waals assembly technique.[35] A typical transfer setup consists of a translation stage with micrometer positioners, a heating stage where the sample can be mounted and a microscope. A manual on how to build such a transfer setup can be found in ref. 76.

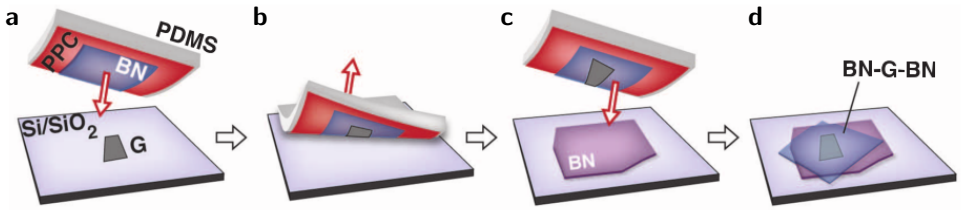

Fig. 1.8.: Polymer-free van der Waals assembling technique. **a** h-BN flake on a PPC/PDMS substrate is brought into contact with exfoliated graphene on a substrate. **b** The whole stack of h-BN/graphene is then picked up. **c** The h-BN/graphene stack is brought in contact with another h-BN flake. **d** The h-BN/graphene/h-BN stack can then be released on the substrate by heating up the substrate. It is also possible to pick up the full stack to continue the stacking process or to release the full stack onto another substrate or metal gates as desired (not shown here). (This figure is taken from ref. 35)

Fig. 1.8 shows the transfer process step by step. The fabrication process of such high quality devices starts by h-BN being exfoliated on a typical SiO_2/Si wafer with an oxide thickness of 300 nm. In order to fabricate devices with the highest quality it can be

necessary to carefully characterize each layer using different inspection techniques such as atomic force microscopy. Then the h-BN is picked up by a stamp made of PDMS and PPC on a glass slide. In the case of the devices for near-field microscopy like in this thesis it is important that the thickness of this h-BN layer is below 10 nm in order for the electric field of the plasmons to penetrate through the top layer of the h-BN. The h-BN is then aligned with a graphene layer on top of a SiO_2/Si wafer using a microscope and brought into contact (Fig. 1.8a). Due to van der Waals interaction between the two layers the graphene adheres to the h-BN and can be easily picked up (Fig. 1.8b). For optimal conditions of the pickup the graphene should be smaller than the h-BN. Now the h-BN/graphene stack can be brought into contact with another layer of h-BN in order to either pick up this layer or to bring down the complete stack at this position (Fig. 1.8c). In order to pick up this second layer of h-BN the flake should be smaller than the top h-BN which was picked up first. Picking up the full stack can be used in order to align the stack on top of local metal gates for example. The release happens by heating the substrate to above 80 °C such that the PPC melts and the full stack is released onto the substrate (Fig. 1.8d).

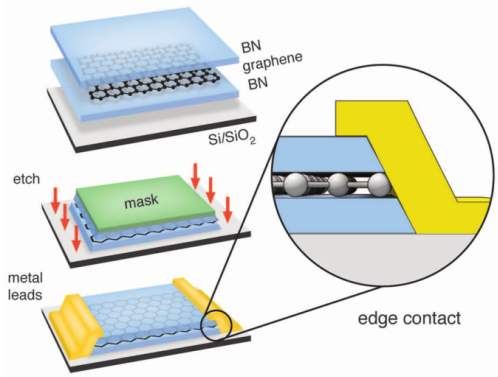

Fig. 1.9.: Fabrication process of one dimensional edge contacts. First the shape of the encapsulated graphene is defined using lithography and a mask is left behind. Then the stack is etched using a directive etching process such as reactive ion etching (RIE). Finally metal contacts are evaporated and a one-dimensional edge contact is formed between the graphene and the metal (This figure is taken from ref. 35).

The PPC can easily be dissolved using acetone and then isopropanol to rinse the sample without leaving chemical residues. For optimal cleanliness the stack can also be annealed in a hydrogen/argon atmosphere at $\sim 300\,^{\circ}C$. It can be seen that at no point during this process the graphene is exposed to any chemicals which is the reason why graphene devices made with this technique show extremely high mobilities.[35]

Electrical contact to the graphene is made by one-dimensional edge contacts (Fig. 1.9).[35] For this the desired shape is written using electron beam lithography and subsequent etching and evaporation of a metal contact. Extremely low contact resistances of around $100\,\Omega\,\mu m$ have been reached.[35]

1.3.2. Optical properties of h-BN

Hexagonal boron nitride is an insulator with a bandgap of $\sim 6\,\mathrm{eV}$ and thus no interband transitions are allowed below that energy.[77] Furthermore there are no free carriers such that also no intraband transitions are allowed. Nevertheless it is interesting for its optical properties in the mid-infrared due to phonons. It even supports so called hyperbolic phonon polaritons.[16,17,78–82] These strong subwavelength modes arise when the in- and out-of-plane permittivity in the h-BN are of different sign in the so called reststrahlen bands of h-BN.[78]

As with many dielectric materials, h-BN is a dispersive material with a frequency dependent permittivity ε due to phonons. Due to the layered nature of h-BN it is an anisotropic material and so its permittivity ε is a tensor. Choosing x, y to be the in-plane directions and z to be the out-of-plane direction ("c-axis"), by symmetry the permittivity must be diagonal in a perfect h-BN crystal:

$$\varepsilon = \begin{pmatrix} \varepsilon_x & 0 & 0 \\ 0 & \varepsilon_y & 0 \\ 0 & 0 & \varepsilon_z \end{pmatrix}$$

with components $\varepsilon_x = \varepsilon_y \neq \varepsilon_z$.

The frequency dependent permittivity ε as a function of the driving electric field with an angular frequency ω can be described by:

$$\varepsilon_l(\omega) = \varepsilon_l(\infty) + s_{\mathrm{v},l} \frac{\omega_{\mathrm{v},l}^2}{\omega_{\mathrm{v},l}^2 - i\gamma_{\mathrm{v},l}\omega - \omega^2}, \qquad l = x, y, z. \tag{1.8}$$

The parameters are the real-valued constants $s_{\mathrm{v},l}$ (dimensionless coupling factor), $\omega_{\mathrm{v},l}$ (normal frequency of vibration), and $\gamma_{\mathrm{v},l}$ (amplitude decay rate). Note that $s_{\mathrm{v},l}$ gives the DC permittivity contribution, so that in the case of a single vibrational mode as in eq. (1.8), one finds $s_{\mathrm{v},l} = \varepsilon_{\mathrm{v},l}(0) - \varepsilon_{\mathrm{v},l}(\infty)$.

In Appendix A.1 we show a table with different values for eq. (1.8).

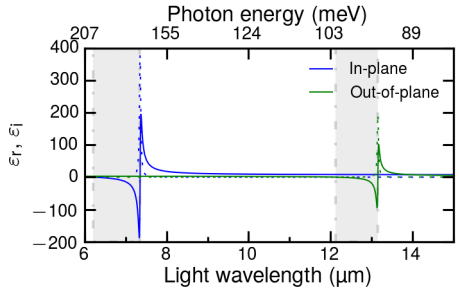

Fig. 1.10.: Real and imaginary part of in- and out-of-plane components of the h-BN permittivity in the mid-infrared. Real parts are depicted as solid lines and imaginary parts as dotted lines. The two reststrahlen bands where the respective real part of the permittivity is negative for one direction and positive for the other is indicated by the gray shaded regions. The model used is from ref. 78.

In h-BN, it is theoretically expected that there are only three polar vibrational modes, one each for x, y, z.[83] The out-of-plane vibration ($l = z$) has significantly different values

of $s_{v,l}, \omega_{v,l}, \gamma_{v,l}$ compared to the in-plane modes ($l = x, y$). In practice, it is sometimes useful to include additional modes to fit the measured permittivity in disordered crystals,[83] however for the clean h-BN used in our studies we consider ideal h-BN with one mode along each direction.

The permittivity calculated by eq. (1.8) completely characterizes the h-BN for optical studies at frequencies up to and including the mid-infrared. For bulk h-BN this permittivity is known to produce interesting behaviour of electromagnetic modes.

Transverse phonon polaritons near $\omega_{v,l}$. Near this frequency, the permittivity along l diverges to very large values ($\operatorname{Re}\varepsilon_l \sim \pm 100$). For light polarized along direction l, a strong peak in reflectivity (near 100%) is observed at this frequency.[78,83]

Longitudinal phonon polaritons near $\omega_{L,l} = \omega_{v,l}\sqrt{\varepsilon_l(0)/\varepsilon_l(\infty)}$. At this frequency, ε_l passes close to 0. This allows a purely electric oscillation that is longitudinal, i.e., electric field parallel with the phase velocity.[83]

Hyperbolic phonon polaritons for $\omega_{v,l} < \omega < \omega_{L,l}$. In this frequency range (the so-called reststralen band), $\operatorname{Re}\varepsilon_l < 0$ in direction l, yet $\operatorname{Re}\varepsilon$ is positive along another direction. This results in a hyperboloidal constant-frequency surface of propagating modes in k-space, rather than the usual ellipsoid that appears for most frequencies. This hyperboloid extends to very high k (short wavelength) allowing propagating modes of very short wavelength.[78] The group velocities of these confined modes are correspondingly low and are nearly perpendicular to their phase velocities.[80] These hyperbolic phonon polaritons propagate as rays with a frequency dependent angle $\tan\theta(\omega) = i\sqrt{\varepsilon_{x,y}(\omega)}/\sqrt{\varepsilon_z(\omega)}$.[84]

The frequency dependent permittivity of h-BN for the in-plane and out-of-plane direction is shown in Fig. 1.10 and the reststrahlen bands are marked. For thin h-BN films, the effects of the transverse and longitudinal modes are somewhat diminished, yet the hyperbolic modes start to exhibit waveguiding[84] and have been exploited to produce subwavelength resonant structures.[78]

I

Plasmons in graphene: Fundamentals and applications

In this part of the thesis plasmon waves are introduced and their fundamental properties, such as their tunability and strong wavelength confinement is shown for the most simple case of free standing graphene. Then give an overview over different available techniques to excite plasmon waves in graphene is given. A focus is put on scattering-type scanning near-field infrared microscopy (s-SNOM) as this was the tool of choice for observing and characterizing graphene plasmons in this thesis. Next two main results of this thesis are presented. First it is shown how by properly choosing the graphene substrate the lifetime of graphene plasmons can be greatly enhanced. It will be presented how graphene encapsulated by hexagonal boron nitride shows plasmon lifetimes of up to 500 fs and what this lifetime is limited by. Finally a first application of such long lifetime plasmons is introduced: a phase modulator for light with an extremely small subwavelength footprint of 350 nm and the light phase being fully tunable in situ from 0 to 2π.

2. Background on plasmons and s-SNOM

Plasmons in graphene have some very promising properties, such as their extreme wavelength and mode volume confinement[8] which makes them an ideal candidate for molecular sensing.[21,85] Furthermore they allow graphene to absorb much more than the typically quoted 2.3 % for interband transitions.[86] This makes them a great candidate for improving graphene photodetectors in the mid-infrared.[87]

However in order to excite graphene plasmons a mismatch between plasmon momentum and the momentum of free space light has to be overcome. Different ways exist to excite and measure graphene plasmons. A very common technique is to use electron-energy-loss spectroscopy (EELS).[88–90] In order to probe low energy plasmons, nanostructured graphene was investigated in the infrared and terahertz regime.[31] In this case the graphene plasmons are excited by a far-field infrared light source and the extinction of the device is measured by e.g. Fourier transform infrared spectroscopy (FTIR). Graphene plasmons are then observed in the spectrum as changes in reflection or transmission.[21,31,32,52,91–94] One disadvantage of this technique is the challenging fabrication. It is extremely difficult to keep the width of the nanoribbons constant as their width needs to be on the order of the plasmon wavelength, thus a width of only hundreds of nanometers. The changing ribbon width leads to inhomogeneous broadening of the observed plasmon resonance in the far-field and thus this technique is not suitable for finding the intrinsic lifetime of graphene plasmons. Moreover no spatial information of the plasmon wave propagation is available.

One of the more recent approaches is to measure plasmons by scattering type sanning near-field optical microscopy (s-SNOM).[29,30,79,95–102] It has also been used to successfully probe plasmon excitations in carbon nanotubes.[103] This is the technique of choice for this thesis and a more detailed description is given in section 2.2.

2.1. Fundamentals of plasmons in graphene

In Fig. 2.1a we show the frequency dependent permittivity of a typical Drude material. In order for plasmons to exist as long lived excitations the real part of the permittivity ε_r has to be negative.[17] For graphene this is the case in the terahertz and mid-infrared frequency range of the electromagnetic spectrum. Moreover the permittivity can be tuned by changing the Fermi energy of graphene.

In Fig. 2.1b we show amplitude and field lines of the in-plane electric field of graphene plasmons as well as the charge carrier distribution. As in the case of plasmons in a two dimensional system, such as graphene, all the free charge carriers are involved in the plasma oscillation. Thus it is evident that by changing the amount of charge carrier n_s in the graphene the plasmon properties can be modified strongly. Furthermore due to the possibility of doping ambipolarly both electron and hole plasmons can be excited.

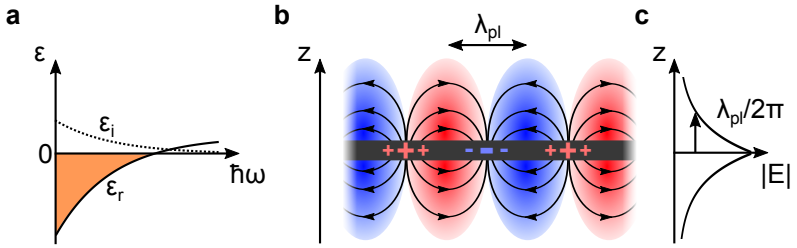

Fig. 2.1.: Sketch of the main plasmons features and the condition for their existence. **a** In order for bound electromagnetic modes to exist the real part of the permittivity ε_r of the material has to be negative. In the case of graphene plasmons this is due to the intraband motion of free carriers, commonly described by the Drude response of graphene. **b** Amplitude and field lines of the in-plane electric field. The plasmon wavelength λ_{pl} is indicated. **c** The out-of-plane electric field of graphene plasmons is an evanescent field with a strong confinement and a $1/e$ amplitude decay length of $1/k_{pl} = \lambda_{pl}/2\pi$.

Fig. 2.1c shows the evanescent nature of the out-of-plane electric field and its strong confinement. Indeed for free standing graphene the out-of-plane decay length is $1/k_{pl} = \lambda_{pl}/2\pi$.[18]

2.1.1. Frequency dispersion of graphene plasmons

For sufficiently high Fermi energies the graphene plasmon dispersion inside two semi-infinite materials can be described by the complex valued plasmon wavevector q_{pl} as:[8]

$$\begin{aligned} q_{pl}(\omega, n_s, \tau) &\approx \omega\epsilon_0(\epsilon_{r,sub}(\omega) + \epsilon_{r,sup}(\omega))\frac{i}{\sigma(\omega, \tau, n_s)} \\ &= k_{pl} + i\,\mathrm{Im}\,q_{pl}. \end{aligned} \tag{2.1}$$

Here n_s is the carrier density of the graphene and $\epsilon_{r,sub}(\omega)$ and $\epsilon_{r,sup}(\omega)$ are the frequency dependent permittivities of the substrate and superstrate respectively. The frequency dependent surface conductivity of graphene is $\sigma(\omega, \tau, n_s)$, and k_{pl} is the real part of the plasmon wavevector.

A dimensionless figure of merit for the propagation of graphene plasmons is the inverse damping ratio $\gamma_{pl}^{-1} = k_{pl}/\,\mathrm{Im}\,q_{pl}$. It describes how many plasmon wavelengths a graphene plasmon can propagate before its amplitude has decayed to $1/e$. It is evident that the plasmon propagation depends on the dielectric environment due to the permittivity of the substrate and superstrate influencing eq. (2.1) as well as the graphene quality due to the influence of σ.

By substituting $\sigma(\omega, n_s)$ with the Drude formula for graphene as defined in eq. (1.4) the graphene plasmon wavelength $\lambda_{pl} = 2\pi/k_{pl}$ can be written as:[8,18]

$$\lambda_{pl} \approx \lambda_0\alpha\frac{E_F}{E_{ph}}\frac{4}{\epsilon_{r,sub} + \epsilon_{r,sup}}. \tag{2.2}$$

Here λ_0 is the free space wavelength of the far-field light, $\alpha = \frac{1}{4\pi\epsilon_0}\frac{e^2}{\hbar c} \approx 1/137$ the fine-structure constant. For typical values of permittivity and photon and Fermi energy

$\frac{E_F}{E_{ph}} \frac{4}{\epsilon_{r,sub}+\epsilon_{r,sup}} \sim 1-10$ which shows that the graphene plasmon wavelength is typically $\lambda_{pl} \sim \alpha\lambda_0$ or about one hundred times smaller than the free space wavelength of the excitation light. This strong wavelength reduction leads to a large momentum mismatch between the free-space excitation light and the plasmons, which needs to be overcome for effective plasmon launching. The out-of-plane decay length of the graphene plasmon is $\sim \lambda_{pl}/2\pi$, also more than two orders of magnitude smaller than the free-space wavelength of the excitation light.[18]

Moreover it is directly visible that the plasmon wavelength $\lambda_{pl} \propto E_F \propto \sqrt{n_s}$ can be tuned simply by tuning the carrier density of the graphene. This makes graphene plasmons unique as their wavelength is *in situ* tunable.

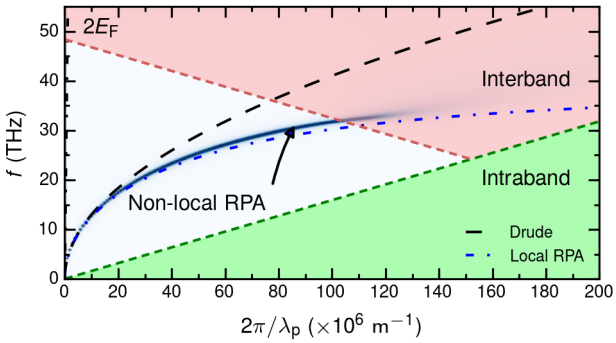

Fig. 2.2.: Frequency dispersion of graphene plasmons in free standing graphene. The graphene plasmon dispersion calculated using different conductivity models of for the graphene (see section 1.2). The simple Drude model (eq. (1.4)) for the graphene conductivity $\sigma(\omega)$ shows the typical square root frequency dispersion of graphene plasmons for free standing graphene (black dashed curve). The plasmon dispersion obtained by the local RPA conductivity is shown as blue dashed-dotted curve and by the non-local RPA as the blue solid curve. The Landau damping regions due to intraband and interband single particle electron-hole excitations are indicated in shaded green and orange respectively. Their onset can be tuned by changing E_F.[15] Here $E_F = 100\,\text{meV}$ and $\tau = 500\,\text{fs}$. The difference between the light line $k = \omega/c$ for free space light (black dashed dotted line close to $k = 0$) and the graphene plasmon momenta show the strong momentum mismatch between plasmons and free space light.

In Fig. 2.2 we show the graphene plasmon frequency dispersion calculated using different graphene conductivity models. The Drude model for the graphene conductivity $\sigma(\omega)$ shows the simple square root dependence on momentum. For small plasmon momentum all three models show good agreement while for higher momenta a clear mismatch becomes visible. In the green and orange shaded regions graphene plasmons decay rapidly because of interband or intraband transitions. These regimes can be tuned by tuning the carrier density.[8,25]

A clear discrepancy between the Drude model and local RPA is visible. This is due to the interband transition appearing in the local RPA but not in the Drude model. As seen in Fig. 1.4 this leads to $\text{Im}\,\sigma$ crossing zero close to the interband threshold photon energy. The local RPA model for the parameters used in this example gives $\text{Im}\,\sigma = 0$ for $f \approx 40.3\,\text{THz}$. According to eq. (2.1) this leads to $q \to \infty$ which explains the observed

asymptotic behavior of the dispersion using the local RPA.

The non-local RPA takes into account also the momentum dependence of the conductivity, i.e. $\sigma(\omega, q)$ (see 1.2.1 and Fig. 1.6). It is evident that for large momenta a mismatch between local and non-local RPA is expected. The analysis, presented in the following chapters, requires the use of the non-local RPA model to fully explain the data. The non-local RPA plasmon dispersion is calculated using the transfer-matrix method and we plot the imaginary part of the Fresnel reflection coefficient. Plasmon modes are seen as poles in the imaginary part of the Fresnel reflection coefficient.[104] Thus the vanishing mode inside the interband regime shows that there are indeed high losses for the plasmons in the interband region, mainly due to interband excitations becoming the favourable process over plasmon excitations.

Fig. 2.3 shows the frequency dispersion of graphene plasmons for different Fermi energies. The strong tunability of the plasmon momentum and thus the plasmon wavelength λ_{pl} with Fermi energy is remarkable. This makes graphene a unique plasmonic material as it allows to tune λ_{pl} *in situ*. This strong tunability has also been shown experimentally.[100] For comparison also the light line of free space light is shown as a dashed-dotted line close to $k = 0$. The strong momentum mismatch between graphene plasmon and free space light is evident.

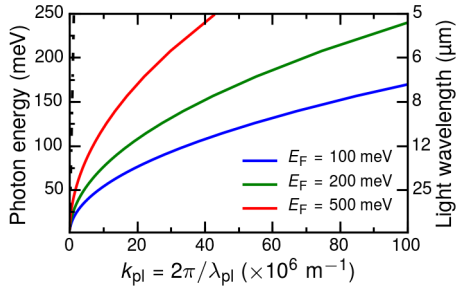

Fig. 2.3.: Frequency dispersion of graphene plasmons for different Fermi energies. By changing the Fermi energy of graphene the frequency dispersion of the graphene plasmons and thus the plasmon wavelength can be tuned *in situ*. Here the damping due to intraband and interband excitations is not taken into account (see Fig. 2.2). The light line of the free space light is shown as a dashed dotted line close to $k = 0$.

2.1.2. Fresnel reflection coefficient

The interface between two media with the refractive indices n_1 and n_2 is known to reflect light. Fig. 2.4 shows such an interface and the and all the necessary parameters. The relation between the angle of the incoming wave θ_i and the transmitted wave θ_t is given by Snell's law as $n_1 \sin\theta_i = n_2 \sin\theta_t$. The relation between the incoming and the reflected wave is given by the law of reflection as $\theta_i = \theta_r$.

The Fresnel reflection coefficient r_{TM} is the ratio of the complex electric field amplitude of the reflected wave reflected to that of the incident wave and can be calculated using:[105]

$$r_{TM} = \frac{n_2 \cos\theta_i - n_1 \cos\theta_t}{n_1 \cos\theta_t + n_2 \cos\theta_i} \tag{2.3}$$

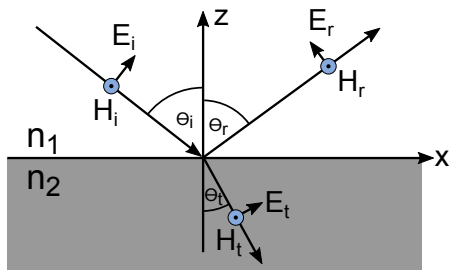

Fig. 2.4.: Reflection and transmission of a transverse magnetic (TM) polarized incoming wave at an interface. Two materials with refractive index n_1 and n_2 respectively form an interface and an electromagnetic wave with TM polarization gets reflected. Here E_i and H_i are the electric and magnetizing field of the incoming, E_r and H_r of the reflected and E_t and H_t of the transmitted electromagnetic wave respectively.

The transmission coefficient can be calculated using:

$$t_{\mathrm{TM}} = \frac{2n_1 \cos\theta_\mathrm{i}}{n_1 \cos\theta_\mathrm{t} + n_2 \cos\theta_\mathrm{i}} \tag{2.4}$$

2.1.3. Transfer-matrix method

While the dispersion calculated using eq. (2.1) gives an idea of how the substrate influences the dispersion it is only strictly valid for a semi-infinite substrate and superstrate. Also the Fresnel equations described above only provide a simple method for calculating how electric and magnetic fields act after impinging on a single boundary between two materials. For layered systems more sophisticated models that take into account multiple reflections and interference, such as the transfer-matrix method, have to be used. The transfer-matrix method is well known to characterize the propagation of electromagnetic waves through layered media.[106] When using the proper thicknesses and permittivities of each of the layers involved excellent agreement between theory and experiment can be reached. A good description of using the transfer-matrix method with graphene is given in ref. 107 and 104. In the case of the transfer-matrix method used in this thesis we used a numerical implementation in Python developed by Mark B. Lundeberg at ICFO.[108]

The transfer-matrix method works well to study transverse magnetic (TM) waves with the two field components E_x and H_y in planar structures, where the permittivity of the system can change in the out-of plane (z) direction and is uniform in the in-plane (x, y) direction. We consider waves at a fixed frequency ω and fixed in-plane wavevectors k_x and $k_y = 0$. So, all fields can be described as $F(x, y, z, t) = F(z)e^{ik_x x + 0y - i\omega t}$.[108]

Each material layer of the system can then be described by a so-called transfer matrix M_l, where l denotes the layer. The electric field at a given boundary can then be calculated if the details of the field at the adjacent boundary and the refractive index and thickness of the medium between boundaries are known. This can be done for an arbitrary amount of layers.

The idea of the method is that by multiplying the transfer matrix of each layer one is able to to map the electric field at the bottom of the stack to the electric field at the top of the stack. In the case of plasmons, like it is of our interest in this thesis, we are looking

for electromagnetic fields that are evanescently decaying at the top and the bottom of the stack.

The typical contour plots of the plasmon dispersion used throughout this thesis are showing the imaginary part of the Fresnel reflection coefficient calculated by the transfer-matrix method. The complex Fresnel reflection coefficient is defined as the ratio between the bound mode evanescently decaying away from the top surface and the wave that exponentially increases away from the surface at the position of the top surface. This reflection coefficient is a complex function of complex k_x and ω. Bound modes, such as plasmons, are found at a pole for real ω at a complex $k_x = q_x$. This complex q_x contains information about the wavelength and losses of the plasmons.

2.1.4. Hybridization of the plasmon with the substrate phonons

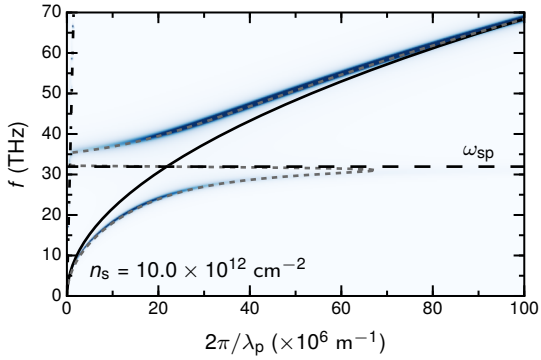

Fig. 2.5.: Hybridization of graphene plasmons with the substrate. Due to the vicinity of the graphene to the underlying substrate there is a strong interaction between the graphene plasmons and the substrate phonons. The blue curve is the imaginary part of the Fresnel reflection coefficient calculated using the transfer-matrix method. In this case the substrate is SiO_2 and the difference between the square root dispersion (solid curve) and the actual dispersion due to the substrate is clearly visible. The simple plasmon dispersion (grey dashed curve) is calculated using eq. (2.1). An avoided crossing at the polar phonon frequency ω_{sp} of the substrate is visible. For frequencies far away from the phonon frequency of the resonance the square root dispersion for a simple Drude model is restored. The SiO_2 permittivity is taken from ref. 109.

As graphene is typically not suspended but rather on top of a substrate it is obvious from eq. (2.1) that the substrate permittivity will strongly influence the frequency dispersion of the graphene plasmon. Indeed there will be avoided crossings, at the polar phonon frequencies (ω_{sp}) of the substrate (for SiO_2 see Fig. 2.5). From the difference between the square root dispersion (solid curve) and the actual dispersion it is evident that the substrate has to be taken into account for any type of dispersion calculation.

The simple dispersion calculated form eq. (2.1) (grey dashed curve) and the transfer matrix calculated dispersion (blue color plot) agree well. This shows that the simple dispersion calculation works extremely well for semi infinite substrates and superstrates like in this case.

Zero crossings of the plasmon momentum due to plasmon and substrate phonon cou-

pling are expected from eq. (2.1) where $\mathrm{Re}\,\epsilon_{r,sub}(\omega) = -1$ when the superstrate has a permittivity of $\epsilon_{r,sup} = 1$, i.e. vacuum, like in this case. The losses associated with the avoided crossing, visible in the full calculation of Fig. 2.5 as fainter blue, are due the imaginary part of the SiO_2 permittivity, and are thus called dielectric losses (see section 2.1.5). These losses are especially severe for the plasmon propagation length as due to the small group velocity (as seen by the small slope of the dispersion curve) the plasmon propagates extremely slowly with very high loss.

2.1.5. Plasmon damping mechanisms

As described in section 1.1.1 charge carriers in graphene can scatter with different mechanisms leading to a reduced transport mobility of graphene. As plasmons are charge oscillations coupled to electromagnetic radiation it is obvious that mechanisms leading to a reduced transport scattering time can also affect the plasmon scattering time in graphene. It is however important to note that the transport and plasmon scattering time are only related quantities and the transport scattering time should be used only for a very rough estimation of the plasmon scattering time.[100,110,111] This is because the plasmon scattering time is the scattering time of the electron system at $\omega > 0$ and a finite momentum $q \gg 0$. In contrast the transport scattering time is for $\omega = 0$ and momentum $q = 0$ due to the linear dispersion of charge carriers in graphene.[110]

In the following I will review the most relevant scattering mechanisms for plasmons.

Charged impurity scattering losses are due to the plasmon scattering with a charged impurity and subsequently losing its energy.[110] Just like in the case of the transport lifetime limited by charged impurities (see section 1.1.1) the plasmon lifetime is expected to increase with increasing carrier density due to increasing screening. However, the plasmon lifetime is calculated to be significantly shorter than the transport one.[110] It has been shown that for the case of graphene on a SiO_2 substrate the measured plasmon decay rates can be explained by this type of scattering.[110]

Acoustic phonon scattering losses are due to the electrons in graphene scattering with the lattice vibrations of the graphene lattice itself.[35,43,111] In this case the plasmon lifetime is calculated to only weakly depend on carrier density and while the transport lifetime is decreasing with increasing carrier density (see section 1.1.1) the plasmon lifetime is slightly increasing.[111] We were able to show that at room temperature for extremely clean encapsulated graphene this mechanism is a main limitation of the scattering time of graphene plasmons.[100] We explain our findings in great detail in chapter 3.

Optical phonon scattering losses occur when electrons scatter inelastically with the plasmon, taking energy from the plasmon and scattering it into an optical phonon in the substrate or the graphene.[32,111] While the contribution of optical phonons to the transport scattering time is negligible due to their large energy,[43] they need to be taken into account in the case of plasmons with a finite ω and q.[111]

Electron-electron (e-e) scattering losses are an intrinsic scattering mechanism of charge carriers in graphene in the absence of any order scattering mechanism such as disorder or lattice vibrations and the ultimate limit of the plasmon scattering time.[112] The plasmon lifetimes expected for graphene limited only by e-e scattering exceed

the currently experimentally achieved lifetimes by two orders of magnitude and thus only play a minor role in current considerations.[100] A pathway to reach these long lifetimes could be to suppress acoustic phonon scattering and measure encapsulated graphene samples at cryogenic temperature, for example using a cryogenic near-field microscope like the one described in ref. 113.

Dielectric losses give rise to plasmons dissipating energy to the environment and not, like the other loss mechanisms discussed before, due to plasmons dissipating energy to the electronic system of the graphene itself.[110,111] This is associated with the imaginary part of the permittivity of a graphene substrate or superstrate. In eq. (2.1) it is evident that a larger imaginary part of the surrounding permittivities will lead to a larger $\mathrm{Im}\, q_{\mathrm{pl}}$ which indicates a shorter propagation distance and thus more damping. Especially for low quality substrates with a large imaginary part of the permittivity and a large amplitude decay rate $\gamma_{v,l}$ (see (1.8)) this loss can be significant not only close to the phonon resonance of the substrate. Both in the case of graphene on SiO_2[29,30] and on h-BN[100] it has been shown that dielectric losses cannot be neglected.

2.2. Scattering-type scanning near-field optical microscopy (s-SNOM)

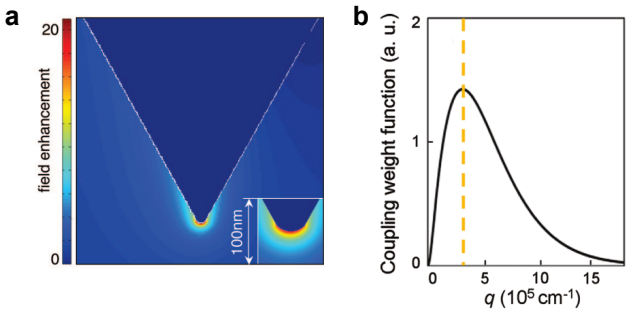

Fig. 2.6.: Near-field enhancement at the tip apex and resulting momentum distribution. **a** Due to a lightning rod effect there is a strong near-field at the apex of the tip which can be used to overcome the momentum mismatch between the graphene plasmons and the far-field light. The length scale associated with this near-field is wavelength independent and is given by the tip radius. Here the incoming light wavelength is $\lambda_0 = 118\,\mu\mathrm{m}$. **b** Momentum distribution of a tip with an apex radius of 30 nm peaking at $q = 3.4 \times 10^5\,\mathrm{cm}^{-1}$. This means that a tip with this radius couples best to wavelengths of $\approx 185\,\mathrm{nm}$. (**a** taken from ref. 114 and **b** taken from ref. 95)

In order to excite graphene plasmons, exhibiting momentum more than 100 times the photon momentum, the momentum mismatch has to be overcome. This is why the scanning probe technique called scattering-type scanning near-field optical microscopy (s-SNOM)[36] is an extremely practical tool to measure plasmons in graphene.[29,30,95] With s-SNOM the necessary momentum to excite graphene plasmons is provided by the sharpness of a metallized atomic force microscopy (AFM) tip.[95,115] It provides very high resolution

spatial images of the near-field optical response, which allows at the same time for the measurement of graphene plasmons. It is able to measure real space images of graphene plasmons which allow insight into their properties such such as their wavelength and decay length.

The advantage of scattering-type near-field systems over conventional near-field microscopes using apertures is that the spatial resolution is completely wavelength independent and is determined by the radius of the tip apex used.[36] This results in spatial resolutions on the order of tens of nanometers for light wavelengths in the infrared[36] or even terahertz regime[114,116] of the optical spectrum.

In Fig. 2.6a we show the near-field of a typical metallized atomic force microscope tip illuminated by infrared light with a polarization parallel to the shaft. It is evident that the resolution is linked with the geometry of the tip apex. For sharper tips an even higher spatial resolution is possible. A field enhancement of ~ 20 is typical.

Fig. 2.6b shows the momentum distribution provided by a tip with an apex radius of 30 nm.[95] It follows a bell shape. For sharper tips a higher momentum and thus a shorter plasmon wavelength can be accessed experimentally. The maximum of the bell shape and thus the best coupling between the sample and the AFM tip is reached for an in-plane momentum $q \approx 1/a$, where a is the radius of the AFM tip apex.[95] But there is a tradeoff between reachable momentum and signal as for smaller tip apexes the signal strength decreases.

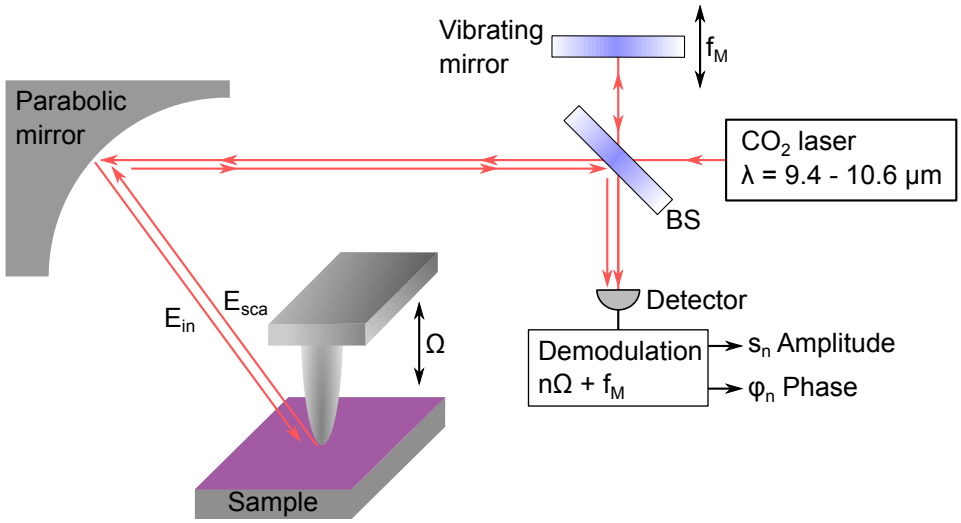

Fig. 2.7.: Sketch of the working principle of a s-SNOM with pseudo-heterodyne detection. The s-SNOM uses pseudo-heterodyne detection[117] to measure amplitude and phase at the same time. This is possible due to a vibrating mirror and a Michelson interferometer. The beam splitter (BS) used for our laser is made of ZnSe. The incoming electromagnetic field E_{in} and the out scattered one E_{scat} are indicated. The mechanical vibration frequency of the cantilever is Ω ($\sim$ 250 kHz) and of the vibrating mirror f_m ($\sim$ 400 Hz).

Besides the probe tip being extremely important for the spatial resolution, the other important part of the s-SNOM system is the pseudo-heterodyne detection. It is based on

modulating the phase of a reference wave.[117] It allows to extract background-free near-field signals containing information about amplitude and phase of the light scattered out by the AFM tip, which is also called optical signal. Fig. 2.7 shows a sketch of this system. A laser source is used to couple light into an interferometer in Michelson configuration. Part of the light is passed through the beam splitter (BS) and focused onto a metallized atomic force microscope (AFM) tip by means of a parabolic mirror. The polarization of the laser is parallel to the shaft of the probe tip. The parabolic mirror guarantees wavelength independent operation. The light interacts with the sample through the tip and gets scattered by the tip. Part of the scattered light is collected by the parabolic mirror and sent back to the beam splitter where it interferes with the light that has been reflected by the vibrating mirror. By demodulating the signal of the detector at higher harmonics n of the mechanical tapping frequency of the tip Ω and measuring at the sidebands created by the mechanical frequency of the vibrating mirror f_m it is possible to fully retrieve amplitude and phase of the near-field light scattered by the sample.[117] Higher harmonics appear due to the non-linear dependence of the scattering amplitude and phase on the tip-sample distance.[36]

2.2.1. Measuring graphene plasmons using s-SNOM

Near-field microscopy allows unprecedented insight into the electric field distribution close to the surface of different materials and devices, such as metals and photonic crystals.[118] Using s-SNOM one can directly measure the plasmon wavelength and decay length in real space. This allows a simple interpretation of the data.

A simple description of the measured data is the following: the strong near-field at the probe apex of the atomic force microscope tip provides the necessary momentum to overcome the mismatch between far-field photon and plasmon. This plasmon wave then propagates radially away from the tip (Fig. 2.8a). The plasmon gets reflected from the graphene edge[29,30] (or defects, grain boundaries,[96] sharp steps in the substrate,[97] etc.) and a interference pattern between the launched plasmon wave and the edge-reflected plasmon wave is formed (Fig. 2.8b). The optical signal $\xi_{opt}(x)$ detected by the s-SNOM system is proportional to the plasmon wave amplitude $E(x)$ underneath the tip. It is important to not that we do not directly observe the interference pattern shown in Fig. 2.8b but rather we observe the optical signal directly at the position of the probe tip. We then move the probe tip on the sample and measure the optical signal at each position. This results in a decaying signal away from the edge as shown in Fig. 2.8c.

The electric field of the propagating graphene plasmon wave can be described as:[18]

$$E(x) = Ae^{ixq_{pl}} \tag{2.5}$$

With A being complex amplitude and x the position on the graphene sheet and q_{pl} the complex valued plasmon wavevector as described before.

A simple way of modelling what happens to graphene plasmons when they are reflected at a graphene edge and how they can be measured using s-SNOM is the so called mirror dipole method or method of images.[29] In Fig. 2.8a a graphene plasmon is excited and propagates radially away from the origin. When a plasmon source is brought close to a graphene edge the plasmons are reflected from the edge and form a standing wave pattern (Fig. 2.8b). Here $x = 0$ denotes the position of the graphene edge. Graphene is present for $x \geq 0$ and no graphene for $x < 0$. The measured optical signal is then given by:

$$\begin{aligned}\xi_{\text{opt}}(x) &\propto |E(0) + e^{i\Phi_R} E(2x)| \\ &= |A + Be^{i\Phi_R} e^{i2xq_{\text{pl}}}|\end{aligned} \tag{2.6}$$

where $E(0)$ is the electric field amplitude underneath the tip due to the tip-launched plasmon wave. The reflected plasmon wave is given by $e^{i\phi}E(2x)$ as the reflected plasmon has travelled twice the tip edge distance x. A and B are fixed complex amplitudes, where A collects all contributions that would already occur away from the edge – local response, plasmon launching, etc. The complex coefficient B includes factors of reflection, in-coupling, out-coupling, etc.

The phase shift Φ_R is acquired due to the reflection and is close to π.[29,119] A theoretical study suggests that the actual phase shift acquired is $3/4\pi$,[120] this was however not observed experimentally.[119] By moving the plasmon source away from the edge and recording the amplitude at each position we can measure the standing wave pattern. The interference underneath the tip is then constructive at

$$x_n = \frac{\lambda_{\text{pl}}}{2}(n - \frac{\Phi_R}{2\pi}), \quad n = 1, 2, \ldots \tag{2.7}$$

This means that the measured fringe spacing, or the distance between the maxima, is $\lambda_{\text{pl}}/2$ as shown in Fig. 2.8c.

From eq. (2.6) it is evident that the measured optical signal will decay exponentially due to $\text{Im}\, q_{\text{pl}}$. This is due to the plasmon wave lifetime. Furthermore there is a $1/\sqrt{r}$ amplitude decay away from the tip due to geometrical decay in two dimensions. It ensures energy conservation of the wavefront, which has circumference $2\pi r$.[100]

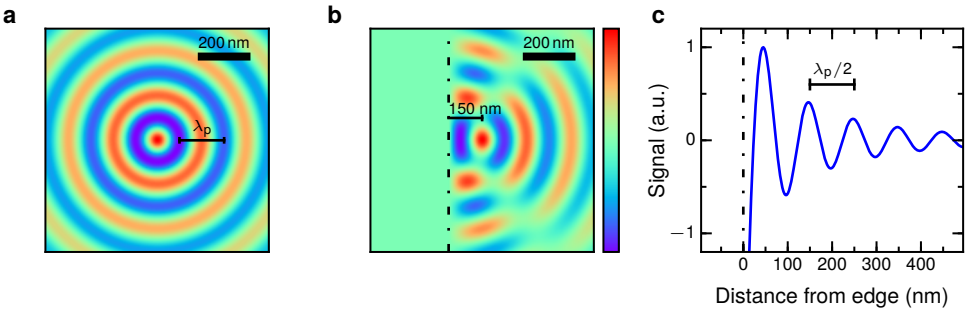

Fig. 2.8.: Simulation of propagating graphene plasmons and their reflection at graphene edges. **a** Graphene plasmons propagate radially away from a dipole source and decay. The plasmon wavelength λ_{pl} is 200 nm. **b** At the edge of graphene the plasmons get reflected and form a standing wave. **c** The standing wave pattern as a function of distance from the graphene edge taking into account that the reflection phase of graphene plasmons is $\Phi_R = \pi$[29] as well as the $1/\sqrt{r}$ amplitude decay away from the edge due to energy conservation reasons. The inverse damping ratio is γ_{pl}^{-1} is 25.

2.2.2. s-SNOM setup

The s-SNOM used for the studies was a Neaspec neaSNOM microscope. In Fig. 2.9 a photograph of the setup is shown. On the left the vibrating mirror is marked. It is used

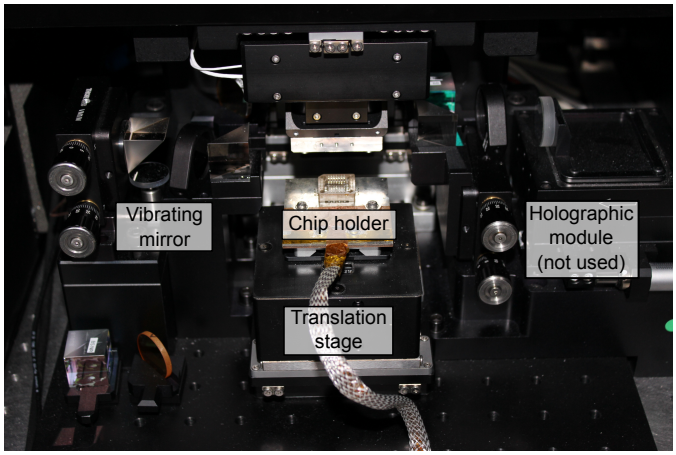

Fig. 2.9.: Neaspec s-SNOM system used for the experiments. The s-SNOM we used included a pseudo-heterodyne module,[117] which we used for most of the measurements as well as a holographic module.[99] The holographic module allows to finely control the length of the interferometric arm which can be extremely useful when working with lasers with a short coherence length.

for pseudo-heterodyne detection to extract amplitude and phase of the scattered light signal simultaneously.[117] There are two screws to align the laser beam with this mirror and make sure the light reflected from the mirror copropagates with the light scattered from the atomic force micrscope tip. Before the mirror a neutral-density filter is placed which allows to tune the light power from the interferometric arm of the system.

A chip holder is connected to a digital to analog converter via cryogenic wire loom with 24 wires. This allows full eletrical control of our devices. The cryogenic wire loom is shielded in order to reduce electrical noise from affecting the signals using a braided metal mesh shielding. It is placed on the translation stage. This cable is extremely flexible and does not affect the movements of the translation stage.

A box was built around the system to isolate it from air flow and vibrations which can influence the measurements. Also the box allowed to flush nitrogen gas which can be used to reduce the humidity inside the box. Flushing nitrogen gas has to be done very carefully as it changes the humidity of the system and parts of the system tend to move when the humidity changes. Especially some of the screws used to align the laser to the vibrating mirror are affected. The optical input and output ports for this box are ZnSe windows which can be screwed into the box.

The atomic force microscope probes used were tapping mode tips with a tip radius $< 25\,\text{nm}$ (NanoWorld Arrow NCPt). We use "Arrow" type tips as here the position of the probe is well known and at the very end of the cantilever. This greatly facilitates alignment of the infrared laser.

In order to steplessly tune the laser power incident on the s-SNOM we use a polarizer/analyzer configuration of two CaF_2 holographic wire grid polarizers (Thorlabs WP25H-C). The polarizer is mounted in a rotation mount and the analyzer is mounted such that the output polarization is always perpendicular to the optical table plane. In order to measure the output power after the analyzer we use a power meter (Newport 1918-R).

The typical power used is $\sim 20\,\mathrm{mW}$.

As mid-infrared light source we use a CO_2 laser which is tunable from 9.4 to 10.7 µm (Access Laser Company L4G) with a water chiller for temperature control (Solid State Cooling Systems Oasis 3). As mid-infrared detector a HgCdTe detector is used (Kolmar Technologies). For alignment purposes we use a HeNe Laser at 632.8 nm (Thorlabs HNL150L).

3. Plasmon propagation in h-BN encapsulated graphene

In this chapter we demonstrate that in the case of graphene encapsulated by h-BN dramatic improvements in the graphene plasmon damping and field confinement can be achieved. Furthermore, we establish an excellent understanding of the graphene plasmon dispersion and damping for a wide range of carrier densities. In contrast to earlier reports, we find much lower plasmon damping and that impurity scattering does not play a significant role in plasmon damping, pointing at very low intrinsic limits on the plasmon damping in graphene.

Graphene plasmons were predicted to possess ultra-strong field confinement and very low damping at the same time, enabling new classes of devices for deep subwavelength metamaterials,[11,121] single-photon nonlinearities,[28] extraordinarily strong light-matter interactions,[18] and nano-optoelectronic switches. While all of these great prospects require low damping, thus far strong plasmon damping was observed,[29,30,98] with both impurity scattering[110] and many-body effects in graphene[29] proposed as possible explanations. With the advent of van der Waals heterostructures,[34,70] new methods have been developed to integrate graphene with other atomically flat materials. In the following chapter we exploit near-field microscopy to image propagating plasmons in high quality graphene encapsulated between two films h-BN.[35] We determine dispersion and particularly plasmon damping in real space. We find unprecedented low plasmon damping combined with strong field confinement, and identify the main damping channels as intrinsic thermal phonons in the graphene and dielectric losses in the h-BN. The observation and in-depth understanding of low plasmon damping is the key for the development of future graphene nano-photonic and nano-optoelectronic devices.

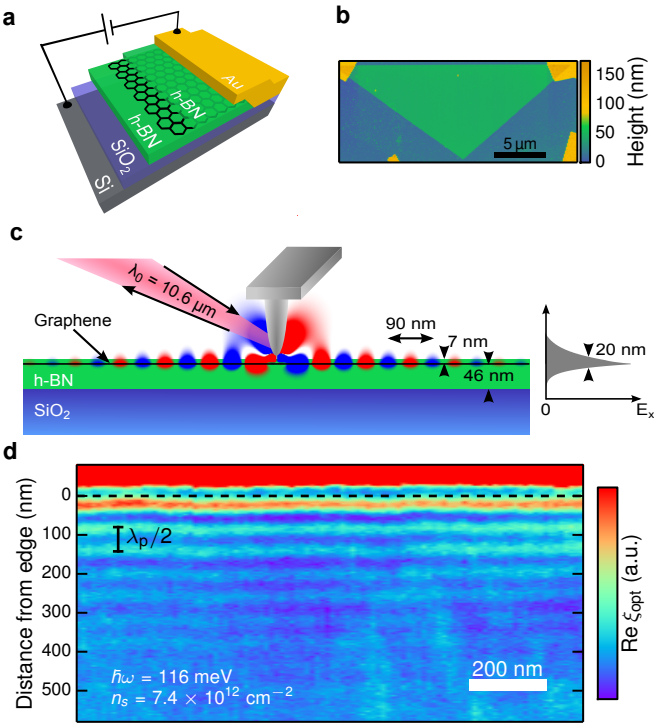

Fig. 3.1.: Device and plasmon imaging with s-SNOM. a Sketch of the layered heterostructure with a Si backgate, SiO_2 layer, h-BN, graphene, h-BN, and a gold side contact. **b** Topography image of the device. The triangle is two h-BN layers encapsulating a graphene layer, contacted at two corners. The blue outer area is etched. **c** Simplified side-view schematic of the s-SNOM measurement including probe tip, excitation, and detection. Plasmons are launched radially from the tip. The color map shows the simulated in-plane component of the electric field of a dipole source oscillating at a photon energy of 116 meV coupling to graphene plasmons using Lumerical FDTD. The simulated field confinement of the plasmon in the out-of-plane direction of 20 nm at full width half maximum can be seen on the right. **d** s-SNOM optical signal from two-dimensional scan of tip position, near the graphene edge at room temperature (dashed line). Edge-reflected plasmons appear as interference fringes with a spacing of half the plasmon wavelength λ_{pl}.

Graphene–h-BN heterostructures[34,70] have recently attracted great interest due to their unusual electronic band structure, sensitive to the crystallographic alignment between graphene and h-BN.[122] Optically, these heterostructures are just beginning to be explored,[94] and they are expected to produce unusual plasmonic behaviour in the case of an aligned lattice.[123] This has actually been shown for graphene grown aligned on an h-BN crystal.[124] Furthermore, h-BN itself is an interesting optical material as it shows natural hyperbolic behaviour, meaning that the in- and out-of-plane component of the permittivity have opposite signs in the *reststrahlen* frequency bands.[125] This implies that h-BN supports deep subwavelength slow-light phonon polariton modes within those bands.[78,84] Combining h-BN with graphene gives rise to unconventional plasmon-phonon hybridization[79,94] and this hybrid system can be used for tailoring novel subwavelength metamaterials. Besides all of those exotic properties, h-BN can provide an exceptionally clean environment

for graphene. Recent advances in graphene device fabrication, exploiting the unique properties of h-BN heterostructures produced by the polymer-free van der Waals assembling technique, resulted in significantly less disorder. This leads to the carrier transport mobility at room temperature reaching its intrinsic limit dominated by thermal phonon scattering.[35]

3.1. Device

The device was fabricated by Yuanda Gao in the group of James Hone at Columbia University according to our input. A device sketch of the layers is provided in Fig. 3.1a. A topography image of the device acquired via atomic force microscopy is depicted in Fig. 3.1b. The h-BN(7 nm)–graphene–h-BN(46 nm) stack assembled by the polymer-free van der Waals assembling technique[35] lies on top of an oxidized silicon wafer, used as a backgate. The device geometry as well as the electrical side-contacts were defined using electron beam lithography and dry etching, in the method of Ref. 35. The backgate capacitance density was estimated to be $6.7 \times 10^{10}\ e\,\mathrm{cm}^{-2}\,\mathrm{V}^{-1}$, where e is the elementary charge for the bottom layer thickness of 46 nm.

3.2. Measurements

We image propagating plasmons using s-SNOM, as explained in detail in sec. 2.2. In order to avoid the strong photodoping in encapsulated graphene it is crucial to turn off any light in the s-SNOM such as the navigation light.[126] A continuous wave CO_2 laser, with tunable photon energy from 115 to 135 meV (laser wavelength λ_0 from 10.8 to 9.2 µm), is used. We operate in a frequency band where $\mathrm{Re}\,\varepsilon$ is strictly positive and the most important aspect of the h-BN dielectric constant is its anisotropy and its dielectric loss to avoid complications for the graphene plasmons[111] (see eq. (1.8)). The overall permittivity, including its high anisotropy (with $\varepsilon_x \approx 9$ and $\varepsilon_z \approx 2$ in the studied frequency range around 10 µm), is very important for matching the measured plasmon wavelengths.

Interferometric detection of the scattered light yields magnitude and phase as the complex-valued optical signal ξ_{opt}. A scan of $\mathrm{Re}\,\xi_{\mathrm{opt}}$ vs. tip position near the graphene edge shows characteristic fringes due to the varying field of the reflected plasmon, interfering with the local response.[29,30] Figure 3.1c shows these fringes measured near a straight edge in our device. For simplicity most figures only show $\mathrm{Re}\,\xi_{\mathrm{opt}}$, however similar information appears in $\mathrm{Im}\,\xi_{\mathrm{opt}}$ as described by equation (3.4). All analysis (background subtraction, fitting, etc.) was performed simultaneously on $\mathrm{Re}\,\xi_{\mathrm{opt}}$ and $\mathrm{Im}\,\xi_{\mathrm{opt}}$.

3.2.1. Detection of graphene edge location

In separating out the contributions from geometrical decay from exponential decay, it is important that the location of $x = 0$ (the graphene edge) has been determined with accuracy. An error in this determination leads to error in the extracted damping. The location of the etched graphene edge ($x = 0$) was determined from the simultaneously-measured topography.

It is well known that tip convolution artefacts result in modified appearances of sharp edges in scanning probe microscopy. We assume that our physical etched edge is sharply vertical as illustrated in Fig. 3.2, such that the rounding and sloping apparent in the

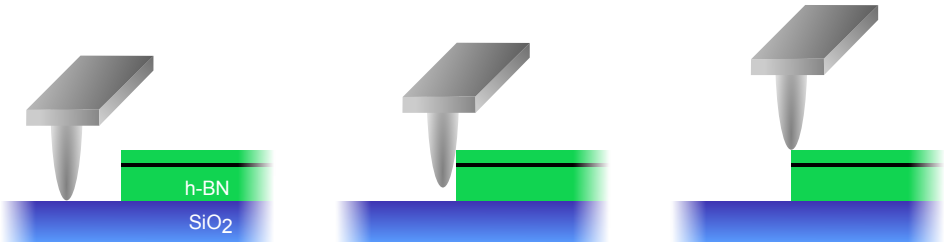

Fig. 3.2.: Tip convolution effects make the topography edge appear away from the graphene edge. We define $x = 0$ to occur when the tip is centered directly above the graphene edge—this is the situation depicted in the third panel.

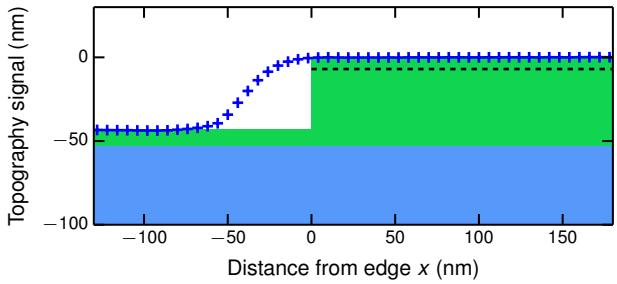

Fig. 3.3.: Topographic signal from measurement (blue crosses) with the interpreted actual topography underneath. The graphene (dashed line) is assumed to terminate at the end of the round feature, since this round feature is interpreted as a tip convolution effect. From the topographic flatness the excellent quality of the h-BN devices is visible.

topographic signal is purely due to the AFM tip convolution (Fig. 3.2). As a result, the edge is located directly beneath the point where the rounding convolution ends, illustrated in Fig. 3.3. With the chosen edge-detection algorithm it is only possible that the graphene edge is actually further on the left in Fig. 3.3 which would lead to an underestimation of our extracted inverse damping ratios. Note that even if the edge were not strictly vertical, the error in x would be on the order of a few nanometers since the graphene lies only 7 nm under the surface.

3.3. Carrier density dependence of the optical response

Due to the encapsulation of the graphene, our device possesses only small intrinsic doping and a uniform doping distribution with a small density of electron-hole puddles.[65] This enables us to study the optical response for a wide range of carrier densities n_s, including features near the charge neutrality point, by applying a backgate voltage V_g. In Fig. 3.4a we tune the plasmon fringes in both wavelength and amplitude and show that λ_{pl} depends strongly on n_s. With decreasing carrier density the fringe visibility decreases, as the wavelength of plasmons becomes shorter. The tip cannot couple to plasmons with an arbitrarily short wavelength due to the non-zero tip radius[95] and their confinement in the top h-BN layer.

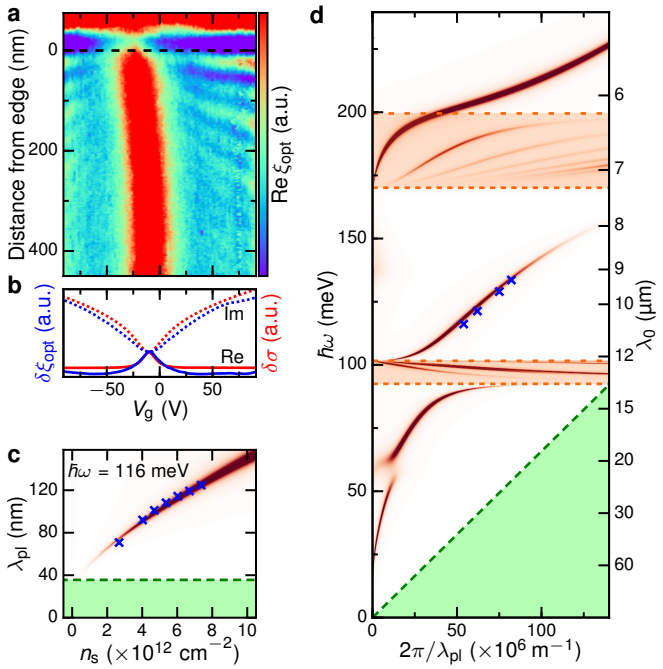

Fig. 3.4.: Optical signal and plasmon wavelength dependence on carrier density and photon energy. **a** s-SNOM optical signal from scan of tip position perpendicular to the graphene edge (dashed line) and gate voltage, showing gate-dependence of plasmon fringes at a photon energy of $\hbar\omega = 116$ meV. **b**, Change in complex optical signal away from the edge (blue, from **a**) with respect to gate voltage, compared to theoretical local conductivity for ideal graphene (red).[24,25] **c** Plasmon wavelength dependence on carrier density. **d** Dependence on frequency, at $n_s = 7.4 \times 10^{12}$ cm^{-2}. Shaded orange regions indicate the h-BN frequency bands in which propagating phonon polaritons can exist. In both **c** and **d**, crosses show the extracted experimental values. The electronic intraband Landau damping region is shaded green. The red background color plot is the imaginary part of the Fresnel reflection coefficient of evanescent waves, evaluated at the top h-BN surface. The damping has been modified (reduced dielectric loss) to enhance the visibility of modes—this does not significantly modify the mode locations.

While changing n_s we also observe changes in the optical response. This is most clearly seen in Fig. 3.4b where we plot ξ_{opt} versus n_s with the signal averaged from 400 nm to 700 nm from the edge, where plasmon interference effects are weak. With appropriately chosen phase, ξ_{opt} is approximately proportional to the change in complex valued graphene conductivity σ (Fig. 3.4b). Near charge neutrality (small $|n_s|$), $\mathrm{Re}\,\sigma$ dominates which gives information about interband conductivity. A corresponding peak in $\mathrm{Re}\,\xi_{opt}$ appears where graphene is charge neutral, in this case near $V_g \approx -10$ V. With increasing carrier density $\mathrm{Re}\,\sigma$ ($\mathrm{Re}\,\xi_{opt}$) decreases due to Pauli blocking and $\mathrm{Im}\,\sigma$ ($\mathrm{Im}\,\xi_{opt}$) grows due to ballistic free carrier motion (Drude-like response).

A detailed study of the plasmon wavelength dependence on carrier density and frequency is shown in Fig. 3.4c,d together with calculations of the graphene plasmon dispersion of the full system. The calculations include optical thin film effects via the transfer-matrix method which need to be included due to the thin h-BN top film as well as graphene non-

local conductivity which needs to be considered due to the low plasmon phase velocity and high plasmon momentum. The measured wavelengths show parameter-free agreement with these electromagnetic calculations (red curves in Fig. 3.4c,d).

For our frequency range, the h-BN lattice is a highly anisotropic dielectric, i.e. birefringent, environment for the plasmon, which enhances its confinement. The out-of-plane full width at half maximum confinement of the plasmon electric field is calculated to be $\sim 20\,\mathrm{nm}$ (Fig. 3.1c). We observe λ_{pl} as low as 70 nm, 150 times smaller than the free space light wavelength. This constitutes a record high volume confinement of propagating optical fields of $\sim 10^7$ compared to the modal volume in free space.

The additional modes (in the orange-marked reststrahlen bands of h-BN in Fig. 3.4d) that appear in the calculation are due to the propagating phonon polaritons in thin h-BN.[78,84] These phonon modes can hybridize with the graphene plasmons, however the plasmons are effectively unhybridized for the frequency range used in this study. Later studies show these hybrid plasmon phonon modes experimentally and show how they can be controlled experimentally.[79]

3.3.1. Dispersion comparison

In Fig. 3.5 and Fig. 3.6 we compare different dispersion models which are outlined in the following.

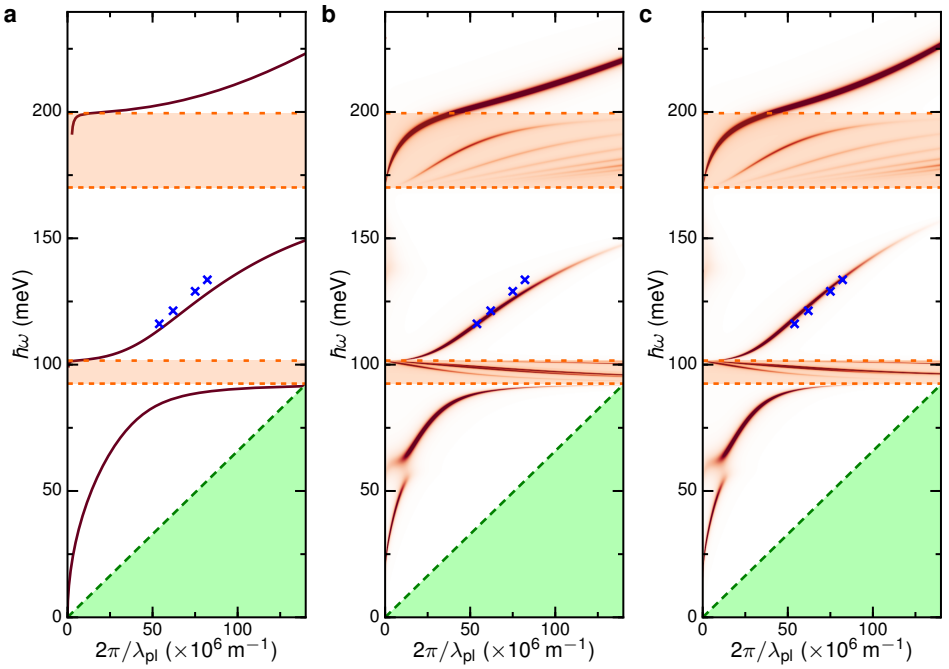

Fig. 3.5.: Frequency dispersion comparison for different models. **a** Drude model for graphene conductivity and simple effective permittivity for h-BN surrounding the graphene. **b** Local RPA for graphene conductivity and thin film effects for h-BN surrounding the graphene. **c** Non-local RPA for graphene conductivity and thin film effects for h-BN surrounding the graphene. Scattering time $\tau = 500$ fs, $n_{\mathrm{s}} = 7.37 \times 10^{12}$ cm^{-2}.

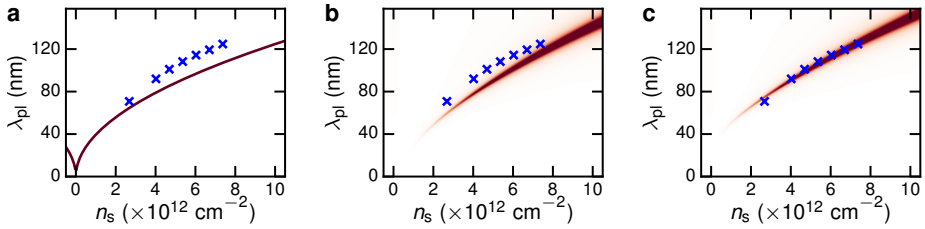

Fig. 3.6.: Comparison of the carrier density dependence for different models a Drude model for graphene conductivity and simple effective permittivity for h-BN surrounding the graphene. **b** Local RPA for graphene conductivity and thin film effects for h-BN surrounding the graphene. **c** Non-local RPA for graphene conductivity and thin film effects for h-BN surrounding the graphene. Scattering time $\tau = 500$ fs, $n_s = 7.37 \times 10^{12}$ cm^{-2}.

Drude conductivity with semi-infinite h-BN (Figs. 3.5,3.6a) Simple Drude conductivity for the graphene as in eq. (1.4) and the simple graphene plasmon relation given in eq. (1.4). Both top and bottom h-BN layer are considered to be semi-infinite and the effective h-BN permittivity is calculated using $\varepsilon \equiv \sqrt{\varepsilon_{xx}\varepsilon_{zz}}$. Note that here no propagating phonon polariton modes are visible inside the reststrahlen bands marked in orange.[111]

Local RPA conductivity with thin-film effects (Figs. 3.5,3.6b) A significantly improved fit is achieved by using the local RPA model and especially by including thin film effects of the 46 nm bottom and 7 nm top h-BN. However for large plasmon momenta a clear discrepancy between model and experiment is observed. Due to the thin film effects propagating hybrid plasmon phonon polariton modes exist in the reststrahlen bands of h-BN.[79]

Non-local conductivity with thin-film effects (Figs. 3.5,3.6c) Including the non-local conductivity we achieve an even better fit, especially for higher wavevectors where non-local effects start playing a more significant role. This shows that especially for large plasmon momenta the non-local conductivity of the graphene has to be taken into account. The zero temperature random phase approximation (RPA) result[24–26] was used for the graphene non-local conductivity $\sigma(k, \omega)$.

3.4. Optical signal model

Ideally, the tip interacts only with the graphene underneath its apex, responding to the electric susceptibility of the graphene and acting as a localized "point source" for exciting plasmons. The plasmons spread out as a circular wave (2D radial wave), reflect off the nearby graphene edge and return to the tip. Even in the ideal lossless case, only a small part of this returning wave couples to the tip, due to geometrical decay. In practice, there are further interaction pathways: the light path does not only interact with the tip but also directly with the sample, and moreover the tip does not solely interact with the graphene under its apex.

This section describes the expected optical signal for a reflected circular wave, that has $\lambda_{pl}/2$-period fringes as well as the origin of the fringes with λ_{pl}-period and their expected optical signal in order to provide a model to fit the measured fringes.

3.4.1. Fringes with λ_{pl}-period

The origin of the fringes with a spacing of half the plasmon wavelength λ_{pl} was already discussed in sec. 2.2.1. Broken translational symmetry at the edge provides for matching the small photon wavevector with the large plasmon wavevector. As a simple model, one can think of the wave $E(x)$ being launched by an oscillating electric field at the edge.[127] This produces a plane wave plasmon without additional geometrical decay:

$$E(\tilde{r}) \sim E_{edge} e^{i q_{pl} r_x}, \tag{3.1}$$

so that a contribution proportional to $E_{edge} e^{i q_{pl} x}$ is added to $\xi_{opt}(x)$. This is the case for plasmons being launched directly by the illuminating laser spot which is effectively a plane wave on these nanometer length scales. However there was no dependence on the angle of incidence observed in our experiments, which would be expected for a launching directly at the edge by the polarized far-field laser source. This is in accordance with later studies[102] which also did not observe any angle dependence.

There are however other possibilities that lead to plasmons that travel only once the tip-edge distance x. One possibility is the reverse of the above, that the plasmons launched at the tip are scattered to light at the graphene edge. In this process the geometrical decay is less obvious: the plasma wave decays geometrically from the tip so that the field at the edge decays as $1/\sqrt{x}$, yet also the wave arrives in-phase over a larger section of the edge, tending to cancel this decay.

Another possibility is that the near-field tail of the tip interacts with the edge and launches a plasmon there, a plasmon which is then received at the tip after travelling x. This is similar to the far-field case, except the tip acts as a field-enhancing mediator between light and edge. Here additional geometrical decay is expected because the electric field of the near-field tail depends on the tip-edge distance. It is not clear what distance dependence this near-field profile should take—monopolar, dipolar, or somewhere in-between. This profile would also be modified by lateral field focussing by the h-BN. Again, the reverse process (launching at tip, then the long-ranged tail of the edge plasmon field interacts with the tip) is also possible.

To allow for these various mechanisms we include a variable geometrical decay in this contribution to ξ_{opt}:

$$\xi_{edge}(x) \propto \frac{e^{i q_{pl} x}}{x^a + R^a},$$

where R is the tip apex radius, included to limit the divergence in this expression. In the picture of plasmon plane wave launching at the edge, this would correspond to taking a distance-dependent edge field in Eq. (3.1)

$$E_{edge}(x) \propto \frac{1}{x^a + R^a}.$$

The optical signal then shows the period of an edge-launched plane wave, but with additional geometrical decay whose origin is unclear.

Later measurements of similar heterostructures also observed fringes with a λ_{pl}-spacing.[102] The authors of ref. 102 have modelled the system in more detail and attribute the fringes to the interaction of the edge with the tip.

3.5. Fringe fitting (parameter extraction)

In order to extract parameters, such as propagation length, from the fringe signal, we need an accurate model of the expected signal for a given amount of damping. Based on the previous section, we have a decent model for the decay of fringes away from the edge:

$$\xi_{\text{opt}}(x) = \xi_{\text{bulk}}(x) + A\frac{e^{i2q_{\text{pl}}x}}{\sqrt{x}} + B\frac{e^{iq_{\text{pl}}x}}{x^a}, \tag{3.2}$$

where the fitting parameters are complex A, B and q_{pl}, and real a. Here ξ_{bulk} collects together all contributions that would already occur away from the edge – local response, plasmon launching, etc., and, the complex coefficient A collects together factors of reflection, in-coupling, out-coupling, etc. The tip radius is fixed to $R = 25$ nm.

There are however some complications to directly fitting the raw data:

- The location of the edge, $x = 0$, needs to be detected accurately (see sec. 3.2.1)
- The background part of the signal, $\xi_{\text{bulk}}(x)$, is not known a priori and we see clear signs of spatial variations. Fortunately, these variations (due to carrier density gradients) appear to be gradual.
- The model in Eq. (3.2) does not necessarily hold for small values of x. For the first fringe, the tip coupling mechanism may become very different than when the tip is over the bulk. Direct fitting of the data with equal residuals weighting is not suitable in this case.

The edge we detect from the topographic data of the s-SNOM apparatus, taking into account tip convolution effects. To avoid biases from the unknown ξ_{bulk} and the unknown first-fringe behaviour, we subtract a smooth background from the signal/model, and then perform fits in a transformed version of the signal/model. In the following we describe this procedure in great detail.

3.5.1. Background subtraction

Since $\xi_{\text{bulk}}(x)$ is not known a priori, we can only estimate it from the dataset itself. After discarding the data for $x < 0$, we estimate $\xi_{\text{bulk}}(x)$ by smoothing the measured $\xi_{\text{opt}}(x)$. The difference,

$$\delta\xi_{\text{opt}}(x) = \xi_{\text{opt}}(x) - \xi_{\text{smooth}}(x) \tag{3.3}$$

should then be free of influence from the unknown ξ_{bulk}.

Background subtraction always results in removal of some of the desired signal, and is a well known source of statistical bias. In this case, background subtraction leaves transient artifacts near $x = 0$ due to the abrupt termination of the signal, and also selectively removes part of the fringes depending on their period (i.e., affecting more the λ_{p}-period fringes than $\lambda_{\text{p}}/2$-period fringes). In order to give a fair comparison, we apply the same background subtraction procedure to the models used in the fit.

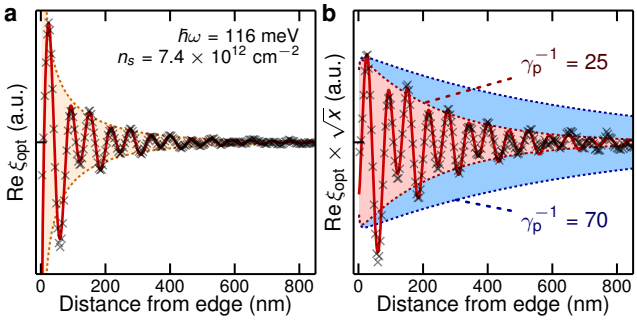

Fig. 3.7.: Extraction of plasmon damping. **a** Black crosses show the s-SNOM optical signal from Fig. 3.1d, averaged along the edge, with a smooth background subtracted. A fit to eq. (3.4) is shown as a red line. The shaded region shows the decay envelope of the first term of equation (3.4). **b** Same signal and fit as in **a** multiplied by $\sqrt{x}$ to isolate exponential decay. The shaded regions show the exponential decay envelopes of the first term of equation (3.4) for the measured damping ($\gamma_{\mathrm{pl}}^{-1} = 25$) and for the case limited only by electron scattering from thermal phonons ($\gamma_{\mathrm{pl}}^{-1} = 70$).

3.6. Damping

The capability to carry plasmons with such strong field confinement and at the same time relatively low propagation damping is a unique property of graphene compared to other plasmonic materials.[8] In order to quantify the propagation damping, we average linescans of the complex ξ_{opt} perpendicular to the graphene edge at different locations, and subtract the background (Fig. 3.7a). The decay of the fringes away from an edge is due to a combination of damping ($\mathrm{Im}\, q_{\mathrm{pl}} > 0$) and circular-wave geometrical spreading. The oscillating signal of Fig. 3.7a fits well with (see eq. (3.2)):

$$\xi_{\mathrm{opt}}(x) = A\frac{e^{i2q_{\mathrm{pl}}x}}{\sqrt{x}} + B\frac{e^{iq_{\mathrm{pl}}x}}{x^a}, \tag{3.4}$$

with complex parameters A, B, q_{pl} and real a. The first term is the returning field for a damped circular wave reflected from a straight edge, with the plasmon travelling $2x$. The second term interferes with the first, producing alternating fringe amplitudes. It arises because plasmons are not only generated/detected beneath the tip apex, but also weakly at the edge of the graphene.[127] These plasmons travel only the tip-edge distance x and therefore show twice the fringe spacing of the plasmons generated/detected beneath the tip apex. As the geometrical decay of the plasmon travelling the tip-edge distance only once is not known *a priori*, we allow for a variable decay $a \sim 1$ (see sec. 3.4.1). Nevertheless, because the $\exp(2iq_{\mathrm{pl}}x)$ component dominates and we can separate the $\exp(iq_{\mathrm{pl}}x)$ component with Fourier analysis, we can extract $\mathrm{Im}\, q_{\mathrm{pl}}$ unambiguously (see sec. 3.5).

3.6.1. Extracted damping

The inverse damping ratio $\gamma_{\mathrm{pl}}^{-1} = \mathrm{Re}\, q_{\mathrm{pl}}/\,\mathrm{Im}\, q_{\mathrm{pl}}$ is a dimensionless figure of merit of propagation damping. Fig. 3.7b shows the data multiplied with $\sqrt{x}$ to isolate the damping decay $\exp(-2\,\mathrm{Im}\, q_{\mathrm{pl}}x)$, and visually indicates the significance of $\gamma_{\mathrm{pl}}^{-1}$—in this case, $\gamma_{\mathrm{pl}}^{-1} \approx 25$.

This is a significant improvement over the $\gamma_{pl}^{-1} \sim 5$ seen in studies of unencapsulated graphene on silicon dioxide.[29,30]

From spatial damping, the plasmon amplitude decay time τ_p can be calculated using the group velocity $v_g = (d\,\mathrm{Re}\,q_{pl}/d\omega)^{-1}$. In this case $v_g \approx 10^6$ m/s, coincidentally the same as the Fermi velocity of graphene electrons (see Fig. 3.4d). We find $\tau_p = (\mathrm{Im}\,q_{pl})^{-1}/v_g \approx$ 500 fs, which is remarkably long for strongly confined optical fields, and an order of magnitude longer than the amplitude decay time of plasmons in silver, the metal with the longest plasmon amplitude decay time.[128] For surface plasmons at a Ag/SiO_2 interface inverse damping ratios above 20 are only feasible for an energy range where the wavelength confinement is below two.[8]

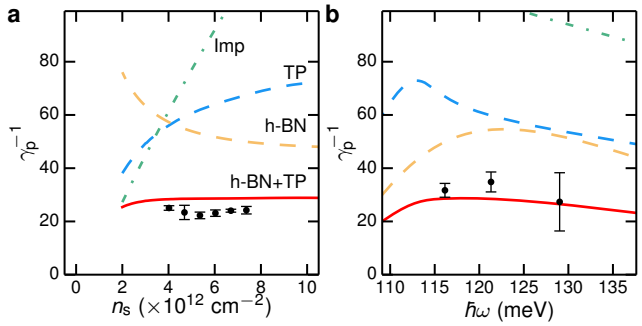

Fig. 3.8.: Plasmon damping mechanisms. **a** The inverse damping ratio as a function of carrier density at a photon energy of 116 meV. **b** The inverse damping ratio as a function of excitation frequency at a carrier density of 7.4×10^{12} cm^{-2}. Both **a** and **b** also show the theoretical inverse damping ratios due to graphene thermal phonons (blue dashed curve), charge impurities at concentration $n_{imp} = 1.9 \times 10^{11}$ cm^{-2} (green dash-dotted curve), dielectric losses of h-BN (yellow dashed curve) and the combination of graphene thermal phonons and dielectric losses of h-BN (red curve).

3.6.2. Damping mechanisms

The different possible damping mechanisms of graphene plasmons have been discussed in sec. 2.1.5. In order to distinguish between them a carrier density dependence can give important information. Thus we investigate the role of the different damping mechanisms by measuring the inverse damping ratio as a function of both n_s and excitation frequency, and compare the results in Fig. 3.8 with the calculated damping for various damping channels. Interestingly, we find experimentally that plasmon damping is constant with carrier density. The calculations are based on the non-local conductivity $\sigma(q,\omega)$ evaluated at the plasmon wave vector $q = q_{pl}$ and at the excitation frequency ω. Such calculations show that charge carrier scattering is strongly modified at high frequency and thus the effective electron scattering time for plasmons can differ from the transport scattering time.[110,111] The theoretical models were developed by Alessandro Principi, Matteo Carrega, Giovanni Vignale and Marco Polini.

Damping from impurity scattering does not play a role for plasmon damping in these high quality heterostructures, because it would lead to strongly reduced damping for increasing n_s, due to increasing electrostatic screening.[110] This is however not

observed experimentally as seen by the flat carrier density dependence. This trend is shown by the green dashed dotted curve in Fig. 3.8 which is based on a plasmon damping theory due to impurity scattering.[110]

Damping from intrinsic thermal phonons in graphene shows a much weaker dependence on n_s[111] (dashed blue curve in Fig. 3.8). From quantitative comparison, we find that (without fitting parameters) this intrinsic damping mechanism accounts for approximately half the observed damping and thus we conclude that this is one of the dominant intrinsic damping mechanism. Extensive details on the calculations of plasmon damping due to thermal phonon scattering are presented in Ref. 111.

Damping from dielectric losses in the substrate provides an additional damping pathway, independent of the electronic damping pathways discussed before. In particular, the dielectric losses of the h-BN encapsulating the graphene may give a significant contribution (yellow dashed curve in Fig. 3.8). However the typical values reported for thick h-BN films do not show a high enough dielectric loss to account for the losses observed. In the following we present how thin h-BN films can potentially have higher dielectric losses than the bulk material.

3.6.3. Increased dielectric losses for thin h-BN films

In clean bulk monocrystals $\mathrm{Re}(\varepsilon)/\mathrm{Im}(\varepsilon)$ can be as high as 400.[78,84] However Caldwell et al. have noticed in measuring the reflection of thin h-BN films in Ref. 78 that the effective $\gamma_{v,l}$ seems to be larger than bulk. As a result h-BN, especially the very thin upper layers in this case, may have higher losses as this leads to a decreased $\mathrm{Re}(\varepsilon)/\mathrm{Im}(\varepsilon)$ in the frequency range of interest of this chapter. In Fig. 3.9 a comparison between clean and damaged h-BN from Ref. 78 is shown. The simulations were done using the far-field transfer-matrix method for layered materials taking into account the thickness of the flakes and the substrate. For the BaF_2 substrate permittivity we use $\varepsilon = 2$.[109]

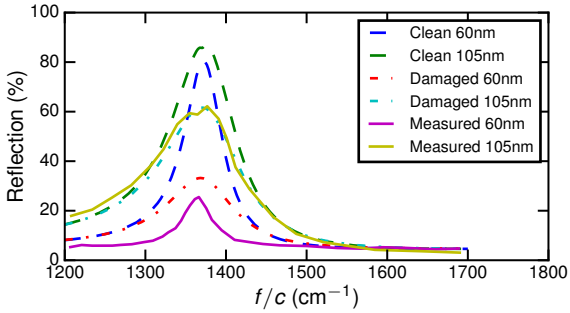

Fig. 3.9.: Reflection spectra of thin h-BN samples. Comparison between measured reflection from the supplement of Ref. 78 and simulated reflection for thin h-BN flakes. The clean h-BN uses the in-plane phonon linewidth of 0.87 meV from Ref. 78. The simulations of the damaged ones have an increased in-plane phonon linewidth of 3.7 meV in the case of the 105 nm thick h-BN and 6.5 meV for the 60 nm h-BN.

It is clear that the resonance linewidth reported for thicker (>200 nm) h-BN flakes becomes broadened for thinner flakes and strongly depends on the thickness. Therefore

the dielectric losses in h-BN strongly depend on sample geometry and surrounding flake thickness. The out-of plane phonon width was estimated by using a ratio of 3.5 between in-plane and out-of-plane width as reported in Refs. 78 and 83 for both very clean mono crystalline h-BN as well as for polycrystalline h-BN. Considering the strong thickness dependence of the phonon linewidth as seen in Fig. 3.9 these values are realistic. The phonon linewidths used to calculate the dielectric loss in Fig. 3.8 are 6.5 meV in-plane and 1.9 meV out-of-plane. A table with different models for the h-BN is shown in appendix A.1 in Table A.1.

The proposed combination of thermal phonon damping and dielectric losses[111] is in good agreement with our measurements (red curve in Fig. 3.8). Although the plasmon damping is affected by the dielectric losses, this work provides strong evidence of the intrinsic limit graphene plasmon inverse damping ratio of 40–70. This provides a upper bound on $\mathrm{Re}\,\sigma \sim 0.05\pi e^2/2h$ at room temperature, much smaller than previously reported.[50,51] This indicates that scattering in such high quality samples is effectively suppressed also for mid-infrared wavelengths and not only in the transport properties.

3.7. Conclusion

In this chapter we have demonstrated h-BN to be an exceptional environment for graphene plasmons, yielding high confinement and low levels of damping. We were able to show that plasmons can have a significantly lower damping than previously reported. In order to further reduce damping and reach the ultimate limit of plasmon propagation at room temperature—electron scattering by thermal phonons[111]—it will be necessary to reduce dielectric losses. This should be possible e.g. by improving the quality of thin h-BN films or by increasing the carrier density and exciting plasmons with higher energy further away from the reststrahlen bands of the h-BN. In order to further proof that indeed acoustic phonons in the graphene are responsible for the decay it would be extremely interesting to measure propagating graphene plasmons at cryogenic temperatures using a s-SNOM such as the ones in refs. 113,129. These measurements would give further insight into the origin of the graphene plasmon damping mechanisms in high quality graphene and could reach closer to intrinsic damping mechanisms such as electron-electron scattering.[112]

The presented device is ideal for applications where tunability and optical field confinement is crucial, such as for routing of plasmons,[27] plasmon lenses,[20,98] tunable sensors,[130] detectors and light-absorbers,[86,131] single-plasmon nonlinearities,[28] and strong light-matter interactions.[18,132] In the following chapter a phase modulator utilizing the high quality graphene and *in situ* tunability of its plasmons is introduced.

4. Plasmonic phase modulation with a small footprint

In this chapter we will use the unique in situ tunability of the graphene plasmon wavelength in order to show one of the first potential applications of graphene plasmons: a plasmonic phase shifter which is able to tune the light phase between 0 and 2π. With a footprint of only 350 nm it is more than 30 times smaller than the 10.6 μm light free space wavelength. Modulating the amplitude and phase of light is essential for applications such as wavefront shaping,[133] transformation optics,[20,134] phased arrays,[135] modulators[6] and sensors.[136] Performing this task with high efficiency and small footprint is a formidable challenge.[137–139] Metasurfaces[6,140] and plasmonics[141] is promising for reducing the footprint even below the free-space wavelength, but metals exhibit weak electro-optic effects. Two-dimensional materials, such as graphene, have shown promising performance as light modulators with small drive voltages.[142,143] The phase modulation is achieved by spatially controlling the graphene plasmon phase velocity and thus the optical path length. Due to three independent electric gates the spatial carrier density profile is tunable by electrostatic gating. We excite graphene plasmons at a sharp metal edge[98,144] and measure their propagation in the near field. We can explain our results qualitatively in terms of a simple model using the optical path length[105] and for a more quantitative understanding we use a complete scattering theory for plasmons propagating through spatial density profiles.[145]

Graphene plasmons are a versatile tool for integrated photonics and nano-optoelectronics as they provide extreme sub-wavelength confinement of light [29,30,100] while still offering a long lifetime approaching 1 ps. [100,102] The graphene plasmon phase velocity (and thus wavelength) is *in situ* tunable, and can be varied spatially, making it a unique platform for for transformation optics in two dimensions. [20,146] This has thus far remained a great challenge and the plasmon propagation was mainly controlled by physical features in the graphene. [96–98,101]

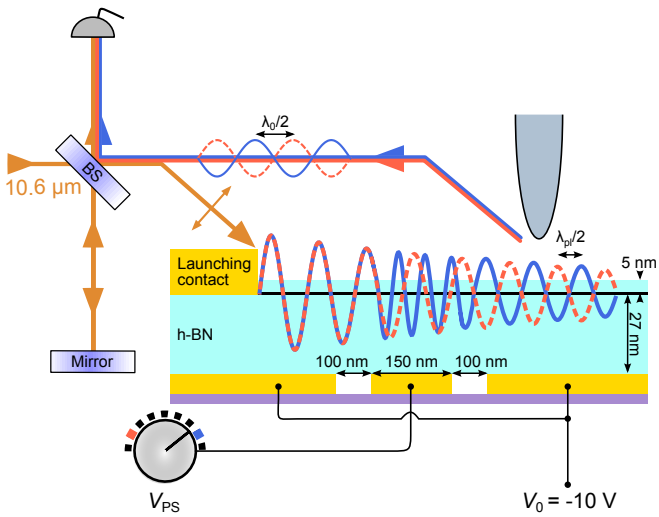

Fig. 4.1.: Device sketch and measurement principle. The three local gates are used to independently tune the carrier concentration in the different graphene regions. The phase shifter voltage V_{PS} is tuned and during all experiments $V_0 = -10\,V$ is kept constant. The left and the right local gate are kept at a gate voltage of $-10\,V$ for all experiments and the voltage of the central phase shifter gate is varied for achieving a phase shift. The gate thickness is 15 nm.The voltage applied to the three gates can be controlled independently. The plasmons propagate from the launching contact over the phase shifter region and are ultimately scattered into far-field light using a metallized AFM tip, and subsequently interfered with the incoming light.

Here, we manipulate for the first time the spatial profile of the plasmon phase velocity actively employing local metal gates, achieving *in situ* control of the plasmon wavelength, as sketched in Fig. 4.1. A plasmon (launched by scattering light on a gold edge) that propagates trough the tunable spatial carrier density profile picks up a phase, that is transferred to the photon after scattering of a metallized atomic force microscopy probe tip. In this way, we are able to steplessly tune the phase shift of the plasmon and the outcoming photons from 0 to 2π, and experimentally measure this phase in the far-field with an interferometer. [147,148]

We present a simple model based on the optical path length of light to explain our observations and to provide guidelines for designing such graphene plasmonic phase modulators. Moreover we rigorously calculate the expected phase shift and reflections using a Lippmann-Schwinger scattering theory approach. This strongly improved understanding of plasmonic phase-control is relevant for the future development of *in situ* tunable

metasurfaces,[149] modulators and holds great promise for novel sensor concepts.

4.1. Device

The device was fabricated by Yuanda Gao in the group of James Hone at Columbia University according to our input. Our device is based on a heterostructure of graphene encapsulated between two layers of hexagonal boron nitride (h-BN),[100,102] which serves to preserve the lifetime of the graphene plasmons. The device was assembled by the polymer-free van der Waals assembling technique[35] and then transferred onto 15 nm thin AuPd local gates. The so-called "phase shifter gate" has a length of 150 nm and the gaps to the other gates are 100 nm each. Using these local gates it is possible to spatially control the carrier density profile. A gold contact is connected by electrical side contact,[35] allowing for gating of the graphene.

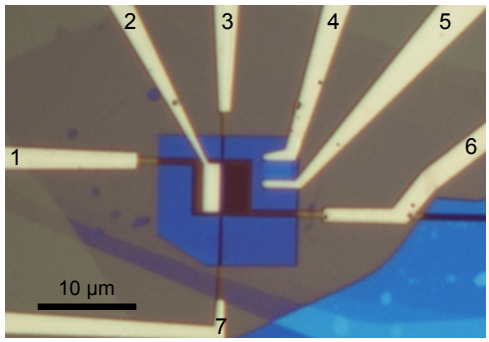

Fig. 4.2.: Microscope image of the device used for the study. The distance between the launching gate and the graphene edge is 2.6 µm. The large local gates can be gated by the contacts 1 and 6 on the left and right, respectively. Contacts 3 and 7 control the phase shifter gate voltage. Contact 2 is the side-contacted launching contact pad. Terminals 4 and 5 are contacts to another device on the same chip without local gates.

Fig. 4.2 shows an optical microscope image of the device used for the study. The launching contact, connected to terminal 2, can be seen on the left side. It has been fabricated according to the recipe described in Ref. 35. The optical illumination is from the left under an angle of $\sim 45°$, with polarization perpendicular to the edge of the launching contact. It is focused with a parabolic mirror onto the atomic force microscope probe tip.

The local metal gates are defined using electron beam lithography and 15 nm of a AuPd alloy is evaporated. The graphene and h-BN are first exfoliated onto a freshly cleaned substrate. The stack of h-BN/graphene/h-BN is then prepared using the polymer-free van der Waals assembling technique[35] and is transferred onto the local gates. Using electron beam lithography and reactive ion etching the graphene is shaped into a rectangle. Subsequently the launching contact is defined using electron beam lithography and evaporation of 75 nm Au.

4.2. Working principle

A CO_2 laser with a free space wavelength of $\lambda_0 = 10.6\,\mu m$ is focussed onto this elongated gold contact with a sharp edge. The polarization is perpendicular to the edge as sketched in Fig. 4.1. This edge provides the necessary momentum matching between far-field photons and plasmons and thus the light is partially converted into graphene plasmons propagating away from the edge as a plane wave in the electrostatically doped graphene. [98,144]

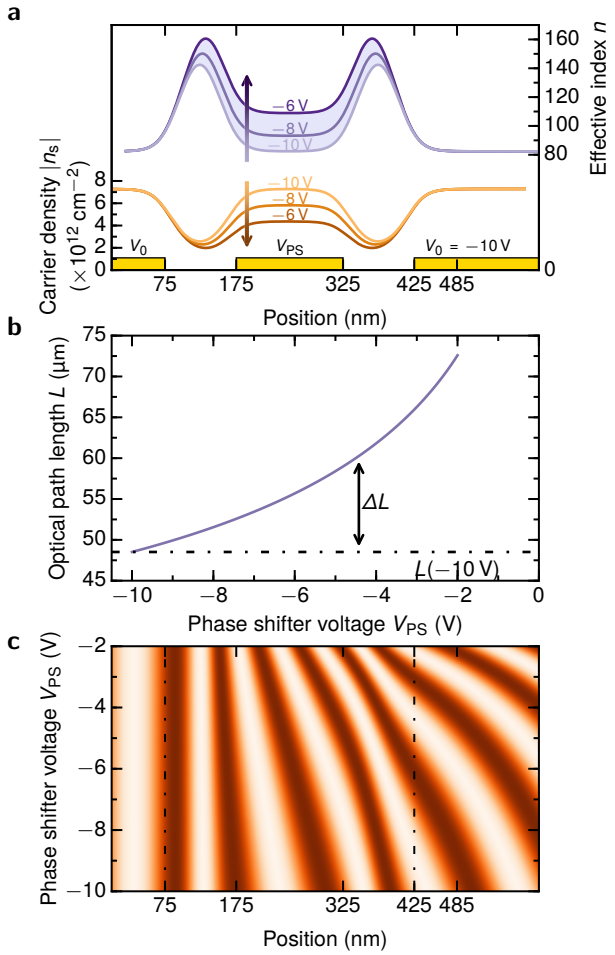

Fig. 4.3.: Working principle. **a**, Simulated spatial carrier density profile and the corresponding spatial profile of the plasmon effective index n, for a range of V_{PS}. Varying V_{PS} leads to different optical path lengths L. The shaded area indicates the optical path difference $\Delta L = 7\,\mu m$ between $V_{PS} = -10\,V$ and $V_{PS} = -6\,V$, equivalent to a phase shift of $\Delta\phi = 4/3\pi$ at $\lambda_0 = 10.6\,\mu m$. The position of the local gates is indicated at the bottom. **b**, Calculated optical path length L from 0 nm to 485 nm for a changing V_{PS} and a constant $V_0 = -10\,V$. The optical path difference for the different configurations is indicated as ΔL. **c**, Plasmons propagate from the left and start accumulating a different phase for different V_{PS} inside the phase shifting region (indicated by the two dashed lines) due to their different optical path lengths $L(V_{PS})$.

The effect of the plasmon propagation trough this spatial carrier density profile is depicted in Fig. 4.3a. The plasmon effective index $n = c/v_{ph}$, with v_{ph} the plasmon phase velocity and c the speed of light, is related to the gate-induced charge density: $v_{ph} \propto \lambda_{pl} \propto \sqrt{n_s}$.[8,18,24,25,150] The voltage on the phase shifter gate V_{PS} controls n in the graphene above this gate. After the plasmons propagate through this velocity-tunable (and thus phase-shifting) region their optical path length (Fig. 4.3b) can be expressed as

$$L(V_{PS}) = \int_a^b n(x, V_{PS}) dx \tag{4.1}$$

where x is the position and $a = 0\,\text{nm}$ and $b = 485\,\text{nm}$ are the start and end points of the phase-shifting region respectively,[105] where the carrier density profile does not change any more when V_{PS} is changed.

The carrier density profile is simulated by the electrostatic Laplace equation taking into account the full anisotropic DC permittivity of h-BN as well as the spatial gate profile.[151] For each V_{PS} the carrier density profile is simulated and $n(x, V_{PS})$ is then calculated taking into account the full dielectric environment. The carrier-density-dependent graphene conductivity is calculated using the zero-temperature non-local random phase approximation.[8,18,24,25,150] As the out-of-plane decay length of the plasmons is much smaller than the thickness of the bottom h-BN the spatial profile of the metal gates does not need to be taken into account.

Due to the different optical path lengths for different V_{PS} the plasmons accumulate a different phase ϕ after propagating through the phase shifter region. The phase difference $\Delta\phi$ between different optical path lengths can be estimated using the optical path difference,

$$\Delta\phi(V_{PS}) = k_0 \Delta L = k_0 \left(L(V_{PS}) - L(-10\,\text{V}) \right). \tag{4.2}$$

In Fig. 4.3c we show how the optical path difference ΔL translates into a different phase for different V_{PS} as they exit the phase shifter region. The wavelength reduction in the phase shifter region is clear.

4.3. Measurements and Result

In order to experimentally observe the phase shift between different V_{PS} we use a metallized atomic force microscopy probe tip to scan across the sample. The plasmons are scattered from the probe tip and then recorded as the out-scattered light signal in the far-field by scattering-type scanning near-field optical microscopy (s-SNOM) (Fig. 4.1). The measurement is performed in homodyne configuration, where the light passes trough interferometric arms with a constant length. While scanning the tip across the sample we observe a plasmon fringe pattern, as shown in Fig. 4.4a), with the full plasmon wavelength λ_{pl} launched by the sharp metal edge on the left. This fringe pattern is measured because the incident electric field interferes with the plasmon field.[98,144] We do not observe any plasmons reflected by the gold contact. We also observe a fringe pattern with $\lambda_{pl}/2$ at the graphene edge due to edge reflected plasmons interfering with the plasmons launched by the tip.[29,30,100] The extracted plasmon wavelength at a gate voltage of $V_0 = -10\,\text{V}$ is $\lambda_{pl} \approx 126\,\text{nm}$ for both launched and reflected plasmons (Fig. 4.4a), in good agreement with the theoretically calculated 128 nm.[100]

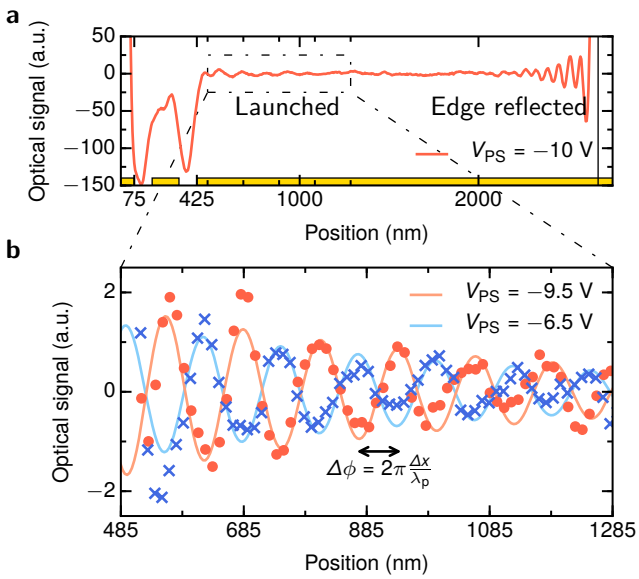

Fig. 4.4.: Measurement of full device and a phase shift of π. a, Optical signal of the full device with the launching contact at 0 nm and the position of all the gates indicated. For clarity a polynomial background was subtracted. The edge of the graphene is indicated as vertical solid line at 2670 nm. **b**, Measurement (data points) and fits (solid lines) of the absolute value of the fourth harmonic of the optical signal with a smoothed optical signal background subtracted from both. The phase shift between $V_{PS} = -9.5\,V$ and $V_{PS} = -6.5\,V$ is $(1.04 \pm 0.11)\pi$.

By changing V_{PS} we observe a change in position of the launched plasmon fringes to the right of the phase shifter region (Fig. 4.4b). The phase shift can be extracted from the data using the simple relationship $\Delta\phi = k_{pl}\Delta x$, with $k_{pl} = 2\pi/\lambda_{pl}$. We find that the wavelength of the plasmons to the right of the phase shifting region is independent of V_{PS}. This confirms that that the carrier density is well defined for the region where we extract the light phase, and that the phase-shift only occurs in the phase-shifting region for positions from 100 to 350 nm.

In order to extract ϕ for different V_{PS} we remove the background optical signal by subtracting the smoothed optical signal both from data and fitting function. We then fit launched and edge reflected fringes using $\mathrm{Re}(re^{i\phi}e^{ikx})$, where ϕ is the phase we are interested in and r a real valued amplitude. The plasmon wavevector $k = k_{pl} + k_i i = 2\pi/126\,\mathrm{nm} - 1.5\mathrm{i}\,\mu\mathrm{m}^{-1}$ is fixed in order to capture the phase fully in ϕ. The extracted inverse damping ratio $\gamma_{pl}^{-1} = k_{pl}/k_i \sim 30$ is in accordance with previous studies on high quality graphene encapsulated in h-BN at room temperature.[100,102] In order to compensate for small drifts in the interferometric arm length which can lead to a change in the fringe position, we measure the phase of the launched plasmons relative to the phase of the edge reflected plasmons. The edge reflected plasmons are not influenced by V_{PS} as the graphene edge is ∼2.7 µm away (and thus more than the plasmon decay length) from the phase shifter gate (Fig. 4.4a). The phase of the edge reflected plasmons is measured relative to the graphene edge from the simultaneously measured topography.[100]

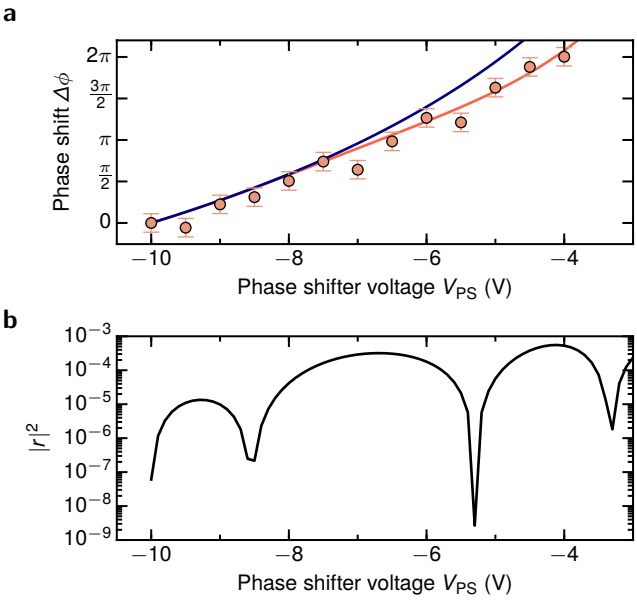

Fig. 4.5.: Phase shift $\Delta\phi$ and reflection magnitude. **a** Calculated and measured phase shift with respect to the phase of the transmitted plasmon at a gate voltage of $-10\,\mathrm{V}$ applied to both the large gates and the phase shifter gate. The blue line is the phase shift calculated from $\Delta\phi = k_0\Delta L$ using the calculated optical path difference ΔL. The red line is the phase shift calculated from Lippmann-Schwinger theory.[145] The error bar length of $\pm 0.11\pi$ is the standard deviation of the extracted phase of the launched plasmon for 12 measurements with $V_{PS} = V_0 = -10\,\mathrm{V}$. **b** Calculated reflection magnitude from the phase shifting device for a plane wave plasmon coming in from the left, i.e. from the direction of the launching structure in Fig. 4.1.

In Fig. 4.5a we show the measured phase shift $\Delta\phi$ relative to the plasmon phase measured at $V_{PS} = V_0 = -10\,\mathrm{V}$. We observe a fully tunable phase shift from 0 to 2π for a 6 V range. The blue line is the phase shift calculated from the optical path length approximation (OPLA)[105] using eq. 4.2, without fitting parameters. A good agreement with experiments is reached for small $V_{PS} - V_0$ but stronger deviation is clearly visible for larger $V_{PS} - V_0$. In section 4.4 we explain how this discrepancy can be explained and how a more sophisticated model gives a complete agreement between theory and experiment.

4.3.1. Measurement details

The s-SNOM used was a NeaSNOM from Neaspec GmbH, equipped with a CO_2 laser operated at 10.6 µm with $\sim$ 20 mW power. The metallized probes were commercially-available atomic force microscopy probes with an apex radius of ~ 25 nm. The tip height was modulated at $\sim$ 250 kHz with $\sim$ 100 nm amplitude. The probe tip was electrically grounded. The beam splitter used is a ZnSe window. The measurements were all performed at ambient conditions and room temperature. In order to have a background free signal the fourth harmonic of the scattered light signal was used. The spacing between the pixels is 3.9 nm and the integration time per pixel 13 ms. The gate capacitance density is $7.29 \times 10^{11}\ e\,\mathrm{cm}^{-2}\,\mathrm{V}^{-1}$, where e is the elementary charge. The h-BN DC permittivity

is 6.7 in-plane and 3.56 out-of-plane and the permittivity at 10.6 µm is $8.341 + 0.023i$ in-plane and $1.932 + 0.006i$ out-of-plane.[100]

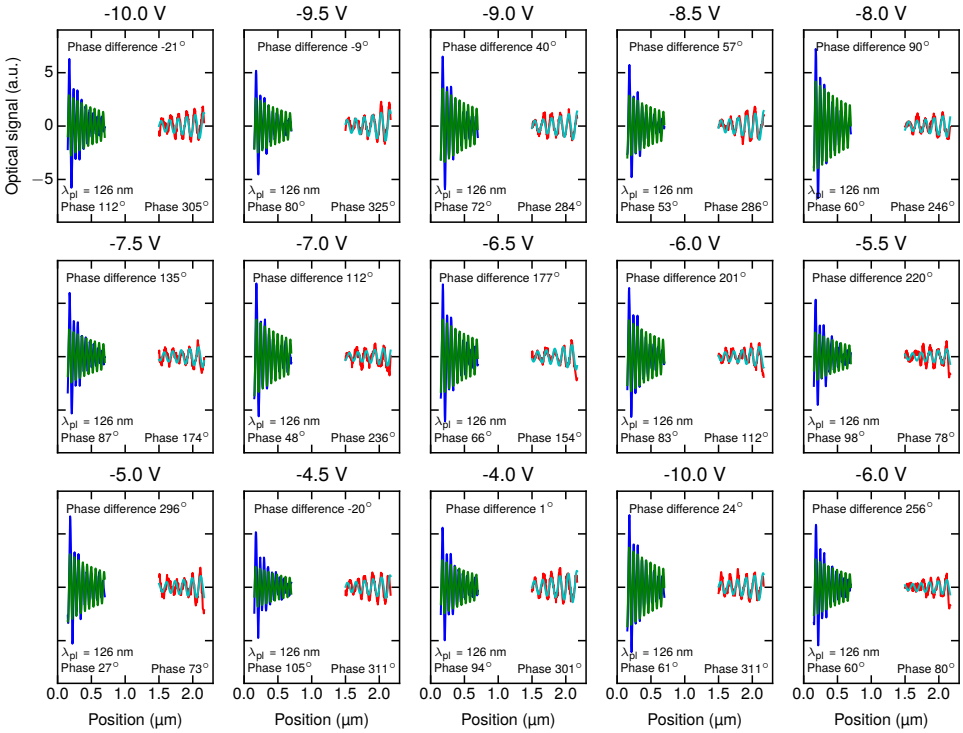

Fig. 4.6.: Experimentally measured plasmon signals. Measured edge-reflected (blue line) and pad-launched (red line) plasmon signals, and their respective best-fits (green and light blue lines) for different values of the phase-shifter gate voltage between −10 V and −4 V. All the other gates are held at −10 V. For the sake of clarity the two signals are shown closer in space than they actually are.

In Fig. 4.6 we show the raw data of the launched as well as edge reflected plasmons and the corresponding fits. It is clear that the fits and data agree well.

As explained we fit both reflected and launched fringes using $\mathrm{Re}(ae^{i\phi}e^{ikx})$, where ϕ is the phase we are interested in and a is a real valued amplitude and we keep the plasmon wavevector $k = k_{\mathrm{pl}} + k_{\mathrm{i}}i = 2\pi/126\,\mathrm{nm} - 1.5\mathrm{i}\,\mu\mathrm{m}^{-1}$ constant for all fits. This guarantees that the phase of the fringes is fully captured in ϕ. The position of the graphene edge is measured from the simultaneously acquired topography and is used as reference point. This enables us to use the phase of the edge reflected fringes as an absolute reference to compensate for potential drifts in the length of one of the interferometric arms which would lead to an observed change in fringe position in absence of an actual change of the plasmon phase.

4.4. Lippmann-Schwinger scattering theory

In order to quantitatively understand the behaviour of the phase shift, we employ a scattering approach that parallels Lippmann-Schwinger single-particle quantum scattering theory, which we termed Lippmann-Schwinger-Random Phase Approximation (LS-RPA). This approach reduces to the OPLA when the plasmon wavelength is much smaller than the length scale over which the carrier density changes. As for our device, these two lengthscales are comparable, the LS-RPA approach is required. This approach has been developed by Iacopo Torre and Marco Polini at IIT and is explored in great detail in ref. 145.

Numerical results obtained with the LS-RPA approach as shown in Fig. 4.5a are in excellent agreement with experimental data. The essence of the LS-RPA approach is the following: We start by considering an inhomogeneous system where spatial variations of the carrier density profile are confined to a limited region of space. Outside this region plasmon modes that freely propagate as plane waves are supported, which can be used to define incoming and outgoing plasmonic "states".[145] Complex transmission and reflection coefficients are evaluated from a long-wavelength expansion of the proper density-density linear response function. This is the point where the Random Phase Approximation (RPA) for an inhomogeneous electron system[145] is carried out, to approximate the proper density response function with the non-interacting one. Keeping only the leading term in the long-wavelength limit, one recovers the local approximation,[152] where only the local frequency-dependent conductivity function matters. A more quantitative understanding of the data, however, requires the first non-local correction to the long-wavelength expansion.[145]

Using this approach we also calculate the expected reflection coefficient $|r|^2$ for this device which is very small (Fig. 4.5b), owing to the smooth change of the plasmon wavelength. This makes this type of device an ideal candidate as a modulator as unwanted reflections are minimal. Indeed we do not observe plasmons reflected by the split gate as there are no plasmon fringes with spacing $\lambda_{\mathrm{pl}}/2$ observed next to the phase shifting region.

4.5. Equivalent circuit model

One important characteristic of a phase modulator is the half-wave voltage V_π, the voltage that needs to be applied to change the phase by π. Smaller voltages means more efficient operation. The voltage-length product $V_\pi l$ reached is 2.5 V µm, more than an order of magnitude smaller than for plasmonic phase modulators based on other materials.[153] By decreasing the thickness of the bottom h-BN V_π can even be further reduced. We have modelled our modulator using an equivalent circuit model (Fig. 4.7a) and find that the RC switching time can be up to ~ 1 THz, but the real switching time will be limited be limited by other processes. In Fig. 4.7b we see the frequency response of the system. The frequency cutoff of this equivalent circuit model is above ~ 1 THz for these device parameters. We remark that the coupling efficiency from light to plasmons for these devices is very low. Improved matching schemes and resonant structures[149] are required for the development of practical modulators or metasurfaces.

We estimate the frequency response by modelling our device with an equivalent circuit. The software used is LTspice IV 4.23. In Fig. 4.7a we show the model. The contact resistance R_{contact} is a relevant parameter and should be kept small. The value of 220 Ω was calculated from a contact resistance of 1000 Ω µm, which is well within technical ca-

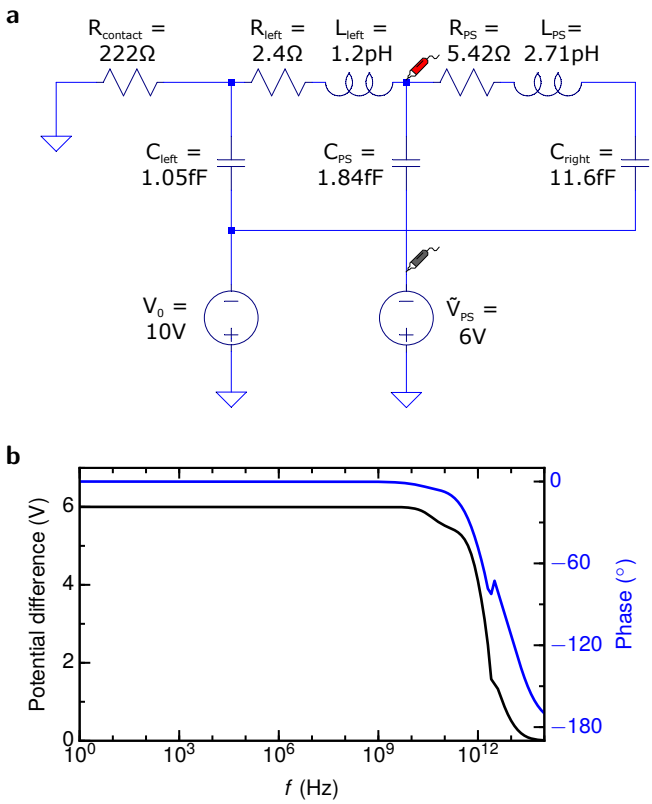

Fig. 4.7.: Equivalent circuit model of the phase modulator. **a** Scheme of the equivalent circuit model with definitions of all the parameters. The potential difference is measured between the two voltage probes indicated in red and grey. **b** Bode plot of the frequency response of the potential difference between the voltage source and the phase shifter gate.

pabilities and easily reachable for typical edge contacted graphene devices.[35] The assumed channel width was 4.5 µm. In order to calculate the resistances and inductances in Fig. 4.7a we used the Drude conductivity of graphene with a carrier lifetime of 500 fs, and for the capacitances a relative d.c. permittivity of h-BN of 3.56. The simulated length of the left, center, and right gate is 350 nm, 350 nm, and 2.2 µm respectively. The voltage applied to the left and right gate are 10 V and 6 V to the phase shifter gate in order to simulate a phase shift of π.

4.6. Conclusions

To conclude, we have implemented a novel approach for ultra-compact voltage-tunable plasmonic phase control by spatially controlling the graphene plasmon phase velocity. By decreasing the gap size between the phase shifter gate and the other gates it will be possible to even further decrease the footprint of such a modulator. By pushing towards higher carrier concentrations it could be possible to build such modulators in the technologically relevant telecommunication wavelength range around 1.5 µm, as near-infrared plasmons

have recently been observed.[154,155] The same type of device could also be used for amplitude modulation of light[156] or on-chip sensing by plasmon interferometry. The device also enables extremely small footprint interferometers for example in Mach-Zehnder configuration for plasmonic biosensing. By nano-structuring the phase shifting region, it would be possible to make phased arrays to control, steer and focus light *in situ* on the nanoscale.[149] This work thus constitutes a first step towards two-dimensional transformation optics[20] which can be employed for ultra-compact phase modulators[137] and biosensing.[21]

II

Near-field photocurrent nanoscopy

In this part of the thesis an introduction to photocurrent in graphene is given. A focus is put on the photothermoelectric effect as it dominates in the experiments introduced after. An overview over different ways of measuring photocurrent is given and near-field photocurrent nanoscopy based on s-SNOM is introduced as a new tool to measure photocurrent with a wavelength independent resolution. In the following chapter it is shown how near-field photocurrent nanoscopy can be used to access different optoelectronic properties of graphene at the nanoscale. Then it is presented how we can electrically detect graphene plasmons in the mid-infrared and terahertz using this technique. Finally electrical detection of hyperbolic phonon polaritons in hexagonal boron nitride and how this can be exploited to greatly enhance the photoresponse of graphene photodetectors in the mid-infrared is introduced.

5. Background

Photodetectors are an essential technology with far-reaching applications from optical communication to biomedical sensing.[157,158] Graphene photodetectors are promising due to their broadband absorption, fast response time,[53,66,159] potential flexibility[160] and large area production capabilities.[161] Furthermore the possible integration of graphene with existing CMOS-technology could enable rapid development of and integration into production of graphene photodetectors.[63] In the next sections I will introduce the photo-thermoelectric effect which is responsible for photocurrent generation of the devices and measurements introduced in the following chapters.

5.1. Photocurrent generation via the photo-thermoelectric effect

In graphene, the dominant mechanism that gives rise to photocurrent I_{PC} is typically the photo-thermoelectric effect (PTE).[158] It has been shown to dominate from the visible[162] to the mid-infrared[163,164] in many different experimental configurations, such as at contacts,[164] single/bilayer interfaces[54,165] and pn-junctions.[162,166] The photo-thermoelectric effect is a very prominent effect for graphene photodetectors. Photoexcited hot electrons can create a photovoltage V_{PTE} due to the Seebeck effect.[158] Because in the case of the PTE the electronic system is heated extremely high bandwidths can be achieved.[53]

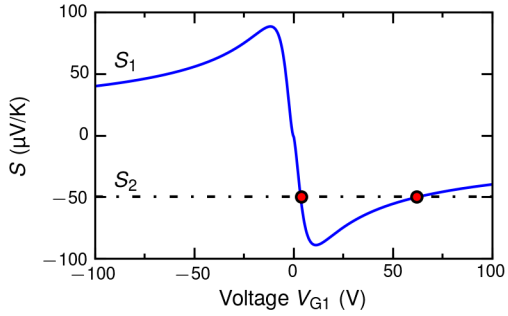

Fig. 5.1.: Seebeck coefficient calculated for graphene using the Mott formula. The blue solid curve indicates the carrier density dependent Seebeck coefficient calculated using the Mott formula as a function of gate voltage V_{G1}. The black dashed dotted line is the Seebeck coefficient for a fixed doping. The positions of the sign change are indicated with red circles both here and in Fig. 5.2.

In simple terms the PTE in graphene can be described as $I_{PC} \propto (S_2 - S_1)\Delta T$, where $S_{1,2}$ are the Seebeck coefficients in two graphene regions and ΔT the difference in electronic temperature between the two regions.

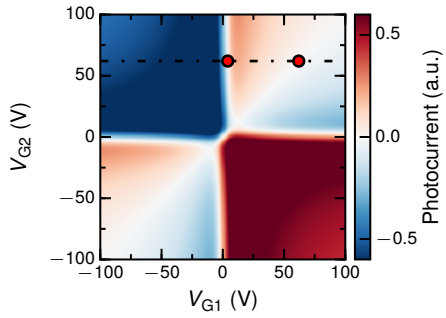

Fig. 5.2.: Calculated six-fold pattern of the photocurrent in graphene indicating the thermoelectric origin. The multiple changes of sign are a clear indication of a photo-thermoelectric origin of the photocurrent. At $V_{G2} \sim 62\,\mathrm{V}$ we find $S_2 = -50\,\mu\mathrm{V/K}$ as shown in Fig. 5.1. The positions of the sign changes are indicated with red circles.

More accurately the current I_{PC} induced due to the photo-thermoelectric effect can be calculated by:[162,167]

$$I_{PC} = \frac{1}{RW} \iint \frac{\partial T(x,y)}{\partial x} S(x,y)\, dxdy \tag{5.1}$$

where R is the total resistance including graphene, contacts and circuitry, W the device width and x the current flow direction. T is the optically induced electron temperature and S the spatially varying Seebeck coefficient in graphene. This simple formula is valid only for rectangular graphene devices and special care needs to be taken for arbitrary shapes.[168]

In graphene the Seebeck coefficient is dependent on the electrical conductivity σ is described by the Mott formula:[167,169,170]

$$S = -\frac{\pi^2 k_B^2 T}{3|e|} \frac{1}{\sigma} \frac{d\sigma}{dE}\bigg|_{E=E_F} \tag{5.2}$$

where e is the electron charge and k_B is the Boltzmann constant. A calculated gate dependent Seebeck coefficient is shown in Fig. 5.1. We can see a clear non-monotonic behaviour of the Seebeck coefficient.

It is evident that by changing the gate voltage and thus the Seebeck coefficient it is possible to tune the photocurrent according to eq. (5.1). Indeed in the case of two independently tunable gates it is possible to observe a so-called six-fold pattern (Fig. 5.2) in the gate dependence of the photocurrent. The double sign change is due to the non-monotonic behaviour of the Seebeck coefficient. As $I_{PC} \propto S_2 - S_1$ it is clear that there are two sign changes of the photocurrent associated with the configuration shown in Fig. 5.1 where S_2 is constant and S_1 is changing according to eq. (5.2). The first sign change is expected at $V_{G1} \sim 4\,\mathrm{V}$ and the second one at $V_{G1} \sim 62\,\mathrm{V}$. These voltages are marked with red circles both in Fig. 5.1 and 5.2 and indeed the sign changes are observed. This six-fold pattern is a clear evidence that a PTE is measured and not a photovoltaic effect for which only a single sign change is observed.[167]

5.1.1. Carrier dynamics in graphene

The carrier dynamics upon shining light onto graphene are relevant for understanding the process of photocurrent generation in graphene. The heating dynamics are important to know the temperature of the electron system and the cooling dynamics in order to know how long hot carriers live and thus how much photocurrent is generated. In Fig. 5.3 we show what determines these carrier dynamics. Directly after the excitation, there is a non-equilibrium, non-thermal distribution, but within $\sim$ 100 fs, there is a quasi-equilibrium, thermal distribution with an elevated electron temperature (broadened Fermi-Dirac distribution).[53] After this the carriers cool down through different mechanisms, which are briefly introduced in the following.

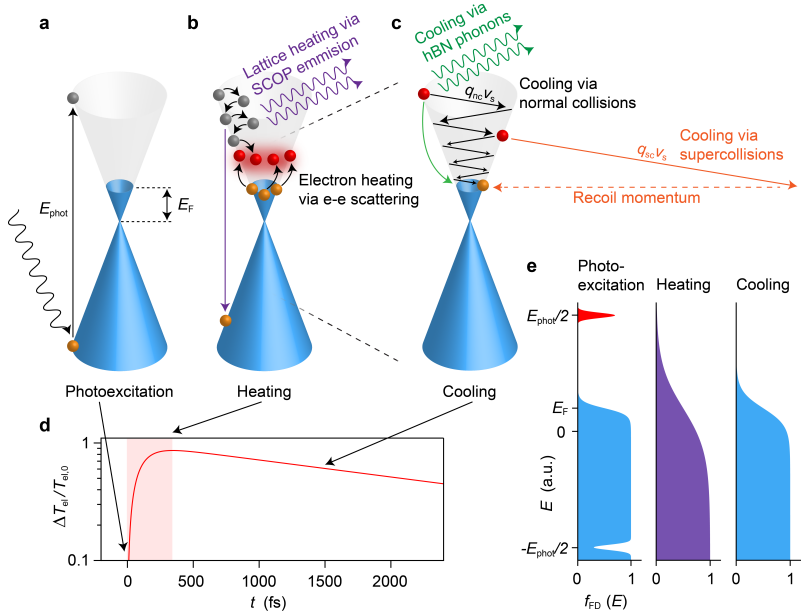

Fig. 5.3.: Hot carrier dynamics in graphene. **a** A photon with energy E_{phot} gets absorbed generating an electron-hole pair. **b** Part of the electron energy is transferred to the electron system via scattering with other electrons forming a hot-electron gas. Strongly coupled optical phonons (SCOPs) transfer part of the energy to the lattice.[171] **c** The hot-electron gas then cools down with different mechanisms. It can cool down through emitting phonons to the substrate. And it can cool via normal-collision or super-collision cooling. **d** The time development of the electron temperature increase ΔT_{el} showing the creation of hot-electron gas and the time dynamics of the cooling.[53] **e** The Fermi-Dirac distribution $f_{FD}(E)$ is out of equilibrium due to the photoexcitation (Photoexciation). The electron temperature is increased due to the hot electrons (Heating). While cooling down the initial Fermi-Dirac distribution is being restored (Cooling). (This figure is copied with permission from ref. 172)

Substrate cooling is an efficient cooling pathway for hot electrons in graphene by the graphene coupling with polar phonons in the substrate, such as SiO_2.[173] It is indeed one of the most dominant cooling mechanisms and associated with the g value introduced in section 6.1.[173,174] More recently also h-BN hyperbolic phonon

polaritons have been shown to be an efficient way to cool the electron system of the graphene.[174]

Super-collision cooling is due to disorder-mediated scattering in graphene and is known to be a limiting factor for cooling of hot-electrons in graphene.[175–177]

Normal-collision cooling is due to hot electrons releasing their energy via momentum-conserving scattering with acoustic phonons of the graphene lattice and thus thermalizing with the lattice. These normal-collisions are expected to happen on a nanosecond timescale and are considered to be the intrinsic limit of l_{cool} in graphene.[178] However the mechanisms discussed before are typically much faster and thus normal-collision cooling only plays a minor role for hot-electron cooling in graphene.

All of these cooling mechanisms determine the cooling length l_{cool} of hot-electrons in graphene and thus influence the resolution of the near-field photocurrent technique as described in section 6.1.

5.2. Mid-infrared photodetection in graphene

The mid-infrared frequency range is a technologically extremely important range for a manifold of applications ranging from biomedical sensing to thermal imaging.[158] This is because the vibrational modes of many molecules fall into the mid-infrared range which makes it an ideal range for spectroscopy of biological samples. Furthermore thermal radiation emitted from warm objects falls into this range.

Graphene photocurrent generation in the mid-infrared has been studied extensively with different origins.[87,163,164,179–182] The main photocurrent generation mechanisms for graphene devices without applied bias voltage in the mid-infrared is just like in the visible spectral region the photothermoelectric effect.[163] As direct absorption of graphene in the mid-infared is low due to Pauli blocking (see section 1.2) different ways to increase the absorption of graphene and thus the sensitivity of photodetectors have been explored. Different ways to improve the responsivity of graphene photodetectors in the mid-infrared are by exciting plasmons in nanostructured graphene[87] or by surface phonons in the substrate.[164,180]

As the PTE in graphene can be very fast[53] detectors based on this effect will allow high bandwidth mid-infrared detection using graphene. Also the other advantages of graphene photodetectors such as their tunability, potential flexibility and integration with existing CMOS-technology translates directly into the mid-infrared.[157]

5.2.1. Scanning mid-infrared photocurrent setup

In order to measure spatially resolved photocurrent maps in the mid-infrared we built a scanning photocurrent measurement setup in which the photoresponse of graphene devices can be measured spatially resolved. It is used for far-field measurements of the encapsulated graphene photodetectors discussed in chap. 9. A sketch of the setup is shown in Fig. 5.4. The light source used is a monochromatic quantum cascade laser (QCL) tunable from 6-10 µm wavelength (Block Engineering Laser Scope). In order to improve the signal to noise level of the measurements we measure the photocurrent using lock-in amplification.

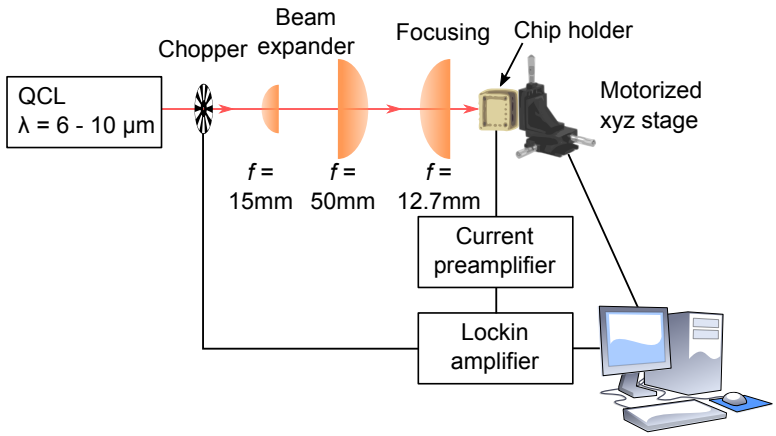

Fig. 5.4.: Scanning mid-infrared photocurrent setup. Far-field setup used to measure the spatial photocurrent pattern in graphene infrared photodetectors. ZnSe lenses with different focal lengths f are used to build a telescope setup in the mid-infrared in order to increase the beam diameter to ultimately be able to focus the light more tightly.

For this the light is modulated using a mechanical chopper, typically at a frequency of 423 Hz.

The light is focussed using a ZnSe lens system to a spot size with a full width at half maximum of about twice the light wavelength. This is achieved by placing a beam expander before the focusing lens in order to increase the numerical aperture of the focusing optics. The sample is mounted onto a motorized xyz-stage with micrometer precision control over the position. As the focal position of the laser spot at the sample position depends on the wavelength due to the dispersion of ZnSe in the mid-infrared the position of the sample has to be corrected as a function of wavelength. In the setup it is also possible to acquire transmission at the same time but this feature is not used in the following experiments.

The setup is inside a box which can be flushed with nitrogen gas in order to have a dry atmosphere to avoid absorption by water vapour which is very prominent in our wavelength range.

6. Near-field photocurrent nanoscopy

One of the major drawbacks of the far-field setup described in section 5.2.1 is that its resolution is limited by the diffraction limit and thus for the case of mid-infrared light to a length scale on the order of tens of micrometers. For many applications especially when characterizing optoelectronic properties of graphene this is not sufficient and a much higher spatial resolution is desired.

Moreover other existing technologies for determining the optoelectronic properties of graphene can have one or more of the following drawbacks. Available techniques are invasive,[183] rely on specifically designed device structures,[184–186] image only very small areas,[58,59,185,187–189] rely on high doping of the graphene,[96] need unhindered electrical access of the probe to the graphene,[58,59,185,187,188] or lack the desired nanometer resolution[190] and are generally difficult to implement. Therefore, a nanoscopic tool that probes both electrical and optical response of graphene devices at nanometer length scales is highly desired. For example the commonly used Raman microscopy[190] is an excellent tool to spatially study large area graphene but as a diffraction limited technique it lacks the possibility to optimally resolve nanoscale features such as grain boundaries[183,184] or charge puddles.

Scanning near-field photocurrent nanoscopy,[191–194] with nanometer resolution at infrared frequencies is a new technique developed to characterize optoelectronic devices overcoming many of the drawbacks of other techniques described before. The technique allows us to directly measure the optoelectronic properties of graphene devices that affect their performance spatially resolved. It is fully non-invasive and can be applied to devices that are used later-on for real applications. In addition, the mid-infrared frequency range inhibits photodoping effects,[126] and enables the characterization of encapsulated devices. It is a promising tool performing measurements at room temperature and ambient conditions with nanometer spatial resolution and without the need of special treatment or device geometries.[2,36] In general, this technique operates most effectively with mid-infrared light because it does not lead to photodoping in the case of graphene[126] and it is more stable in operation, compared to visible light.

The measurement principle is sketched in Fig. 6.1. The setup is based on a scattering-type scanning near-field optical microscope (s-SNOM)[30,36,96,98–100,117] augmented with electrical contact to the sample to measure currents *in situ*. For scanning near-field infrared photocurrent nanoscopy we do not measure the outscattered light signal but rather directly measure current induced by the near-field as explained in the following. A mid-infrared laser illuminates a metallized atomic force microscope probe, which is tapping at its mechanical resonance frequency Ω. A part of the incoming light, which is polarized parallel to the shaft of the probe, excites a strong near-field at the tip apex due to an antenna effect.[36] This near-field is on the order of 25 nm, limited only by the tip radius and is completely wavelength independent.[2,36]

The near and far fields impinging on the device induce charge flows in the device mainly due to the photo-thermoelectric effect. They drive currents into an external current am-

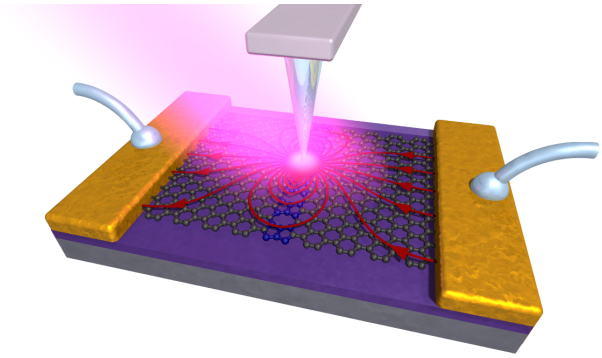

Fig. 6.1.: Sketch of the scattering-type scanning near-field optical microscope setup working principle. A mid-infrared laser illuminates the atomic force microscope tip and generates a near-field at the tip apex. The near-field is absorbed by the graphene and heats charge carriers in the graphene which consequently leads to a position dependent photocurrent in the graphene. The blue region in the graphene lattice represents a grain boundary with a modified Seebeck coefficient which leads to a net current flow. In the measurements for each position only magnitude and direction of the current can be measured. This sketch for illustrative reasons shows photocurrent at a grain boundary but the technique is not limited to this system as will be shown in detail in the following chapter. The sketch of the working principle is not to scale.

plifier via attached contacts on the device. We isolate the part of the current that is induced by near fields by demodulating the current at the second harmonic of the tip tapping frequency using a lock-in technique.[36] This demodulated current is denoted I_{PC} and referred to as near-field photocurrent. It is obtained together with near-field optical and topography information which can be used for obtaining complementary information.

As to the physical mechanism of the photocurrent, we consider the photo-thermoelectric effect that has been shown to dominate the photoresponse of graphene from the visible to the infrared. See for example refs. 54,158,162,164,166,167. The light (in this case, the tip-enhanced near-field) locally heats the graphene, and this heat acts via non-uniformities in Seebeck coefficient S to drive charge currents within the device and into the contacts. Therefore, we interpret the variations of I_{PC} in terms of microscopic variations in S. The Seebeck coefficient, which depends on material properties such as carrier density and mobility, is a measure of the electromotive force driven by a temperature difference in a material. A complete description of I_{PC} needs to take into account the carrier cooling length[162,167] and overall sample geometry.[168] A quantitative model of the thermoelectric photocurrent mechanism can be found in section 5.1.

6.1. Limits of the resolution

As explained before the advantage of the near field photocurrent technique presented here is that the spatial resolution is unaffected by light diffraction length scales, and instead limited by the ~ 25 nm near field extension due to the tip apex radius.

Also the cooling length l_{cool} of charge carriers in graphene influences the resolution. The carrier cooling length l_{cool} is determined by an interplay of carrier cooling via internal and

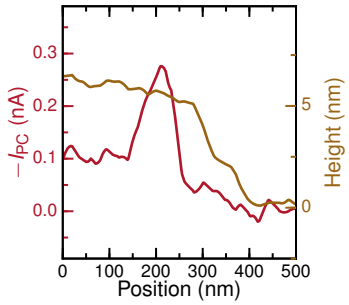

Fig. 6.2.: Spatial resolution of near-field photocurrent nanoscopy. Topography (brown) and near-field photocurrent (red) at an edge of graphene on top of a self assembled monolayer. The photocurrent going to zero over a similar distance as the topography shows that the photocurrent resolution is on the order of the size of the probe tip shows the extremely high spatial resolution of the technique.

external parameters as described in section 5.1.1. The carrier cooling length $l_{cool} = \sqrt{\kappa/g}$, where κ the thermal conductivity in plane and g the thermal conductivity out-of-plane to the heat sinking substrate, describes how far heat propagates through the charge carriers, before dissipating to the environment.[167] Thus in the case of a constant coupling efficiency of the near-field to the graphene any feature will be limited in resolution by the cooling length. The fact that a larger l_{cool} leads to a reduced resolution indeed means that for higher quality graphene which has a larger l_{cool} our technique has a worse resolution than for low quality graphene.

Fig. 6.2 shows a near-field photocurrent measurement at a graphene edge. The wavelength of the light used is 10.6 µm while we observe features in the photocurrent at similar nanometer size scales as the sample topography. We can quantify the resolution by observing the change in I_{PC} as the tip is moved over the edge of graphene. The full width at half maximum of the photocurrent peak at this location is ∼100 nm, matching the rise distance in the topographic signal. This resolution is indeed comparable to the tip radius of ∼ 25 nm, and more than two order of magnitude below any limits relating to the 10 µm free space light wavelength.[195] It has also been shown that this high resolution extends until the terahertz spectral range with light wavelengths on the order of ∼100 µm where the observed resolution is still only 50 nm.[116] In the case of Fig. 6.2 and ref. 116 the measurements have been performed on low quality graphene grown with chemical vapor deposition and thus a very short cooling length leading to the high resolution achieved.

6.1.1. Model of the temperature profile

For the temperature profile $T(x)$ we consider that the heat spreads in two dimensions with heat sinking to lattice and substrate, producing a $T(x)$ profile described by a modified Bessel function of the second kind, with a finite tip size correction (Fig. 6.3).

In order to describe the photocurrent in graphene with a model it is of great importance to correctly describe the heat profile within the graphene as the heat profile in combination with the Seebeck profile lead to the photocurrent pattern.

Graphene on top of a substrate is a two dimensional material with the substrate acting

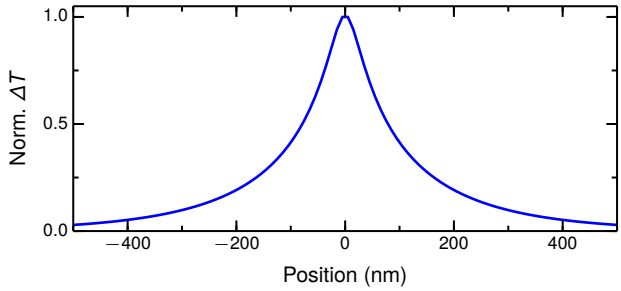

Fig. 6.3.: Temperature profile created in an infinite graphene sheet with a cooling length $l_{\text{cool}} = 200\,\text{nm}$ and a finite tip size correction of 25 nm shows the heat change profile ΔT generated by the near-field in the graphene.

as a heat sink, as for typical substrate materials, such as SiO_2, the thermal conductivity is much larger than for air. The two dimensional heat equation in steady state with an additional term for heat sinking can be written as:

$$0 = \kappa \nabla^2 T_{\text{el}} + P - g(T_{\text{el}} - T_{\text{s}}), \tag{6.1}$$

where T_{el} is the electron temperature, T_{s} is the constant heat sink temperature, κ the thermal conductivity in plane, g the thermal conductivity out of plane to the heat sinking substrate and P the power density of the heat source.

In using this equation, we assume that the electron heat cools to the lattice, but then that the lattice can pass on any heat much more easily to substrate. In that way the temperature of the lattice does not change significantly. This is convenient because the lattice itself has a different thermal length which would complicate matters.

If we take the two-dimensional case and a point source for P,

$$P = P_{\text{total}} \delta(x)\delta(y) \tag{6.2}$$

then the solution of the two dimensional heat equation eq. (6.1) turns out to be:

$$T_{\text{spot}} = T_0 K_0 \left(\frac{|r|}{l_{\text{cool}}} \right) \tag{6.3}$$

where K_0 is the modified Bessel function of the second kind, $r = \sqrt{x^2 + y^2}$, the cooling length $l_{\text{cool}} = \sqrt{\kappa / g}$ and the maximum temperature rise $T_0 = P_{\text{total}}/(2\pi\kappa)$.

If we also include l_{tip} to approximate the effect of the finite tip size we end up with a heat spot of the following form:

$$T_{\text{spot}}(x' - x, y' - y) = T_0 K_0 \left(\sqrt{\frac{(x' - x)^2 + (y' - y)^2 + l_{\text{tip}}^2}{l_{\text{cool}}^2}} \right) \tag{6.4}$$

A typical temperature profile as calculated by eq. 6.4 with a finite tip size approximation $l_{\text{tip}} = 25$ nm, the actual radius of the tip, and a cooling length of $l_{\text{cool}} = 200$ nm is shown in Fig. 6.3. In the following a 25 nm finite tip size correction, in accordance with the physical tip size, was used for simulations unless otherwise stated.

6.1.2. Model of a pnp-junction

In Fig. 6.4 we show how the photocurrent pattern from a pnp-junction looks like where the p and n regions are extended to a size larger than the heat spot size. The photocurrent pattern is simulated using eq. (5.1). In this case the photocurrent at the pn- and np-junction respectively has one sign. In the simulation shown the electrical contacts are on the left and right outside of the shown region. While the the change between p- and n-type region which is responsible for a net photocurrent is abrupt (Fig. 6.4a) the photocurrent extends over a certain region (Fig. 6.4b) which in this case is mainly due to l_{cool}, as here $l_{\mathrm{cool}} \gg l_{\mathrm{tip}}$.

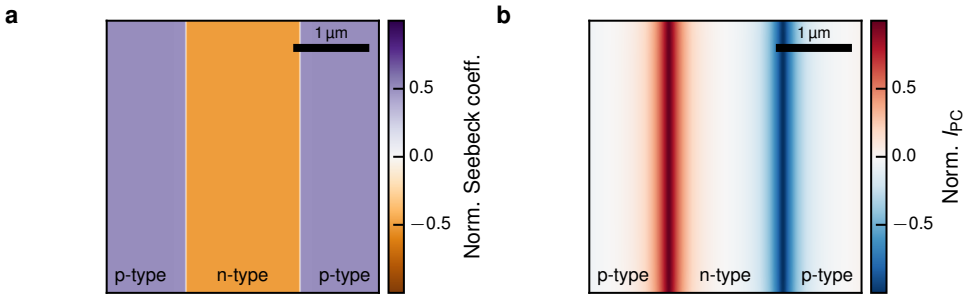

Fig. 6.4.: Simulation of near-field photocurrent from a pnp-junction. **a** Spatial Seebeck coefficient profile for two p- and one n-type region. Their doping is assumed to be of the same magnitude of opposite sign leading to opposite sign Seebeck coefficients with the same magnitude (see Fig. 5.1). **b** Photocurrent generated by the pn- and np-junction with a cooling length of 200 nm and a tip size of 25 nm.

For calculating I_{PC} at each position one has to do a convolution of the spatial Seebeck coefficient profile with the temperature gradient. This is numerically very expensive and the simulations can take a long time. In order to more efficiently simulate a photocurrent map for an arbitrary spatial Seebeck profile we use the convolution theorem which allows us to just multiply the Fourier transform of spatial Seebeck coefficient and temperature gradient, multiply them and inverse Fourier transform them. This is computationally much faster and the simulation time is greatly reduced. This method was employed for all simulations shown unless stated otherwise.

6.2. Near-field photocurrent nanoscopy setup

The setup used is based on a Neaspec neaSNOM microscope with an additional current amplifier (Femto DHPCA-100). For the current amplifier it is important that its cutoff frequency is well above 500 kHz. This is because a typical tapping frequency used for the s-SNOM operation is $\sim$ 250 kHz and in order to suppress background signal we typically work at the second or third harmonic, thus well above 500 kHz. It is equipped with a CO_2 laser operated at 10.6 µm wavelength, away from the phonon resonance of SiO_2.[164] Furthermore it also has a tunable monochromatic quantum cascade laser (QCL) source which allows us to measure inside the reststrahlen bands of h-BN. The probes were commercially-available metallized atomic force microscopy probes with an apex radius of $\sim$ 25 nm. The tip height was modulated at a frequency of $\sim$ 250 kHz with an amplitude of 60–80 nm. The

near-field photocurrent I_{PC} was obtained from the second harmonic demodulation of the photocurrent signal in order to suppress the background photocurrent signal due to the illumination of the complete device. [117]

7. Photocurrent nanoscopy of different graphene devices

In this chapter we will employ the previously introduced near-field photocurrent nanoscopy to characterize the opto-electronic properties of a variety of graphene devices in the mid-infrared.

Opto-electronic devices utilizing graphene have already demonstrated unique capabilities, which are difficult to realize with conventional technologies.[158] However, the requirements in terms of material quality and uniformity are very demanding. A major roadblock towards high-performance devices are the nanoscale variations of graphene properties, which strongly impact the macroscopic device behaviour.[59] Here, we present and apply opto-electronic nanoscopy to measure locally both the optical and electronic properties of graphene devices. This is achieved by combining scanning near-field infrared nanoscopy with electrical device read-out, allowing infrared photocurrent mapping at length scales of tens of nanometers.[191–194] We apply this technique to study the impact of edges and grain boundaries on spatial carrier density profiles and local thermoelectric properties. Moreover, we show that the technique can also be applied to encapsulated graphene/h-BN devices, where we observe strong charge build-up near the edges, and also address a device solution to this problem. The technique enables nanoscale characterization for a broad range of common graphene devices without the need of special device architectures or invasive graphene treatment.

As large scale integration and wafer scale device processing capabilities of graphene have become available,[196–203] technological implementations of electronic and opto-electronic graphene devices are within reach.[63,158,204] At the same time, to achieve high device performance, any imperfections at the nanometer or even atomic scale need to be minimized or even eliminated. For example, in large area graphene, grown by chemical vapour deposition (CVD), grain boundaries are the stitching regions between different monocrystalline parts of graphene and act as carrier scatterers, limiting the graphene mobility and uniformity.[184,205] These nanoscale defects are elusive to many standard characterization techniques without special treatment of the graphene.[206,207] In addition, even perfectly monocrystalline graphene is still highly sensitive to its environment, and on typical substrates charge-density inhomogeneities (charge puddles)[58,59,65,208–210] and additional doping near contacts, defects and edges arise, which reduce the device performance as well. Therefore it is important to efficiently probe the nanoscale opto-electronic properties of graphene and to understand the microscopic physical behaviour.

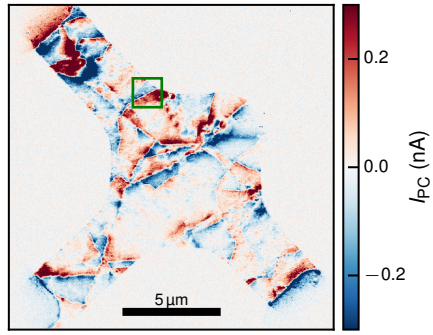

Fig. 7.1.: Near-field photocurrent from grain boundaries. I_{PC} map at a backgate voltage $V_{BG} = 0\,V$ of a CVD graphene device with three contacts: top left (drain), right (source) and bottom left (ground). Both grain boundaries and wrinkles show characteristic photocurrent patterns. The green box indicates the measurement region in Fig. 7.2a,b. A Raman map of the same device is shown in Fig. 7.6.

In this chapter we demonstrate how the previously described fully non-invasive room-temperature scanning near-field photocurrent nanoscopy[191–194] is used with infrared frequencies. We use it to study the nanoscale opto-electronic properties of devices that can later be used for real applications. This technique allows measuring the properties of graphene devices that affect their performance with high spatial resolution in atmospheric conditions. We apply this technique to study the microscopic physics of grain boundaries (see sec. 7.1) and charge density inhomogeneities, the so-called charge puddles (see sec. 7.2). In addition, we study encapsulated graphene devices,[35,211] where the encapsulation would prevent many other scanning probe techniques from accessing local properties of graphene.

7.1. Grain boundaries

We first discuss the application of this infrared near-field photocurrent technique to grain boundaries, which are responsible for some of the line-shaped features in the photocurrent

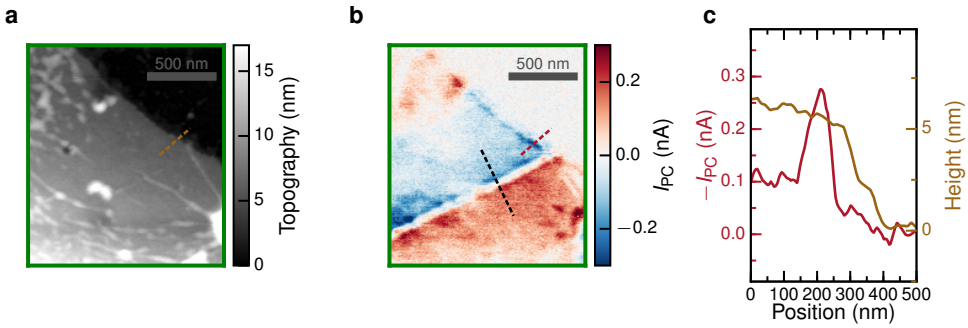

Fig. 7.2.: Near-field photocurrent working principle and photocurrent from grain boundaries. **a** Topography of etched CVD graphene does not show grain boundary but only wrinkles and other inhomogeneities due to the transfer process. **b** I_{PC} at $V_{BG} = 0\,V$ clearly shows a grain boundary and the expected sign change around it. The black dashed line indicates the measurement positions in Fig. 7.3a,d. **c** Topography (brown) and I_{PC} (red) measured at the brown line in **a** and the red line in **b** respectively.

map in Fig. 7.1b. The region within the green frame is shown with higher resolution in Fig. 7.2b, exhibiting a strong photocurrent signal that changes sign along a sharp boundary, yet the graphene is topographically flat in the vicinity of this boundary (Fig. 7.2a). We show now that this type of feature indicates a grain boundary.

The CVD graphene was transferred onto a self-assembled monolayer[212] on 285 nm of SiO_2 in order to stabilize the charge neutrality point. The contacts were defined using optical lithography with Ti(5 nm)/Pd(35 nm). The graphene was transferred onto deposited contacts. The device was fabricate by Gabriele Navickaite and Davide Janner at ICFO.

Figure 7.3a shows a line profile of I_{PC} across the boundary feature identified in Fig. 7.2b. This antisymmetric I_{PC} can be explained by a localized deviation in S at the boundary, i.e. a line defect within an otherwise uniform thermoelectric medium. Indeed, grain boundaries behave as localized lines of strongly modified electronic properties, within otherwise uniform graphene.[96,183,185,213,214] We remark that the decay of the photocurrent away from the boundary extends over more than 100 nm, which is due to a larger hot carrier cooling. We find in this case $l_{cool} = 140$ nm.

To gain more insight in the Seebeck coefficient at the grain boundary, we tune the carrier density by a global gate (Fig. 7.3d). We observe that the antisymmetric spatial photocurrent profile changes sign as the backgate voltage V_{BG} passes the peak in resistance, i.e., the global charge neutrality point V_D. The Seebeck coefficient S_G of graphene itself changes sign at the charge neutrality point[162,166,170,215] (Fig. 7.3c), thus our data implies that the Seebeck coefficient of the grain boundary S_{GB} is always smaller in magnitude than S_G, since $I_{PC}(V_{BG}) \propto S_G(V_{BG}) - S_{GB}(V_{BG})$.

Using a polycrystalline graphene model (developed by Jose E. Barrios-Vargas and Aron W. Cummings in the group of Stephan Roche at ICN2), we compute the resistance due to grain boundaries using a Kubo transport formalism and real space simulations.[206] S_{GB} is the ratio of the first- and zero-order Onsager coefficients. Indeed we find that S_{GB} is always smaller in magnitude and has a similar lineshape as S_G in the carrier density range measured (Fig. 7.3c). Fig. 7.3e shows a simulation of the photocurrent for the calculated Seebeck coefficients, which is in excellent agreement with the measurements.

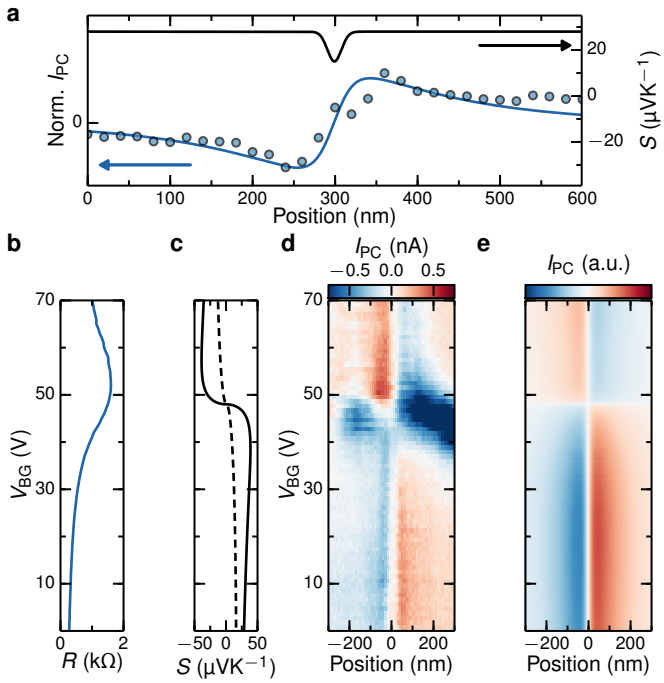

Fig. 7.3.: Photocurrent profile at a grain boundary and its gate voltage dependence. **a** Photocurrent profile, measured at the black dashed line in Fig. 7.2b, perpendicular to the grain boundary at $V_{BG} = 0$ V shows good agreement with the photo-thermoelectric model with $l_{cool} = 140$ nm. The modelled spatial Seebeck profile (with FWHM 20 nm) is shown in black. **b** Two-probe device resistance as a function of V_{BG}. **c** Simulated Seebeck coefficient S_G for pristine graphene (solid line) and S_{GB} for polycrystalline graphene with an average grain size of 25 nm (dashed line). **d** Backgate dependent photocurrent profile perpendicular to the grain boundary shows that the grain boundary changes its sign at the charge neutrality point. **e** Simulated backgate dependent photocurrent profile based on the Seebeck profiles in **c**.

7.1.1. Topography, Optical Signal, Photocurrent

Mid-infrared s-SNOM also offers the ability to detect grain boundaries in the optical signal, obtained from the light scattered out from the tip into far field.[96] We also compare the visibility of the grain boundary in optical signal to the simultaneously-measured photocurrent (Figs. 7.4). In Fig. 7.4a and c, we show the topography and the near-field photocurrent at a grain boundary at a backgate voltage of 0 V. To give further proof that what we observe is indeed a grain boundary we also show the simultaneously acquired optical signal in Fig.7.4b. The optical signal shows the typical double fringes due to plasmon reflections at the grain boundary.[96,99]

When comparing the topography in Fig. 7.4a with the optical signal in Fig. 7.4b and the near-field photocurrent in Fig. 7.4c it becomes evident that the optical signal and the photocurrent contain information not visible in the topography.

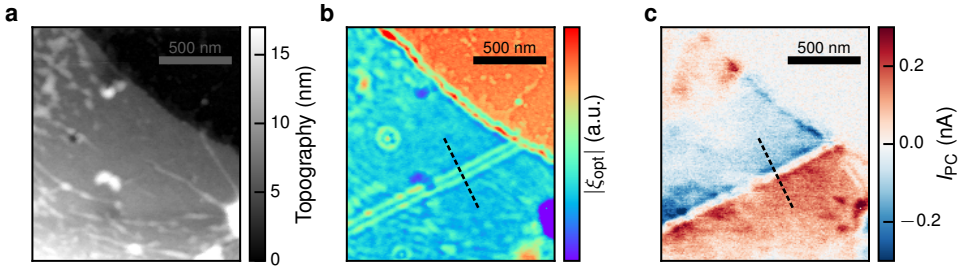

Fig. 7.4.: Comparison between topography, optical signal and photocurrent. **a** Topography of etched CVD graphene does not show grain boundary but only wrinkles and other inhomogeneities due to the transfer process. **b** Optical signal shows the characteristic plasmonic double fringes around a grain boundary in CVD graphene because the intrinsic doping of the graphene is strong and plasmons are supported.[96,99] **c** Near-field photocurrent clearly shows grain boundary and a sign change around it.

7.1.2. Gate dependence of a grain boundary

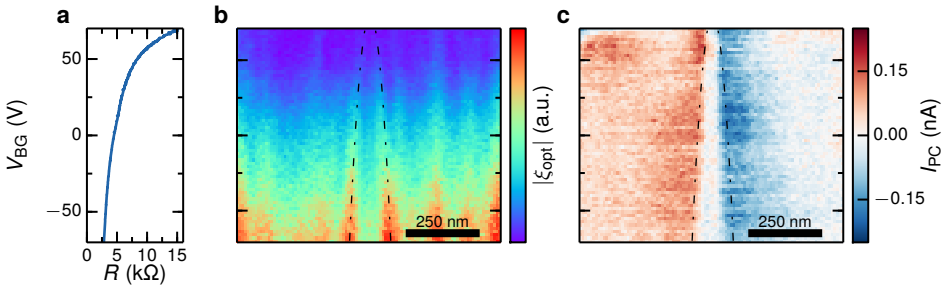

Fig. 7.5.: Gate dependent measurement of a grain boundary. **a** Backgate dependence of the resistance of the device measured simultaneously to the near-field optical scattering and near-field photocurrent. **b** Near-field optical scattering shows the plasmon reflections due to the grain boundary and their dependence on the carrier density of the graphene. **c** Near-field photocurrent shows no sign change even for highly doped graphene. The dashed dotted curves in **b** and **c** show the theoretical fringe spacing for a phase shift due to the reflection of $-3/4\pi$.[96]

As shown before the Seebeck coefficient at or very near the grain boundary is smaller in magnitude than the Seebeck coefficient of the surrounding pristine graphene for all the carrier densities measured. To further support this statement, we show the near-field optical scattering and near-field photocurrent for an extended carrier density range in Fig. 7.5. These data show that there is no additional sign change for higher carrier densities indicating that the Seebeck coefficient at the grain boundary S_{GB} is smaller in magnitude than the Seebeck coefficient of pristine graphene S_G for the measurable range of carrier densities. We note that in the case of Fig. 7.5c there is no sign change as a function of gate voltage visible as the charge neutrality point of the device was not reached due to high intrinsic doping. Grain boundaries are thus modelled as having a finite width with a Gaussian profile[96] and their Seebeck coefficient is close to zero, in accordance with

the results discussed before.

When comparing the position of the photocurrent extrema in Fig. 7.5c with the expected plasmonic fringe spacing as indicated by the dashed dotted curve it becomes evident indeed also the position of the photocurrent extrema is changing with carrier density. This could be due to an increased absorption due to the excitation of plasmons in the graphene and is subject of further study.

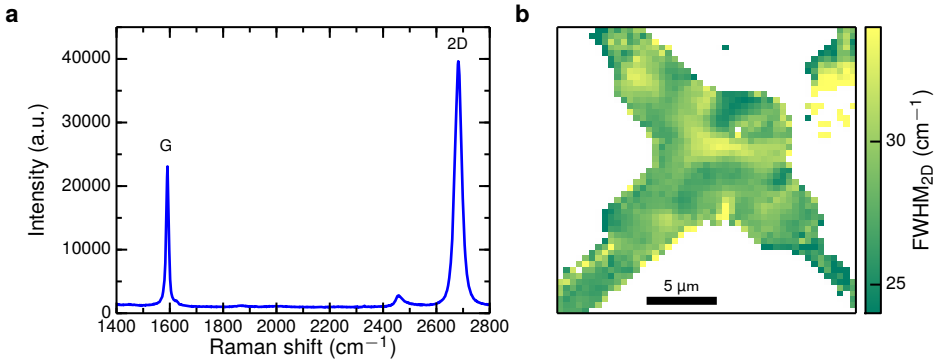

Fig. 7.6.: Raman spectrum and map of the CVD device. **a** Raman spectrum of the graphene shows the characteristic G and 2D peak of single layer graphene. **b** Map of the full width at half maximum of the 2D peak at the different positions of the device shown in Fig. 7.1. This map clearly shows that the device is fully composed of single layer graphene. In the white region no graphene is present.

In Fig. 7.6 show a map of the full width at half maximum of the 2D peak of the graphene Raman spectrum to confirm that the graphene is single layer everywhere on the device. [190] It is clearly visible that besides large scale inhomogeneities no fine features, as visible in the near-field photocurrent, due to grain boundaries are observed in the Raman map.

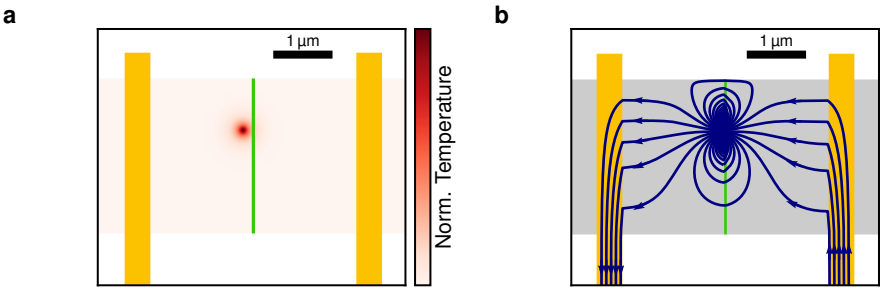

Fig. 7.7.: Heat spot creating near-field photocurrent flow pattern from grain boundary. **a** A heat spot created in the graphene due to the near-field energy being converted into heat in the graphene. **b** A heat spot creates a photocurrent flow pattern in the graphene (grey) which flows through the contacts (gold). Contacts are shown in gold, graphene in grey and substrate in white.

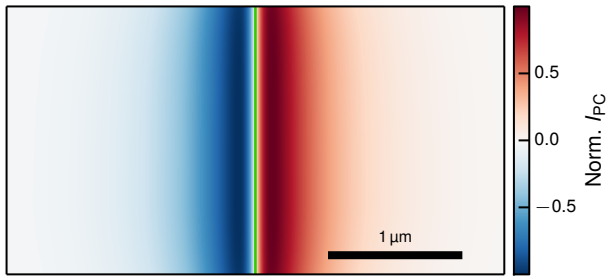

Fig. 7.8.: Simulated photocurrent map from a grain boundary. A map of the simulated photocurrent for each position of the graphene device. The contacts are on the left and right outside of the region shown in this figure. The cooling length used was 140 nm and the tip size 25 nm. The position of the grain boundary is indicated by a green line.

7.2. Charge puddles

We next examine near-field photocurrent in a typical two probe exfoliated graphene device (Fig. 7.9). The device was fabricated by Qiong Ma in the group of Pablo Jarillo-Herrero at MIT. The exfoliated graphene device was fabricated on a Si/SiO_2(300 nm) wafer, used as backgate. The Cr(0.8 nm)/Au(80 nm) contacts were defined using electron beam lithography. A strong photocurrent is obtained with the tip near the metal contacts, similar to previous near- and far-field measurements.[54,191,216] Additionally, an apparently random pattern of photocurrent is present throughout the device, as in high-resolution far-field measurements[216] but at a much finer scale.

The random photocurrent pattern between the contacts in Fig. 7.9a indicates random variations in Seebeck coefficient over short length scales. Random variations of the Seebeck coefficient are indeed expected since it depends on carrier density,[170] which in turn has fine-scaled inhomogeneities (charge puddles).[58,59,65,208,209] The photocurrent variations can thus be used to gain insight in the charge puddle distribution. A more detailed view of the photocurrent due to charge puddles in Fig. 7.9b shows that the length scale that can be resolved is on the order of hundreds of nanometers.

Quantitatively, from the autocorrelation of the photocurrent in comparison to a photothermoelectric model taking into account the size of the charge puddles in Fig. 7.9c we extract $l_{cool} \sim 200\,nm$. The charge puddles are modelled to have a size of $\sim$ 20 nm, in accordance with measurements of graphene on SiO_2.[58,65,208,209]

By changing the gate voltage we study the carrier density profile with high spatial resolution (see Fig. 7.10) and highlight the possibility of spatially resolving the charge neutrality point for a large device. I_{PC} from charge puddles is largest around the charge neutrality point and varies with position. This is consistent with the very high sensitivity of the Seebeck coefficient to changes in carrier density, near zero density (Fig. 7.10b). This allows us to map the local carrier density offset (charge inhomogeneity) throughout the device, as indicated by the extremum of photocurrent in a scan of photocurrent vs. gate voltage (Fig. 7.10c). In contrast to the grain boundary photocurrent we do not observe the charge puddle photocurrent change sign when sweeping the average carrier density through the charge neutrality point, as expected from the gate dependence the of Seebeck coefficient.

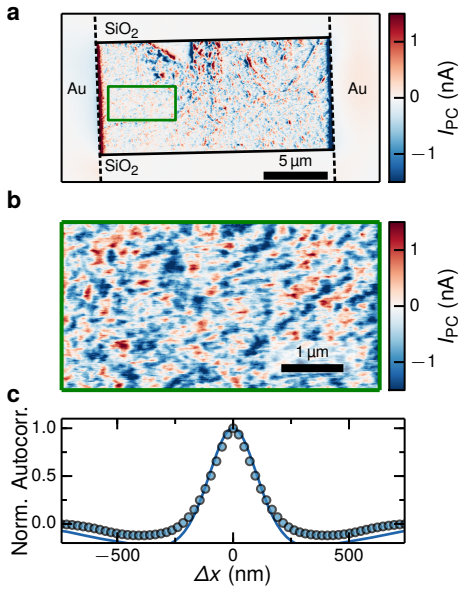

Fig. 7.9.: Photocurrent from charge puddles. **a** Near-field photocurrent map of an exfoliated graphene device on 300 nm SiO_2 at $V_{BG} = 20\,V$. The dashed lines indicate the position of the contacts and solid lines the graphene edges. The green box indicates the measurement region in **b**. **b** Detailed photocurrent map at the charge neutrality point of the device ($V_{BG} = 7$ V) reveals the charge puddles and the high spatial resolution of the technique. **c** Autocorrelation of the photocurrent from charge puddles at V_D (data points) compared to photocurrent expected from a random charge puddle distribution and $l_{cool} = 200\,nm$ (blue curve). Autocorrelation is taken along the source drain current path.

We can thus resolve the local charge neutrality point at a given position of the device (green curve, Fig. 7.10a), which can be different from the global charge neutrality point V_D, the backgate voltage V_{BG} at which the resistance is maximum (blue curve, Fig. 7.10a). We show that the global charge neutrality point (blue curve, Fig. 7.10a) is determined by an average of the gate voltages at which the local charge neutrality points appear (red curve, Fig. 7.10a). Spatially resolved puddle photocurrent can be much narrower (green curve, Fig. 7.10a) than the average of all possible current paths (red curve, Fig. 7.10a) This indicates that the graphene locally has less inhomogeneity. Thus the technique gives insight not only in the global but also in the local behaviour of the device.

7.2.1. Charge puddle model

In order to model photocurrent from charge puddles first we need to find an accurate model of the charge puddle distribution. For this we use a random spatial Seebeck profile generated by a spatial profile of white noise and smoothing the noise to create charge puddles with an average approximate size of 20 nm. This size is the size previous experimental studies of charge puddles on SiO_2 with a higher spatial resolution have found.[58,65,208,209]

In order to efficiently calculate the photocurrent map from the charge puddles we again convolve the spatial Seebeck profile with the spatial heat gradient profile. A comparison between the spatial Seebeck profile and the photocurrent map is shown in Fig. 7.11. Here

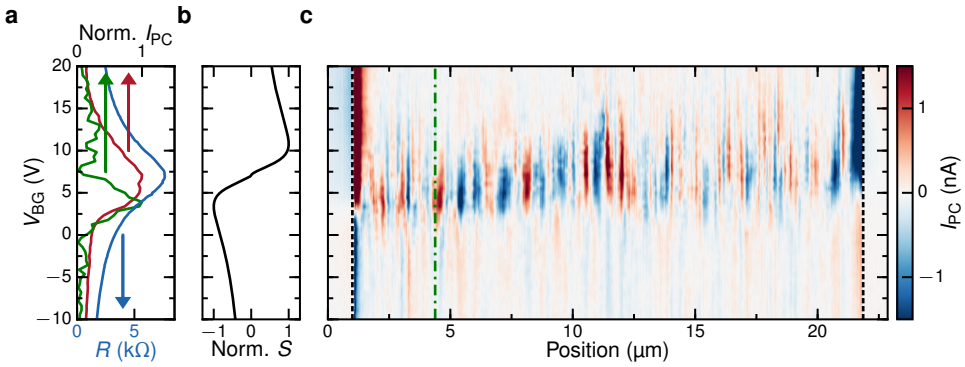

Fig. 7.10.: Dependence of photocurrent profiles on backgate voltage reveals doping inhomogeneities. **a** Backgate dependence of the resistance of the device measured simultaneously to the photocurrent in blue. The red curve shows the normalized root mean square of the photocurrent across the device. The green curve shows a single normalized photocurrent backgate trace, corresponding to the green dashed dotted line in **c**. **b** Backgate dependent Seebeck coefficient of graphene, calculated from the gate dependent resistance in **a** using the Mott formula.[170] **c** Backgate dependence of the photocurrent across the device. Graphene is between the black dashed lines, which indicate the edges of the metal contacts.

the source and drain contacts are outside of the displayed on the left and right respectively. It is obvious that for positions with a high gradient in Seebeck coefficient the photocurrent is strongest, like expected from eq. (5.1).

7.3. Encapsulated graphene and edge doping

Finally we apply this technique to a graphene device encapsulated between two layers of h-BN, using the polymer-free van der Waals assembly technique[35,211] as sketched in Fig. 7.13a. This device lies on top of an oxidized silicon wafer, used as a backgate. The stack is etched into a triangle and electrically side-contacted by metal electrodes.[35] The device was fabricated by Yuanda Gao in the group of James Hone at Columbia University. The Si/SiO_2(300 nm)/h-BN(46 nm)/Gr/h-BN(7 nm) and the Si/SiO_2(300 nm)-/AuPd(15 nm)/h-BN(42 nm)/Gr/h-BN(13 nm) stacks, were fabricated using the polymer-free van der Waals assembling technique.[35] The stack is etched into a triangle and is electrically side-contacted with metal electrodes. Recent studies[217,218] have shown that the edges affect where current flows in the device, in particular near charge neutrality. In the following we study the build up of edge doping and provide a solution to this.

While monitoring the photocurrent of such encapsulated devices, we observe indications of strong carrier density variations near the edges over micrometer scales. These variations are influenced by lighting conditions, gate voltages, and temperature, and evolve over timescales ranging from minutes to weeks. As an example, Figure 7.12a-d shows a progression of photocurrent maps, taken after annealing the device at 200 °C for 30 minutes to temporarily remove charge density variations near the edges. Initially in Fig. 7.12a we see very small photocurrents indicating a flat carrier density landscape. After some time (∼ hours), in the dark with only gate voltages smaller than 3 V applied, a small doping

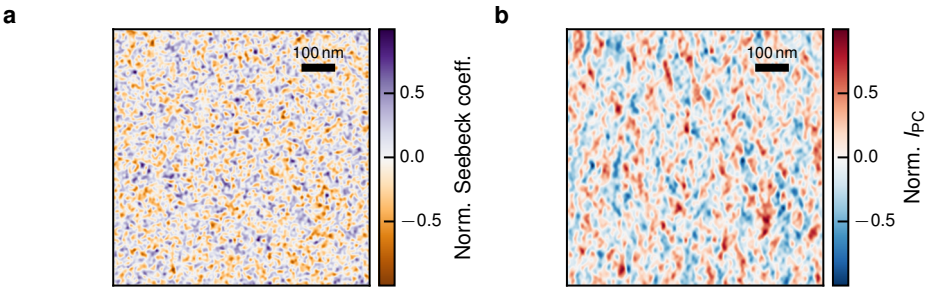

Fig. 7.11.: Simulation of near-field photocurrent from random charge puddle distribution. **a** Random distribution of Seebeck coefficients due to a random distribution of charge puddles with an average size of $\sim$ 20 nm. **b** Photocurrent generated by the charge puddles in **a** with a cooling length of the charge carriers in the graphene of 200 nm and a tip size of 25 nm.

gradient between the contacts builds up. This gradient leads to the stronger photocurrent shown in Fig. 7.12b. The local charge neutrality point, indicated by the maximum of photocurrent, is at the same position close to the edge of the device as further inside the bulk. After keeping the device for 3 hours in ambient conditions we can see a change of the local charge neutrality point at the edge of the graphene compared to the bulk in Fig. 7.12c. The edge is slightly more *p*-type compared to the bulk. Finally we apply high gate voltages, of in this case 50 V for $\sim$ 20 hours, to increase the edge doping. A strong *p*-doping at the edge and an *n*-doping in the bulk of the graphene is induced in Fig. 7.12d. This indicates that electric field accelerates the speed and increases this type of edge doping.

We exploit the observed edge doping to create a natural *pn*-junction along the edge of the device. For this we apply a backgate voltage at which the edge of the graphene is *p*-type and the bulk *n*-type. We observe photocurrent at the junction in Fig. 7.13b around the whole device, indicating that the edge doping is uniform around the graphene. The photocurrent decays gradually towards the midline between the electrodes as a result of how the triangular geometry modifies the ability of the contacts to capture photocurrents.[168] We are able to temporarily reset the edge doping by annealing the device on a hotplate at 200 °C for 30 minutes.

While we have not been able to precisely identify the origin of the edge doping, we present here a technique to completely eliminate it. We place encapsulated graphene on top of a local conductive gate, such as a 15 nm AuPd alloy in the case of Fig. 7.13c. We find that edge doping is efficiently suppressed even after extended periods of time at ambient conditions and high gate voltages. Furthermore, such devices lack the photodoping effect observed for devices where the h-BN is in contact with SiO_2[126] (see section 7.3.1). We suspect that humidity that is able to penetrate between the boron nitride and the silicon oxide leading to trapped charges is responsible for the observed edge doping.

In the device with a metal gate we find small features due to charge puddles on top of a slowly varying background photocurrent, due to large scale carrier density inhomogeneities. The size of the features due to charge puddles determined by autocorrelation is $\approx$ 800 nm. The long length scale of those features is either due to the longer cooling length of the encapsulated graphene compared to the graphene on SiO_2 or due to larger charge puddle

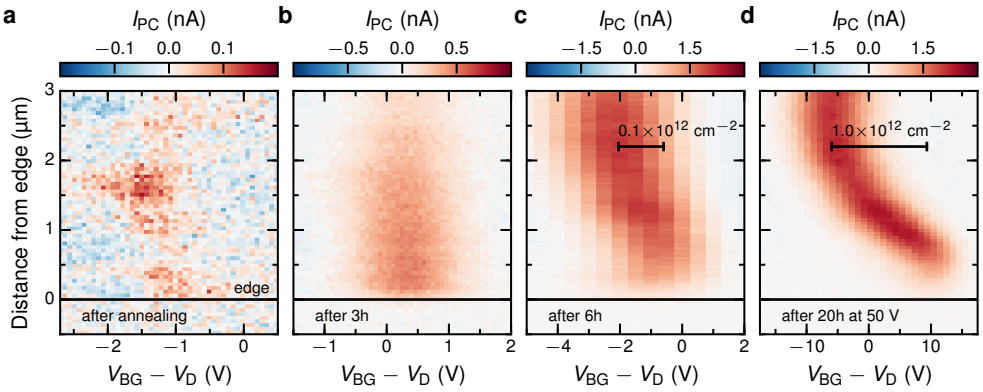

Fig. 7.12.: Near-field photocurrent maps revealing edge doping in encapsulated graphene. **a** Spatial photocurrent profile vs. backgate voltage V_{BG} (minus voltage of the resistance maximum V_D) near the edge of encapsulated graphene. These data are taken directly after annealing the device. **b** The same scan on the same device after three hours in air, and **c**, after annealing and applying V_{BG} up to 3 V. **d** The same scan after $\sim$ 20 hours in air and after applying V_{BG} up to 50 V. In **a**-**d** the black solid lines indicate the graphene edge.

size in the encapsulated devices. Further work is required to clearly distinguish these effects.

7.3.1. Photodoping and puddles of encapsulated graphene

It is known that graphene on h-BN on top of an oxidized silicon wafer shows photodoping when it is illuminated with visible light.[126] This effect is clearly visible in our near-field photocurrent measurements after illumination with visible light. In Fig. 7.14a we see almost no near-field photocurrent at a backgate voltage of −90 V. In Fig. 7.14b we show the near-field photocurrent pattern after the sample was illuminated with a white LED light source for several minutes at a backgate voltage of −90 V. Clearly, near-field photocurrent is visible all the way throughout the device. We attribute this to the screening of the backgate by photoexcited defects in the h-BN or at the h-BN/silicon dioxide interface, which can effectively neutralize the graphene.[126] Thus we see charge puddles which show a very similar near-field photocurrent pattern compared to the near-field photocurrent from charge puddles observed at the charge neutrality point of exfoliated graphene on SiO_2. In the case of the encapsulated device the charge puddles are induced by the photoexcited charged defects in the h-BN. In order to reset the photo doping and be immune to it we use positive gate voltages.[126]

7.3.2. Encapsulated graphene with a local gate

We also studied near-field photocurrent from an encapsulated device which was put onto conductive PdAu alloy gates with a 50 nm gap in between them in order to individually tune the carrier density in the graphene above the two gates. In Fig. 7.15a we show a six-fold pattern typical for a photothermoelectric effect[162] in graphene measured at the junction between the two gates, which is indicated by the dashed line in Fig. 7.15.

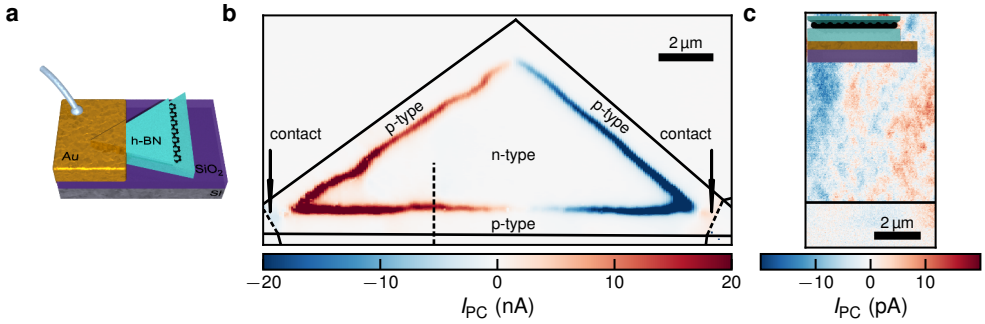

Fig. 7.13.: Near-field photocurrent maps revealing edge doping in encapsulated graphene. **a** Sketch of the device, a stack of h-BN(46 nm)/Gr/h-BN(7 nm) on a Si/SiO_2(300 nm) wafer used as global backgate. **b** Photocurrent close to the resistance maximum at $V_{BG} = -28$ V shows a triangular photocurrent pattern, due to edge *p*-doping. The dashed lines in **f** indicate where the stack is underneath the gold. **c** Photocurrent from charge puddles in encapsulated graphene on a metal gate close to the charge neutrality point (sketch in inset). The layers are AuPd(15 nm)/h-BN(42 nm)/Gr/h-BN(13 nm). The electrical contacts are on the left and right outside of this figure. In **b**,**c** the black solid lines indicate the graphene edge.

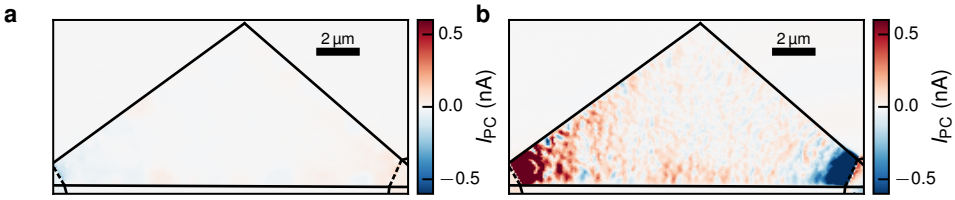

Fig. 7.14.: Encapsulated graphene device on oxidized silicon wafer. **a** Near-field photocurrent of the graphene triangle device at -90 V backgate voltage in the dark. **b** Photodoping showing up in the near-field photocurrent after illuminating the device for several minutes with white LED light at -90 V. The dashed lines in **a** and **b** indicate where the stack is underneath the gold and the solid lines the outer edge of the stack and gold respectively.

In Fig. 7.15b the current in the device is shown for both sides being tuned to a gate voltage of 0.4 V, close to the charge neutrality point. The magnitude of the near-field photocurrent is two orders of magnitude smaller than the magnitude of near-field photocurrent from charge puddles in graphene on SiO_2. This indicates that the charge density inhomogeneity of the charge puddles in encapsulated graphene on a local gate is much lower than for graphene on SiO_2. Furthermore the length scale of the charge puddles indicates that the charge puddle size is much larger than for the case of graphene on SiO_2 [65,209] or that the cooling length in encapsulated graphene devices is much longer than for bare graphene, as expected due to the increased carrier mobility in encapsulated graphene.

We remark the we do not see any photodoping for the encapsulated graphene on top of a conductive gate structure, even after extended periods of exposure of many minutes to the same white light LED as was used to induce photodoping in Fig. 7.14b. This can be explained by the extraction of the photoexcited charged defects by the conductive gate,

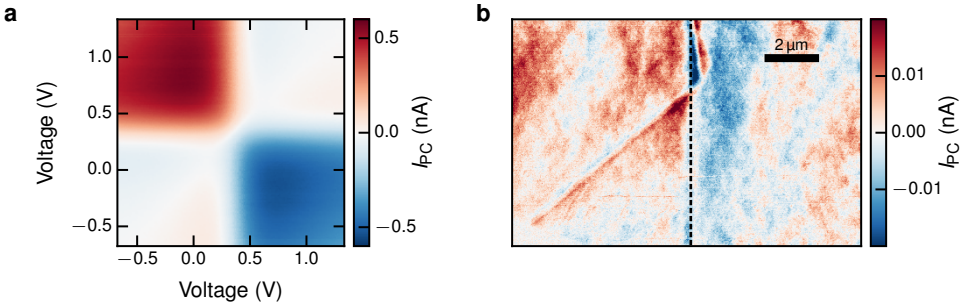

Fig. 7.15.: Encapsulated graphene with independently tunable gates. a Measured six-fold pattern showing the thermoelectric origin of the near-field photocurrent at the junction between the two gates.[162] **b** Near-field photocurrent from a local gated encapsulated graphene device with both sides of the local gate being tuned to a voltage of $V_{BG} = 0.4$ V close to the charge neutrality point. The layers are AuPd(15 nm)/h-BN(42 nm)/Gr/h-BN(13 nm). The dashed line indicates the position of the 50 nm gap between the two local gates.

which is in direct contact with h-BN.

7.4. Conclusion

To conclude, in this chapter we demonstrated that scanning near-field photocurrent nanoscopy is a versatile technique to characterize the electronic and opto-electronic and even previously inaccessible properties of relevant graphene devices. This technique is highly promising for spatially resolved quality control of regular graphene devices without the need for special device structures and can therefore be readily applied. The technique can be exploited to measure the charge puddle distribution in graphene encapsulated in h-BN, which cannot be measured with current techniques that need electrical contact with the graphene.[58,59,65,208,209] This technique can also be used for nanometer resolution device characterization in terahertz regime, which is interesting both from a fundamental[219] and applied point of view.[114] Indeed it was shown that even in the terahertz the photocurrent resolution is on the order of tens of nanometers.[116] Furthermore the high resolution enables studying the role of substrate phonons on the photocurrent generation in graphene in more detail.[164,180] In the following chapters we will also use this technique to study how plasmons in graphene (chapter 8) and hyperbolic phonon polaritons in h-BN (chapter 9) can be detected fully electrically.

8. Broadband electrical detection of graphene plasmons

In this chapter we will show how near-field photocurrent nanoscopy can be used to electrically detect propagating graphene plasmons. We show that the detection is broadband and employ it to detect plasmons in both the mid-infrared as well as terahertz region of the electromagnetic spectrum. In the terahertz case the plasmons hybridize with the underlying metal gate and an acoustic plasmons with a linear dispersion is created. We employ two local gates to fully tune the thermoelectric and plasmonic behaviour of the graphene. High-resolution real-space photocurrent maps are used to investigate the plasmon propagation and interference, decay, thermal diffusion, and thermoelectric generation.

Controlling, detecting and generating propagating plasmons by all-electrical means is at the heart of on-chip nano-optical processing.[20,220,221] Graphene carries long-lived plasmons that are extremely confined and controllable by electrostatic fields,[8,11,24,25] however electrical detection of propagating plasmons in graphene has not been realized before. Here, we present an all-graphene mid-infrared plasmon detector, where a single graphene sheet serves simultaneously as the plasmonic medium and detector. Rather than achieving detection via added optoelectronic materials, as is typically done in other plasmonic systems,[222–229] our device converts the natural decay product of the plasmon—electronic heat—directly into a voltage through the thermoelectric effect.[230,231]

Graphene plasmonics is an emerging platform for terahertz to infrared nano-optics, attractive due to the long intrinsic lifetime of $> 0.5\,\mathrm{ps}$ and the strong tunable broadband response of its Dirac electrons.[8,111] Typically, graphene plasmons are sensed in s-SNOM by out-coupling to light, which is inefficient due to one of the key features of graphene plasmons: their extremely short wavelength ($\sim \frac{1}{100}$ that of free space light). While plasmon resonances have been exploited to enhance absorption and thereby enhance far-field photodetection,[87,232] the concept of an on-chip plasmon receiver has not been realized before.

The presented experiments are built around the state-of-the-art plasmonic medium of graphene encapsulated in h-BN, which we have demonstrated before to support high quality propagating plasmons in the mid-infrared (see chapter 3). As a key innovation in this work, the induction of free carriers in the graphene is achieved through the use of separate local gates directly underneath the h-BN, rather than the conventional global back gating through an additional SiO_2 layer. These local gates allow us to spatially modulate the charge carrier density and polarity across the device, as well as providing lower voltage operation and reduced charge trapping effects.[195] As we will show below, the junction induced by the two gates can be used as a thermoelectric detector for the plasmons for a large range of excitation frequencies.

8.1. Basics of electrical graphene plasmon detection

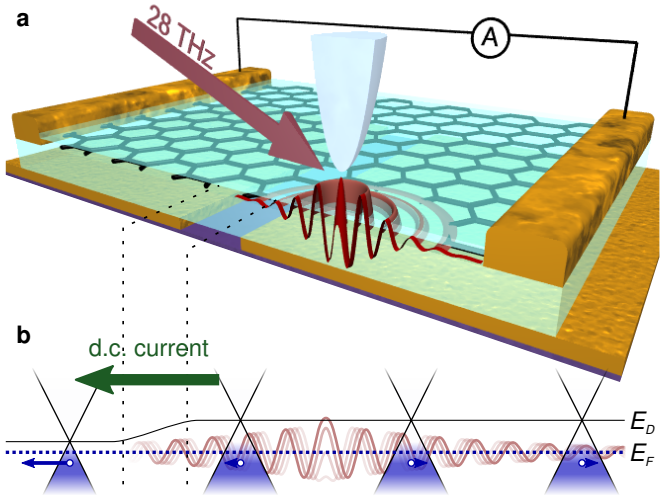

Fig. 8.1.: Measurement concept. a Schematic cross-section of devices and measurement technique. Continuous-wave laser light scatters at a movable metallized AFM tip, launching plasmons in the h-BN–graphene–h-BN heterostructure. **b**, Schematic of thermoelectric detection mechanism in a microscopic picture. The plasmon decay energy drives an outward majority carrier diffusion, in this case hole carriers. A gate-induced homojunction (seen as variation in the graphene Dirac point energy level E_D relative to the Fermi level E_F) imbalances this diffusion, resulting in a nonzero net dc current.

Figures 8.1a,b show a schematic of the operating principle of the detector. As cur-

rently no on-chip graphene plasmon sources are available, we generate plasmons using the conventional scattering scanning near field microscopy (s-SNOM) technique.[29,30] The s-SNOM apparatus consists of a scanning metal probe under illumination from a continuous wave laser. In conventional plasmonic s-SNOM experiments discussed before the out-scattered light signal is measured and contains all the information about local dielectric properties and plasmonic modes. In this chapter however we instead measure the near field photocurrent I_{PC} in the same manner as explained in chapter 6. As the graphene shows a linear photocurrent response, I_{PC} can be understood as the photocurrent arising only from the near fields of the tip, isolated from the background photocurrent directly induced by the incident light. The s-SNOM used was a NeaSNOM from Neaspec GmbH, equipped with different laser sources for the mid-infrared and terahertz radiation.

The plasmon launching works analogous to conventional s-SNOM described in sec. 2.2.1. The near fields at the tip apex launch radially propagating graphene plasmons, which interfere with their own reflections from the graphene edge, producing oscillations of the electric field intensity – and thus the local energy dissipation – when the tip is scanned perpendicular to the graphene edge. The dissipated energy heats the electron temperature of the graphene and after diffusion the pn-junction, yielding a photo-thermally induced current that oscillates with a period of half the plasmon wavelength $\lambda_{pl}/2$. A more detailed model including the cooling length based on experimental evidence is given in ref. 233.

8.2. Electrical detection of mid-infrared plasmons

The main part of the measurements and analysis in the following section was done by Mark B. Lundeberg at ICFO and I was closely involved starting from the design phase of the experiment. In this section of the chapter I will give an overview of the results of converting mid-infrared plasmons into photocurrent in the near-field. I will first introduce the device and the measurement results, then give a brief overview of the modelling and finally introduce the measured carrier density dependence. For more technical details and sophisticated modelling of the mechanism please refer to ref. 233. The measurements presented here are measured using a CO_2 laser at a laser frequency of 28 THz (10.6 µm free space wavelength) in order to avoid complications from the h-BN phonons.[100]

8.2.1. Device

The device was fabricated by Yuanda Gao in the group of James Hone at Columbia University according to our input. For the mid-infrared electrical plasmon detection the device fabrication started with an 10 nm, surface low roughness AuPd alloy gate film patterned by electron beam lithography, on top of an oxidized Si substrate. The gap separating the gates from each other was 150 nm, as indicated in the figures. An h-BN–graphene–h-BN stack was then prepared by the van der Waals assembly technique,[35] and placed on top of the AuPd gate layer. The bottom h-BN film (between graphene and metal) thickness of 27 nm was chosen to isolate the plasmonic mode from interacting with the gate metal, while still allowing for strong gate effect. The top h-BN film was made thin (9 nm) to allow for efficient plasmon launching and coupling of the plasmons to the s-SNOM tip.[100] The device geometry as well as the edge contacts were defined by dry etching and electron beam evaporation in the method of ref. 35. The dry etching depth

was only 11 nm, leaving most of the bottom h-BN thickness remaining in order to reduce possible leakage.

8.2.2. Results

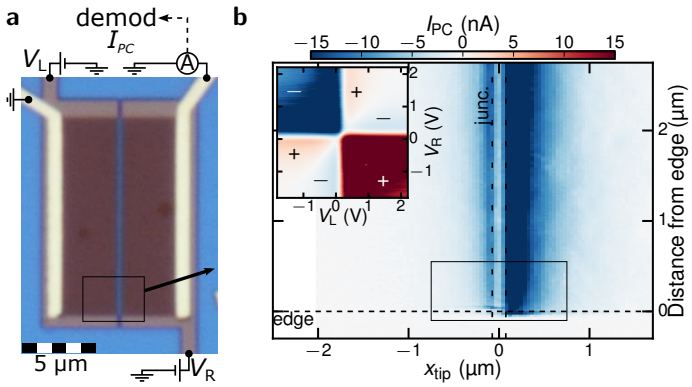

Fig. 8.2.: Device image and photocurrent measurement. **a** Optical micrograph of presented device and circuit diagram. Two metal electrodes (light yellow) contact an encapsulated graphene sheet (dark rectangle) which lies above a split metal gate layer (light brown). Split gate voltages V_L and V_R create the homojunction, while tip-induced currents are captured at the electrodes and demodulated to obtain the near field photocurrent I_{PC}. **b** Near-field photocurrent map of the entire device, showing the photosensitive junction created by applying different gate voltages. *Inset*: The sign of the photocurrent (measured with the tip over the junction) shows a six-fold pattern characteristic of thermoelectric effects.

The device and circuit schematic of the device studied in this section is shown in Fig. 8.2a. By applying different voltages $V_{L(R)}$ to the left (right) gates, we induce a localized photosensitive region around the gap of the device, e.g., a pn-junction as studied in Fig. 8.2b. The six-fold photocurrent pattern observed when both gates are scanned (figure inset) is consistent with a thermoelectric generation mechanism, where the pattern arises due to the nonmonotonic dependence of Seebeck coefficient on gate voltage.[162,166,167] For a simple junction, the thermoelectric current is $I = (S_R - S_L)\overline{\Delta T}^{junc}/R$, where $S_{L(R)}$ is the left (right) Seebeck coefficient, $\overline{\Delta T}^{junc}$ is the junction-average rise in electronic temperature relative to ambient temperature, and R is the circuit resistance. The gate dependence allows to identify the charge neutrality point of the graphene in this device (occuring at a gate voltage offset of $+0.09\,V$). From now on we use this offset and the calculated gate capacitance to convert the gate voltages $V_{L,R}$ into carrier densities $n_{L,R}$. Gate voltages are converted to carrier sheet density via $n_{L,R} = (0.73 \times 10^{16}\,m^{-2}V^{-1})(V_{L,R} - 0.09\,V)$, where the offset was determined by examining gate dependences and the coefficient was calculated as the static capacitance of the 27 nm h-BN layer with dielectric constant 3.56.[100]

Strong evidence of plasmons mediating the photocurrent is visible in photocurrent maps obtained at high carrier density (Fig. 8.3), where interference fringes can be observed in I_{PC} near the graphene edge. These fringes can be unambiguously attributed to plasmon reflections, as they match the half-wavelength periodicity seen in the s-SNOM optical signal that is conventionally used to characterize graphene plasmons.[100] The extracted

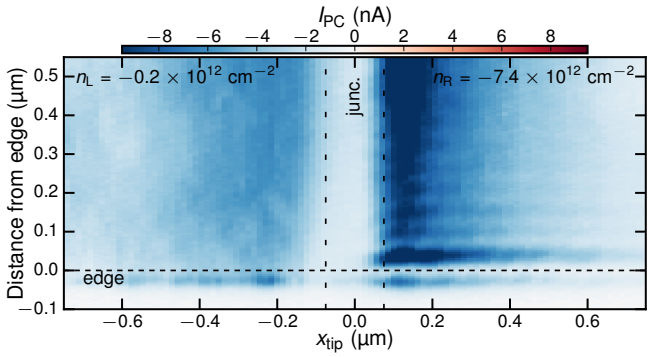

Fig. 8.3.: Plasmon photocurrent spatial maps. A high-resolution photocurrent map near the edge of the graphene, containing interference fringes at the graphene edge, analogous to the ones measured using conventional s-SNOM.[29,30] On the left side the carrier density is not high enough to support plasmons and thus no fringes are visible.

plasmon wavelength of $\lambda_{pl} = 112\,\text{nm}$ in this scan is close to the expected value of 114 nm, and consistent with a previous study of a similar h-BN–graphene–h-BN device.[100]

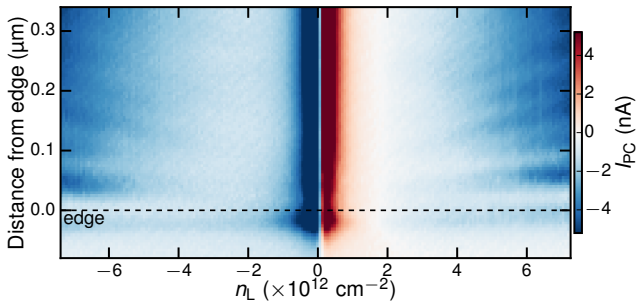

Fig. 8.4.: Gate dependence. Dependence of photocurrent on n_L, at various tip positions away from the graphene edge. This scan was taken 300 nm left of the junction with a fixed $n_R = 0.26 \times 10^{12}\,\text{cm}^{-2}$. A clear change of the fringe spacing is observed, further confirming that we are observing graphene plasmons electrically.

8.2.3. Carrier density dependence

Next, we show tunability of the nature and strength of the plasmon launching, with varying carrier density. Figure 8.4 shows the dependence of the photocurrent on the gate voltage under the tip. The data show several features simultaneously evolving with carrier density. There are two sign changes in photocurrent, due to the sign change of Seebeck coefficient differences.[162,166,167] The fringe spacing appears to follow $\frac{1}{2}\lambda_p \propto \sqrt{|n|}$ as expected for graphene plasmons.[100] Most strikingly, the photocurrent shows two regimes of strong magnitude, at high $|n|$ and low $|n|$, separated by a region of weak photocurrent from $|n| \sim 1\text{–}4\times10^{12}\,\text{cm}^{-2}$. We attribute these to the two ways that graphene can absorb power from the tip: direct heating or plasmon launching. The launched plasmon power grows strongly with carrier density primarily due to variation in plasmon wavelength: plasmons

with small values of λ_p couple poorly to the tip due to their strong confinement in the top h-BN layer and the limited range of spatial frequencies probed by the round tip. Direct heating on the other hand is strongest for low $|n|$ due to unblocked interband transitions, possible when the Dirac point E_D is within about $\hbar\omega/2$ ($= 58\,\text{meV}$) of the Fermi level E_F. A quantitative model further corroborating the given explanations is introduced in ref. 233.

8.3. Electrical detection of terahertz plasmons

The measurements and analysis in this section were done by Pablo Alonso-Gonzalez and me at CIC nanoGUNE. In this part of the chapter we will discuss electrical graphene plasmon detection when terahertz light is used to excite the plasmons. We will first show an overview of the results and then introduce the characteristic acoustic frequency dispersion for graphene close to a metal gate and finally show a carrier density dependence. For more details please refer to ref. 116. The working principle and device structure of the photodetector in this section is the same as previously discussed. In the following I will only introduce the main differences and peculiarities of terahertz graphene plasmons. The laser source used for the terahertz radiation is a gas laser (SIFIR-50 from Coherent, providing output power in the range of a few 10 mW) which is tunable from 2.5 to 5.7 THz.

8.3.1. Device

The device was again fabricated by Yuanda Gao in the group of James Hone at Columbia University according to our input. However the exact device parameters are slightly different compared with the device for mid-infrared electrical plasmon detection. In this case the h-BN(13 nm)-graphene-h-BN(42 nm) heterostructure is placed on top of a pair of 15-nm-thick AuPd gates, which are laterally separated by a gap of 50 nm. A thicker top layer of h-BN than in previous studies is permitted because of the longer plasmon wavelength of graphene plasmons in the terahertz. A smaller gap width is permissible as the voltage differences that need to be applied are smaller than in the infrared case due to the smaller carrier densities needed for terahertz plasmons. Again we are able to individually tune the carrier density of the graphene sheet on top of both of the electrons.

8.3.2. Results

As was the case with the mid-infrared laser used before near the pn-junction we observe photocurrent oscillations perpendicular to the graphene edge which decay with increasing distance from the edge (Fig. 8.5). Resembling the s-SNOM images of infrared graphene plasmons both measured using electrical detection (see previous sec. 8.2) and by s-SNOM,[29,30,100] we attribute them to terahertz graphene plasmons. While terahertz plasmons in graphene have been seen before in spectral extinction measurements[31] this is according to our knowledge the first direct observation of propagating graphene plasmons in the terahertz.

We corroborate the plasmonic origin of the photocurrent oscillations by recording line profiles along the dashed black line in Fig.8.5 at different illumination frequencies but fixed carrier densities $n_{c1} = 0.77 \times 10^{12}\,\text{cm}^{-2}$ and $n_{c2} = -1.11 \times 10^{12}\,\text{cm}^{-2}$. The near-field photocurrent profiles shown in Fig. 8.6 were extracted at a distance of about 1 µm from

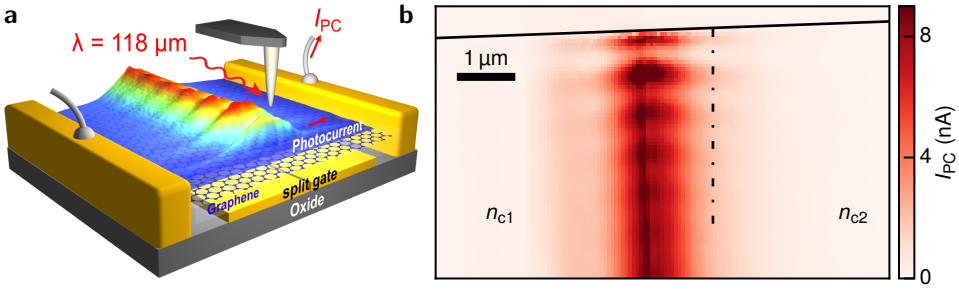

Fig. 8.5.: Terahertz photocurrent measurement of graphene plasmons at a pn-junction. a Overlay of the measured plasmons at a pn-junction with a device and measurement schematic. **b** Measurement of the experimental near-field photocurrent, I_{PC}, recorded at $f = 2.52\,\mathrm{THz}$. The carrier densities were chosen to be $n_{c1} = 0.77 \times 10^{12}\,\mathrm{cm}^{-2}$ and $n_{c2} = -0.71 \times 10^{12}\,\mathrm{cm}^{-2}$, yielding plasmons on both sides of the junction. The solid line marks the edge of the graphene sheet and the dashed dotted line marks where the line profiles in Fig. 8.6 were measured.

the 50 nm-wide gap between the two gates, in order to ensure a well-defined and homogeneous carrier density in the graphene sheet. We find that the oscillation period decreases with increasing illumination frequency f for constant carrier density (Fig. 8.6). The distance between the peaks is equivalent to $\lambda_{pl}/2$ and thus we observe a decreasing plasmon wavlength for an increasing frequency, like you would expect for graphene plasmons.

8.3.3. Indication of acoustic plasmons

By measuring the oscillation period as a function of f we obtain the frequency dispersion of terahertz graphene plasmons in this system. The measured results are shown in Fig. 8.7 (red symbols). Interestingly, we find a nearly linear dispersion at low frequencies, in excellent agreement with the dispersion calculated taking into account the full stack via the transfer-matrix method (blue contour plot in Fig. 8.7). The observed linear, or acoustic, dispersion is in different from the conventional square root dispersion for conventional graphene plasmons in free-standing graphene (black solid curve in Fig. 8.7). From the agreement between the acoustic plasmon model and the experiment we conclude that acoustic graphene plasmons rather than conventional graphene plasmons are observed. Indeed this type of acoustic dispersion is expected for graphene plasmons close to a metal gate in the terahertz due to screening.[234–237] As can be seen from the calculated dispersion for the different systems the closeness of the metal gate also increases the plasmon momentum and thus decreases the plasmon wavelength, leading to a strong wavelength compression of graphene plasmons compared to the free space light even in the terahertz regime. We show numerical simulations further investigating this wavelength reduction and field enhancement for graphene near a metal gate in ref. 116 done by Alexey Nikitin at CIC nanoGUNE.

8.3.4. Carrier density dependence and charge neutral plasmons

We also studied the plasmon interference pattern (along the dashed black line in Fig. 8.5) as a function of charge carrier density n_{c2} (Fig. 8.8). We observe that the fringe spacing

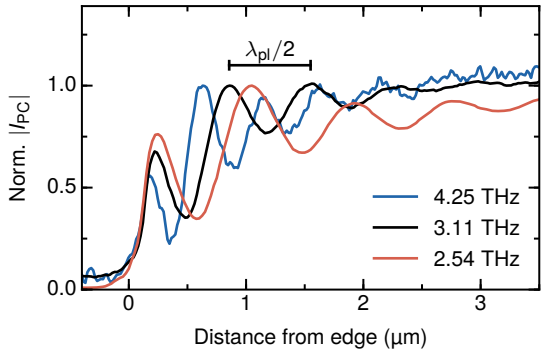

Fig. 8.6.: Line profiles at different frequencies. Near-field photocurrent profiles at different frequencies, recorded along the black dashed line in Fig. 8.5 with a carrier density of n_{c2}. The peak-to-peak distance reveals $\lambda_{pl}/2$. The carrier density was $n_{c1} = 0.77 \times 10^{12}\,\mathrm{cm}^{-2}$ and $n_{c2} = -1.11 \times 10^{12}\,\mathrm{cm}^{-2}$.

(plasmon wavelength) increases with increasing carrier concentration of both electrons and holes, demonstrating that acoustic graphene plasmons can be tuned by electrical gating, similar to systems where the graphene plasmons are not hybridized with the metal.[29,30] However, in strong contrast to graphene plasmons in the infrared, we observe graphene plasmons even at the charge neutrality point (Fig. 8.8b and 8.9). The photocurrent profile at the charge neutrality point clearly shows weak oscillations near the graphene edge, revealing plasmons with a wavelength λ_{pl} of about 650 nm. This is close to theoretically expected wavelength of 720 nm calculated using the transfer-matrix method on the full stack and the graphene local RPA conductivity at room temperature[56] ($T = 300\,\mathrm{K}$). We explain the existence of plasmons at the charge neutrality point by electron and hole populations that are thermally excited at room temperature. Their energy of about 25 meV is large enough for supporting plasmons at terahertz frequencies (3.11 THz = 13 meV) and thus partially hindering interband damping of the plasmons. In Fig. 8.8a we show an overlap of the calculated plasmon fringe position as a function of carrier density as a solid curve. The excellent agreement between experiment and theory shown verifies both the electrical tunability of acoustic graphene plasmons, as well as their existence at the charge neutrality point.

8.3.5. Origin of the damping

Ref. 116 further discusses the origin of the losses in for terahertz plasmons in the low carrier density regime. The main result is that there is a strong carrier density dependent change of damping. This is in accordance with Coulomb scattering by charge impurities.[110] It is thus concluded that for small carrier densities in the terahertz in high quality graphene devices, as is the case here, the main source of damping is charge impurity scattering[110] and not acoustic phonon scattering like for high carrier densities.[100] This is corroborated by comparison with microscopic theoretical calculations done by Alessandro Principi and Marco Polini. This sheds light also on the discrepancy between the acoustic phonon limit for the transport mobility and the observed mobilities.[35,64]

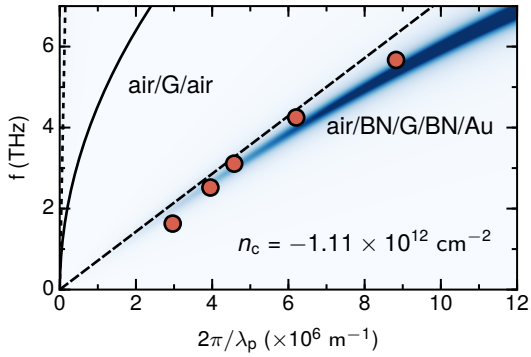

Fig. 8.7.: Experimental and theoretical frequency dispersion of the terahertz plasmons. The symbols show the experimental plasmon momenta extracted from Fig. 8.6. The blue colour plot shows the calculated dispersion of graphene plasmons in an air/h-BN/graphene/h-BN/AuPd/SiO_2 heterostructure with the experimental carrier concentration and layer thicknesses. The black solid curve shows the calculated plasmon dispersion for free-standing graphene (air/G/air) of the same carrier concentration. The dashed black line displays the plasmon dispersion approximated for acoustic plasmons (see ref. 116). The dashed black line with momenta close to zero is the light line in free-space. The carrier density was $n_{c1} = 0.77 \times 10^{12}\,\mathrm{cm}^{-2}$ and $n_{c2} = -1.11 \times 10^{12}\,\mathrm{cm}^{-2}$.

8.4. Conclusion

In conclusion, we have shown that a graphene junction can be used to electrically detect mid-infrared and terahertz plasmons that are carried by the graphene itself. The measurements in both infrared and terahertz show behaviour that is indicative of the photothermoelectric effect. The presented concept opens the door to broadband graphene plasmonic devices where inefficient plasmon out-coupling to light is unnecessary. The observed photocurrent signals are well above the noise level and thus this type of detector in the future could be used together with electrical plasmon sources, for example based on thermal[161] or tunneling emission,[238] resulting in complete on-chip optical systems at sizes far below the light diffraction limit. The presented results also show that near-field photocurrent nanoscopy is an ideal tool to study and map local terahertz photocurrent in nanoscale semiconductor devices or other two dimensional materials with unprecedented detail.

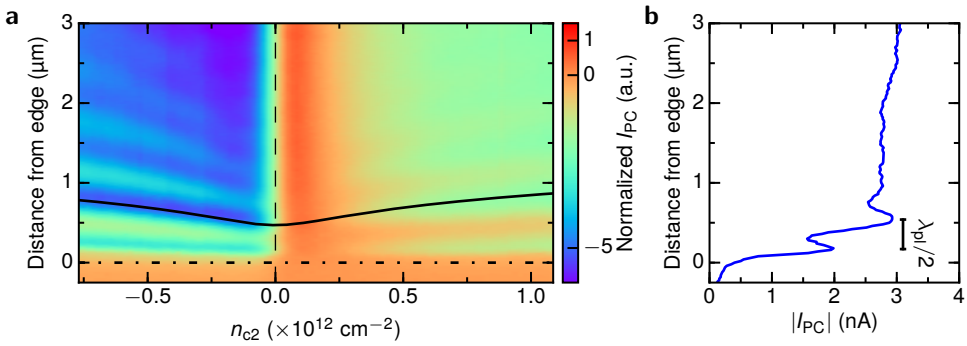

Fig. 8.8.: Measured gate dependence of the terahertz plasmons. **a** Near-field photocurrent signal measured by changing the carrier density of the graphene. We can see a clear change of the plasmon wavelength as indicated by the changing fringe spacing with changing carrier density. This measurement was recorded by the tip scanning perpendicular to the graphene edge and a changing carrier density n_{c2}. The illumination frequency was fixed at $f = 3.11\,\mathrm{THz}$ and the carrier density at $n_{c1} = 0.11 \times 10^{12}\,\mathrm{cm}^{-2}$. The black solid line shows the theoretically expected dependence of the fringe position with carrier density. The dashed vertical line indicates the charge neutrality point which is simultaneously probed by direct-current electrical measurements. **b** Photocurrent profile at the charge neutrality point (along the vertical dashed line in **a**) shows indication of plasmon fringes.

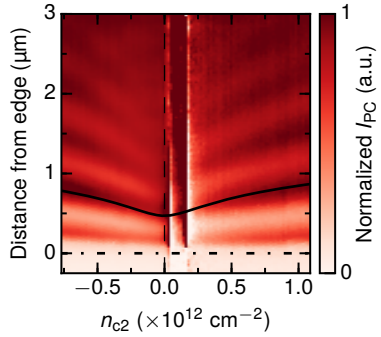

Fig. 8.9.: Normalized measured gate dependence of the terahertz plasmons. After normalization the gate dependent plasmon fringes are visible for carrier densities close to the charge neutrality point in the photocurrent measurement shown in Fig. 8.8. Normalization done to the photocurrent measured 4 μm away from the graphene edge where no fringes are visible.

9. Electrical detection of h-BN phonon polaritons

In this chapter we will show how hyperbolic phonon polaritons (HPPs) in hexagonal boron nitride (h-BN) can be detected electrically both in the near- and far-field using graphene photodetectors.

Light properties in the mid-infrared can be controlled at a deep subwavelength scale using HPPs of h-BN.[78,79,82,84,239] While propagating as waveguided modes[79,80,82] HPPs can concentrate the electric field in a chosen nanovolume.[78,79] Such a behavior is at the heart of many applications including subdiffraction imaging[78,79] and sensing. Here, we employ HPPs in heterostructures of h-BN and graphene as new nano-optoelectronic platform by uniting the benefits of efficient hot-carrier photoconversion in graphene and the hyperbolic nature of h-BN. We demonstrate electrical detection of HPPs by guiding them towards a graphene pn-junction. We shine a laser beam onto a gap in metal gates underneath the heterostructure, where the light is converted into HPPs. The HPPs then propagate as confined rays heating up the graphene leading to a strong photocurrent. This concept is exploited to boost the external responsivity of mid-infrared photodetectors, overcoming the limitation of graphene pn-junction detectors due to their small active area and weak absorption. Moreover this type of detector exhibits tunable frequency selectivity due to the HPPs, which combined with its high responsivity paves the way for efficient high-resolution mid-infrared imaging.

As explained in detail in section 1.3.2 h-BN is a natural hyperbolic material as in the two so called reststrahlen bands (760–825 cm^{-1} and 1360–1610 cm^{-1}) the in plane ($\epsilon_{x,y}$) and the out of plane (ϵ_z) permittivity are of opposite sign.[78,79,82] As a consequence, h-BN supports propagating hyperbolic phonon-polaritons (HPPs) which are electromagnetic modes[78,79] originating in the coupling of photons to optical phonons. Because of their unique physical properties such as long lifetime, tunability,[84] slow propagation velocity,[80] and strong field confinement the HPPs have a great potential for applications in nanophotonics. The capability to concentrate light into small volumes can also have far-reaching implications for opto-electronic technologies, such as mid-infrared photodetection,[87,179–181,240–242] on-chip spectroscopy and sensing. These concepts, however, remain underexplored.

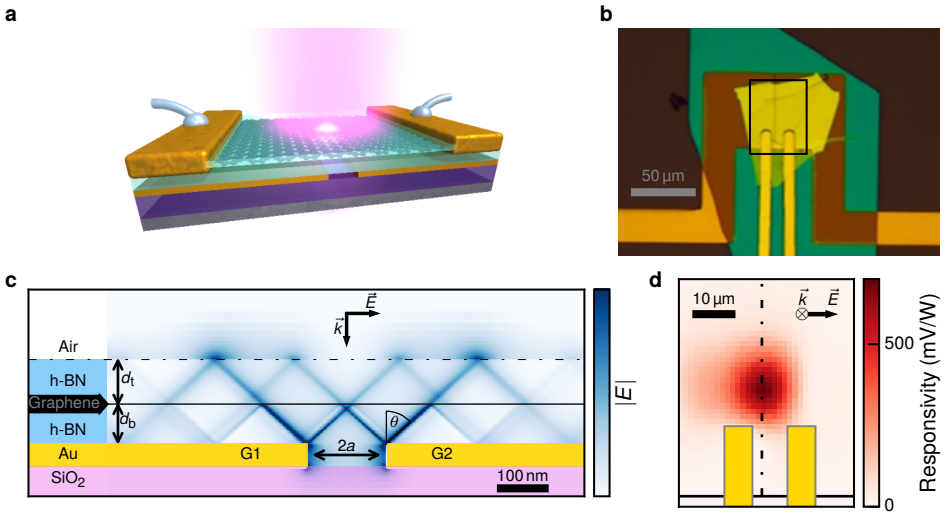

Fig. 9.1.: Device schematic and working principle. **a** Schematic of the encapsulated graphene pn-junction. The h-BN/graphene/h-BN is placed on two gold split gates and contacted electrically by the edges. **b** Optical image of one device: the top (bottom) BN is blue (yellow). The black rectangle indicates the measurement region in **d**. The distance between the two gates in this device is 100 nm. **c** Side view of the propagating hyperbolic phonon-polaritons simulated by FDTD for the device in **b**. The thickness of the bottom h-BN is 50 nm and the top h-BN is 55 nm. HPPs are launched at the edges of the split gates and propagate as directional rays. While they cross the graphene plane they are partially absorbed leading to a temperature increase in the graphene. **d** Spatial map of the device responsivity for a polarization of the laser perpendicular to the gap of the split gate. The photoresponse arises at the junction, indicated by the dashed-dotted line. The graphene edge is indicated by the solid black line. The gate voltages used here are ($V_{g1} = 1.2\,V$ and $V_{g2} = -0.21\,V$). The electric field polarization and propagation direction (E,k) are represented in panels **c** and **d**.

Here we present a hyperbolic opto-electronic device that takes advantage of h-BN being at the same time an ideal substrate for graphene as well as an excellent waveguide for HPPs. We show how HPPs can be exploited to concentrate the electric field of incident mid-infrared beam towards a graphene pn-junction, where it is converted to a photovoltage. The impact of the HPPs leads to a strongly increased responsivity of the graphene pn-

junction in the mid-infrared up to 1 V/W, with zero bias applied.

In previous studies graphene pn-junctions have shown very high internal efficiencies [158,162,163,165,166,182] due to the strong photo-thermoelectric effect in graphene. However, the active area of this type of devices is extremely small, leading to poor light collection. For detecting mid-infrared light this issue is even more acute. By exciting hyperbolic phonon polaritons we strongly enhance the effective absorption. We compare our experimental results with FDTD simulations and an analytical model, providing insight into the underlying physical processes and the frequency tunability of our novel mid-infrared detectors.

9.0.1. Device details

The devices were fabricated by Diana Davydovskaya at ICFO and Yuanda Gao in the group of James Hone at Columbia University according to our input. The investigated devices consist of heterostructures of monolayer graphene encapsulated in h-BN, obtained by the polymer-free van der Waals assembly technique, [35] and placed on top of two metal gates separated by a narrow gap (Fig. 9.1a). The graphene layer has a mobility of $\sim$ 30000 $\mathrm{cm}^2/\mathrm{Vs}$. It is electrically connected to the source and drain electrodes by edge contacts (see sec. 1.3.1). [35] An optical micrograph of a typical device is shown in Fig. 9.1b. The individually tunable carrier density on both sides of the split gate is used to tune the photosensitivity of our device. [162,166,182]

9.0.2. Electrical device characterization

Electrical properties of the pn junction devices are first characterized by recording the drain current under a bias voltage of 5 mV by sweeping simultaneously the two gate voltages (V_{g1}, V_{g2}) from -3 to 3 V. From this measurement we obtain the gate dependence of the device resistance when the entire graphene sheet is uniformly doped. The experimental curve is fitted using the following equation:

$$R_{tot} = R_c + \frac{1}{e\mu\sqrt{n_0^2 + (\epsilon\epsilon_0 V_g/e)^2}} \tag{9.1}$$

where R_c is the sum of both contact resistances, e is the elementary charge, μ is the carrier mobility, ϵ_0 is the vacuum permittivity, ϵ is the DC permittivity of h-BN, n_0 is the residual doping at the charge neutrality voltage and V_g is the gate voltage shift with respect to the charge neutrality voltage. In the case of the device in Fig. 9.1 the fit yields $R_c = 1500\,\Omega\mu\mathrm{m}$ and $\mu = 30963\,\mathrm{cm}^2\,\mathrm{V}^{-1}\,\mathrm{s}^{-1}$. The gate dependence map of the device resistance shown in Fig. 9.4a is measured by sweeping both gates independently in the range (-3 V, 3 V). The cross pattern is a clear sign of independent and stable gate efficiency and allows the access to the four doping configurations: pn, np, pp' and nn'.

The setup used for the far-field measurements is described in more details in sec. 5.2.1. The laser is modulated at 128 Hz using a chopper and the current at the junction is measured using a current pre-amplifier and lock-in amplifier. The polarization of the light is controlled using a ZnSe wire grid polarizer. The power for each frequency is measured using a thermal power meter and the photocurrent spectra are normalized by this power to calculate the responsivity.

9.1. Operation principle

The operation of our device is as follows. HPPs are launched at the sharp gold edges of the split gate when the laser beam illuminates the sample under normal incidence with the polarization perpendicular to the gap between the gate electrodes.[79,80,243] While the HPPs propagate as highly directional rays in both bottom and top h-BN slabs of the stack, they are absorbed when they pass through graphene (Fig. 9.1c) creating hot carriers. The hot carriers diffuse over a length scale of the electron cooling length (about 0.5–1 µm) and generate a temperature increase peaking at the graphene junction defined by the position of the gap in the metal gates. This inhomogeneous temperature distribution induces a photovoltage due to the Seebeck effect. Thus, all HPPs absorbed within approximately one cooling length from the junction contribute to the photovoltage. Similar HPPs lauching presumably also occurs at the source and drain gold contacts. However, they do not contribute to the photovoltage because the electrodes are situated much further than the electron cooling length from the junction.

The measured spatially resolved photoresponse of the device is shown in Fig. 9.1d. The photoresponse arises mainly at the junction (shown as a dashed line). In such a graphene junction the photovoltage V_{ph} is generated by the photo-thermoelectric effect:[162,164,166,182]

$$V_{ph} = \Delta S \Delta T \tag{9.2}$$

where, $\Delta S = S_1 - S_2$ is the difference between the Seebeck coefficients of graphene on the left and right side of the junction and ΔT is the difference in electronic temperature at the junction and at the source/drain contacts. The photo-thermoelectric effect dominates over other possible mechanisms of photovoltage generation due to the high Seebeck coefficient of graphene ($S \sim 100\,\mu V\,K^{-1}$), which is in-situ tunable by gating.[162,170]

9.1.1. Photocurrent generation

The photoresponse is probed by focusing the laser beam on the junction and by sweeping the two gate voltages from $-3\,V$ to $3\,V$ without biasing the device. The obtained gate dependence of the responsivity exhibits a six fold pattern, a signature of the photo-thermoelectric effect as the photovoltage generation mechanism (Fig. 9.4b).[162,164,166,182] A maximal internal responsivity of about $150\,V/W$ is measured in both pn and np configurations respectively at $1515\,cm^{-1}$ for ($V_{g1} = 1.2\,V$, $V_{g2} = -0.21\,V$) and ($V_{g1} = -0.06\,V$, $V_{g2} = 1.26\,V$) which correspond to a fairly low carrier concentration of about $0.29 \times 10^{12}\,cm^{-2}$ on one side of the junction and $0.23 \times 10^{12}\,cm^{-2}$ on the other side. This corresponds to a pn-configuration with a fairly low doping level of about 0.06 eV. At these optimal doping levels $0.112\,eV < 2E_F < 0.126\,eV$ is always lower than the probed energy range of the reststrahlen band ($0.168\,eV < E_L < 0.198\,eV$) meaning that the HPPs absorption by the graphene is never limited by Pauli blocking. In order to be quantitative we simulated the graphene absorption at $1515\,cm^{-1}$ for a symmetric doping in the two regions of the junction variable in the range ($0 < E_F < 0.15\,eV$). As shown on Fig. 9.4c the absorption only drops by 10% at the doping where the thermoelectric effect is the most efficient and by 50% for the highest doping level explored ($E_F = 0.136\,eV$).

The spectral responsivity (Fig. 9.2a) is obtained by recording the photovoltage while tuning the wavelength of the quantum cascade laser source from 1000 to $1610\,cm^{-1}$. A

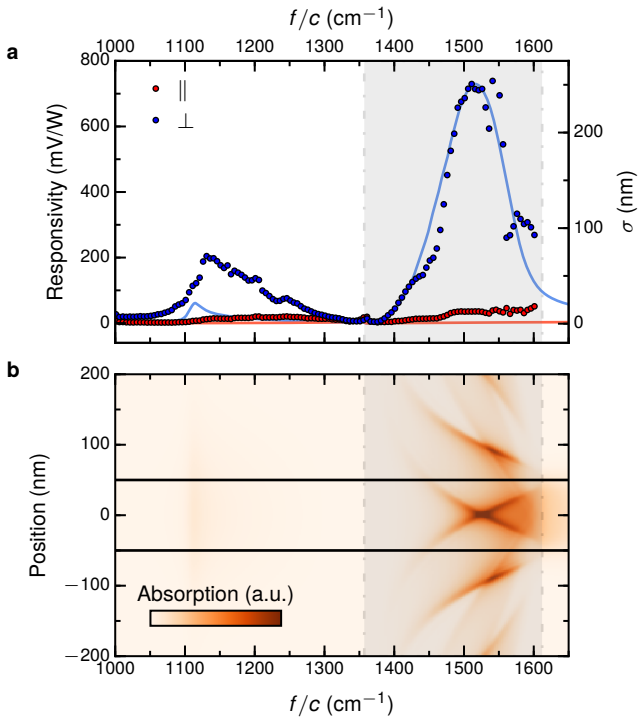

Fig. 9.2.: Absorption and photocurrent spectra. **a** Responsivity spectrum for light polarisation perpendicular (parallel) to the junction in blue (red). The gate voltages used here are ($V_{g1} = 1.2\,V$ and $V_{g2} = -0.21\,V$). The main peak which lies in the upper reststrahlen band of h-BN (grey shaded region) is the result of the hyperbolic phonon-polariton assisted photoresponse. Solid lines are absorption spectra simulated by FDTD. The peak around $1100\,cm^{-1}$ is related with the SiO_2 surface phonon of the underlying substrate.[164] **b** FDTD simulation of the spatial absorption profile in the vicinity of the junction as a function of the laser frequency. The spatial integral at each frequency is proportional to the simulated absorption cross section spectrum in **a**.

strong photocurrent enhancement for the polarization perpendicular to the gap, peaking at $1515\,cm^{-1}$, is observed.

In order to understand the observed behavior we use finite difference time domain (FDTD) simulations to model the scattering process of far-field light into HPPs and the subsequent HPP waveguiding and absorption of the HPPs in the graphene (solid lines in Fig. 9.2a). A good match with the experimentally observed spectral response is obtained (points in Fig. 9.2a). The simulated absorption spectrum shows a peak inside the reststrahlen band of h-BN. The spatial distribution of the electric field inside the h-BN layers is shown in Fig. 9.3b. It is dominated by four rays which are launched at the edges of the split gate and undergo multiple reflections from the top and bottom surfaces. The rays maintain a fixed angle with the c-axis. This angle is related to the anisotropy of the permittivity via the analytical formula $\tan\theta(\omega) = i\sqrt{\epsilon_{x,y}(\omega)}/\sqrt{\epsilon_z(\omega)}$.[78,79] It predicts that $|\theta|$ changes from $\pi/2$ to 0 as ω varies across the reststrahlen band. The unusual ray pattern of HPP emission in turn affects the spatial absorption pattern in graphene, which

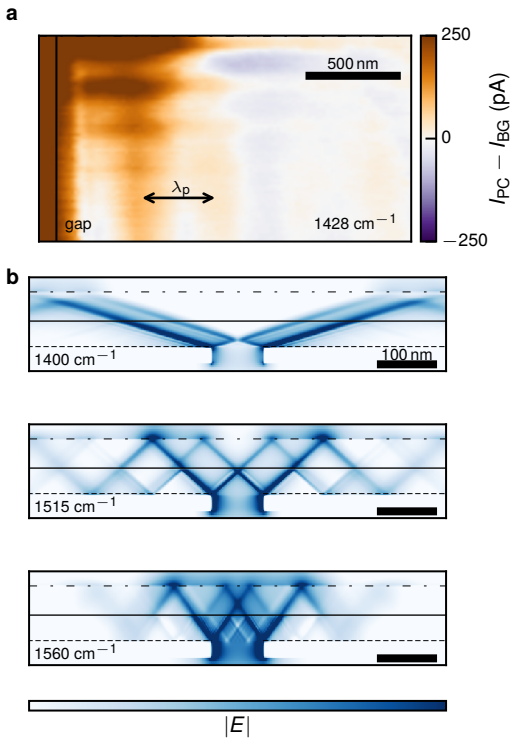

Fig. 9.3.: Near-field photocurrent measurement and simulated propagating HPPs. **a** Near-field photocurrent measurement with subtracted background photocurrent of a similar device with 42 nm of bottom h-BN thickness, 13 nm on top and a gap width of 50 nm. The top edge of the panel is the edge of the graphene and the gap position is indicated. The left gate is set to −2 V and the right gate to 0.1 V. **b** Side views of the propagating HPPs at 1400 cm^{-1} (below the maximum), 1515 cm^{-1} (at the maximum) and at 1560 cm^{-1} (above the maximum) respectively.

is shown in the simulated spectral-spatial pattern of Fig. 9.2b. This pattern is dominated by the four families of "hot spots" that correspond to the four HPP rays seen in Fig. 9.3b. The separation of hot spots within each family is $2d|\tan\theta|$, where $d = d_t + d_b$ is the total thickness of the h-BN layers (Fig. 9.1c).

FDTD simulation details

The full wave simulations were performed using Lumerical FDTD. The frequency dependent permittivity of the h-BN was taken from ref. 78. The optical conductivity of the graphene was calculated using the local random phase approximation at T = 300 K with a scattering time of 500 fs. For each device the appropriate Fermi energy was used in the simulations, however this did not influence the results significantly. In the simulations the Fermi energy of the graphene is spatially constant (see the comment after eq. 9.5) but frequency dependent. A plane wave source was used and the absorption cross section was calculated by normalizing to the incident power. For simplicity the calculated absorption does not take into account the cooling length of the graphene nor the carrier density

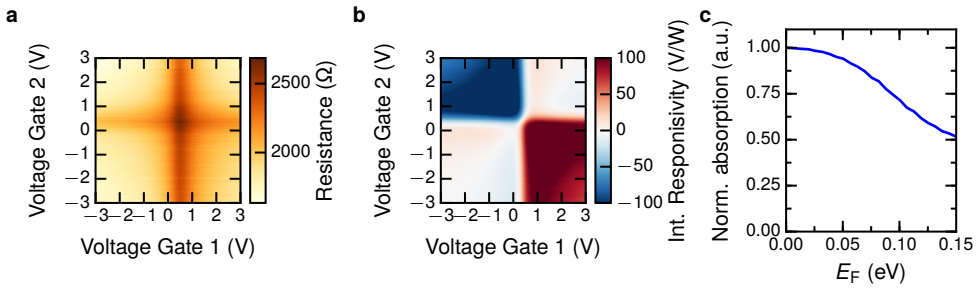

Fig. 9.4.: Gate dependence of resistance and photocurrent and Fermi energy dependent absorption. a Gate dependence of the device resistance. **b** Gate dependence of the internal responsivity at laser frequency 1515 cm^{-1}. **c** Simulated normalized absorption at 1515 cm^{-1} for $V_{g1} = -V_{g2}$.

profile.

9.2. s-SNOM measurements of the phonon polaritons

To investigate further the origin of the observed spectral peaks in the photocurrent and further corroborate their phononic origin we carried out scanning near-field photocurrent mapping of our devices.[195,233] In this technique a metallized atomic force microscopy tip is illuminated with an infrared laser and a near-field is generated at the apex of the tip. This enables us to measure the photocurrent with a spatial resolution greatly exceeding the diffraction limit of light.[195] The representative results are shown in Fig. 9.3a. The device region measured includes the gap of the split gate and one graphene edge localized at the top of the frame.

The obtained photocurrent map reveals two series of sinusoidal spatial oscillations (fringes) rather than sharply peaked hot spots seen in Fig. 9.2b. These smooth oscillations can be explained if we recall that in an h-BN slab of small enough thickness d the HPPs are quantized into discrete eigenmodes with in-plane momenta $k_l = \tan\theta(\pi l + \phi)/d$ where $l = 0, 1, 2, \ldots$ is the mode index and $\phi \sim 1$ is a phase shift that depends on the boundary conditions (see Fig. 9.5b and e.g., Ref. 244). The collimated rays seen in Fig. 9.3b can be understood as coherent superpositions of many such modes emitted by the split-gate. On the other hand, in the photocurrent microscopy the role of the HPP emitter is played by an AFM tip, which apparently couples predominantly to the $l = 0$ mode.[81] The horizontal fringes in Fig. 9.3a are due to interference of $l = 0$ polariton waves launched by the tip, which is backreflected at the graphene edge leading to a fringe spacing corresponding to half the wavelength $\lambda_p = 2\pi/k_0$ of this mode.[81] The vertical fringes are due to interference of the $l = 0$ partial wave launched at the split gate[80] with the tip launched waves. In this case the fringe spacing is λ_p. We do not observe HPPs launched by the tip and reflected by the gap as there are no vertical fringes with half the wavelength visible. This interpretation enables us to extract λ_p from the fringe spacing in the photocurrent maps. For example, at 1428 cm^{-1} is $\lambda_p = 460 \pm 5$ nm, which agrees with the calculated wavelength of 455 nm. The observed fringes parallel to the gap on the left of Fig. 9.3a confirm that phonons are indeed launched by the split gate and are converted into photocurrent.

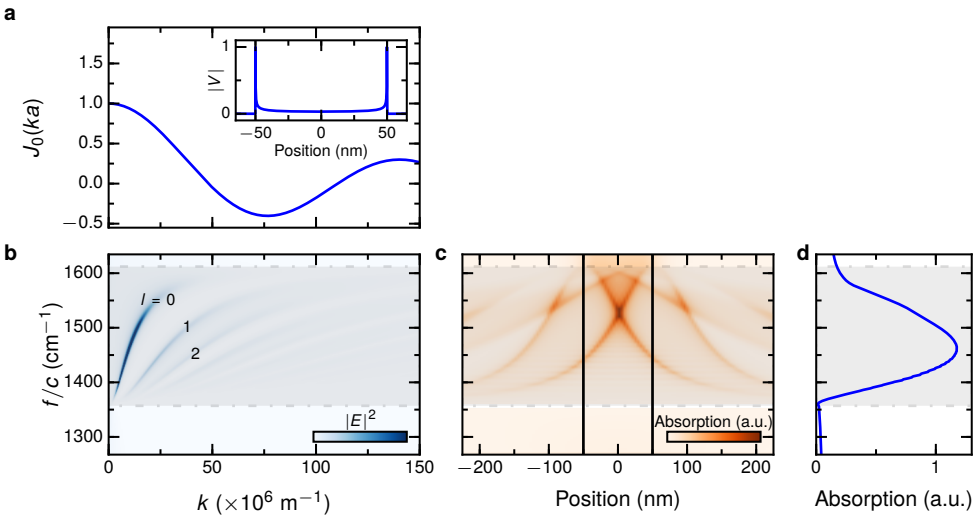

Fig. 9.5.: Analytic calculation of absorption spectra. **a** Momentum distribution provided by a metallic split gate with 100 nm gap width. The associated electric field profile is shown in the inset. **b** HPP frequency dispersion curves showing discrete eigenmodes $l = 0, 1, 2, \ldots$ calculated for the full system of a metal gate, 50 nm h-BN, graphene and 55 nm h-BN on top. **c** Real space absorption profile obtained from the analytic calculations. **d** The resulting absorption spectrum calculated in k-space of the total power absorbed inside the graphene.

9.3. Analytic device model

The analytic model described in the following was developed in collaboration with Jhih-Sheng Wu and Michael M. Fogler from UCSD. In order to better understand which parameters determine the absorption spectrum we also modelled the system analytically.[244] In this model we approximate the electric fields at the bottom surface of the h-BN by the electric field inside the gap $-a < x < a$ cut along the y-axis in a perfectly conducting plane $z = 0$ in vacuum:

$$E_x(x, z = 0) = \frac{V_0}{\pi} \operatorname{Re} \frac{1}{\sqrt{a^2 - x^2}} . \tag{9.3}$$

Here V_0 is the voltage across the gap, which is proportional to the field of the incident beam (see inset Fig. 9.5a).

The Fourier transform of E_x is given by (Fig. 9.5a)

$$\widetilde{E}_x(k) = V_0 J_0(ka), \tag{9.4}$$

where $J_0(z)$ is the Bessel function of the first kind.

We then compute the field inside the h-BN-graphene layered structure using the transfer matrix method (Fig. 9.5b) by assuming that Eq. 9.4 represents the field incident on the structure from the bottom. The assumption is not strictly self-consistent because it does not account for the backreaction of h-BN on the split-gate, in the form of the HPP rays reflected back to $z = 0$ plane. A more accurate but also more complicated model that

obeys the self-consistency condition has been developed by Jhih-Sheng Wu and Michael M. Fogler from UCSD and is presented in the supplement of ref. 245.

We calculate the Fourier transform of the in-plane electric field at the graphene surface as a function of momentum k. The power absorbed in the graphene is then expressed as (Fig. 9.5d):

$$p = \frac{1}{4\pi} \operatorname{Re}\sigma(\omega) \int |\widetilde{E}_x(k)|^2 dk \,, \tag{9.5}$$

where $\sigma(\omega)$ is the sheet conductivity of graphene at the laser frequency ω. Here, for simplicity, we neglect the spatial variation of σ near the pn-junction as the hot spots responsible for the absorption are typically found some distance away from the junction (Fig. 9.5c).

From this model description it becomes clear that the characteristic momentum $k \sim 1/a$ provided by the junction plays a crucial role for the frequency of maximum absorption. By calculating the inverse Fourier transform of $\widetilde{E}_x(k)$ we are able to also calculate the spatial profile of the electric field $E_x(x)$ and thus the spatial absorption profile (Fig. 9.5c). The validity of our analytic model can be seen by the close resemblance between the analytically calculated and FDTD simulated frequency dependent absorption profile (compare Fig. 9.2b and 9.5c).

9.3.1. Origin of the photocurrent peak

From this model, the origin of the peak in the spectral photoresponse is the competition between the following two processes: the dielectric losses in the h-BN and the (finite) momentum provided by the junction. First, the losses in the h-BN contribute mainly to the low frequency side due to the imaginary part of the permittivity which peaks at the TO phonon frequency ($1360\,\mathrm{cm}^{-1}$). The impact of this effect on the device responsivity is enhanced by the obtuse angle with which the HPPs are launched, as the intensity of the HPPs reaching the graphene becomes smaller with travelled distance. Second, the momentum provided by the junction is responsible for the responsivity decay on the high frequency side. Interestingly both of these effects depend on the h-BN thickness and on the gap size. It is important to note that the impact of the h-BN thickness is twofold since it is also changing the HPPs dispersion.[78] Thus by choosing the geometrical parameters of the device, the device thickness and gap width, it is possible to tune the frequency as well as amplitude of the photocurrent maximum within the reststrahlen band of h-BN.

9.3.2. Photoresponse tunability

Our analytic model has revealed the effect of two relevant geometrical parameters, the stack thickness ($d_t + d_b$) and the split gate gap width ($2a$), on both the frequency and the maximum absorbed power. In Fig. 9.7 we show these dependences for a large set of geometries: $10\,\mathrm{nm} < d_t + d_b < 150\,\mathrm{nm}$ and $30\,\mathrm{nm} < 2a < 150\,\mathrm{nm}$. The frequency dependence has the shape of a sloping plane of equation:

$$f/c(d_t + d_b, 2a) = \alpha(d_t + d_b) + \beta 2a + 1405 \tag{9.6}$$

Where $\alpha = 0.428 \times 10^9$ and $\beta = 0.292 \times 10^9$.

The map of the absorbed power reveals that the optimal geometry for a high absorption is reached when both the gap width and sample thickness are small.

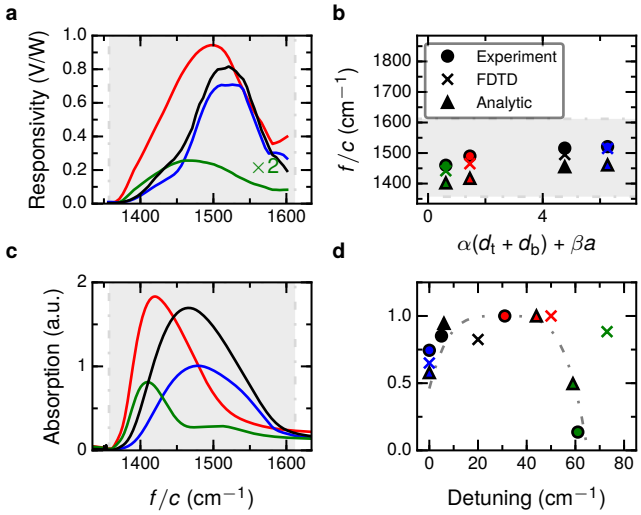

Fig. 9.6.: Comparison between experiments, simulation and analytic model. **a** Responsivity spectra of the investigated devices. **b** Comparison of the peak frequency of the devices obtained experimentally, by FDTD simulation and using the analytic model. Where d_t and d_b are the top and bottom thicknesses of the h-BN respectively and a is the gap width. The parameters α and β are extracted from the analytic model. **c** Absorption spectra calculated analytically. **d** Normalized peak values as a function of the detuning (see text) of its frequency. The gray dashed-dotted line is a guide to the eye. The device parameters for the different devices geometries are given in table A.2 appendix A.2.

9.3.3. Position dependent graphene absorption

In Fig. 9.8b we show the frequency dependent absorption profile of the HPPs by the graphene $\sigma(x)|E(x)|^2$ simulated using the analytic model. The intensity of the electric field $|E(x)|^2$ and the optical conductivity of the graphene pn junction $\sigma(x)$ in the case of symmetric doping ($E_F = \pm 0.1\,\text{eV}$) are respectively presented in Fig. 9.8a and 9.8c. This moderate doping level is the onset of the Pauli blocking, thus the absorption is slightly reduced in the n and p region of the junction but remains unchanged in the intrinsic part of the junction. In Fig. 9.8d we compare the absorbed power spectra of uniformly doped graphene ($E_F = 0.1\,\text{eV}$) and of graphene pn junction ($E_F = \pm 0.1\,\text{eV}$). We observe an extremely weak shift toward the high frequency in the case of the junction. This is explained by the higher weight of the HPPs absorption in the intrinsic part of the junction which takes place at higher frequency.

9.4. Experimental verification of the frequency tunability

In order to show previously simulated frequency tunability, and to validate the physical model, we fabricated different device geometries. Experimental responsivity spectra of the different devices are plotted in Fig. 9.6a. All the spectra were measured using the gate voltage configuration exhibiting the highest responsivity for the respective device. They

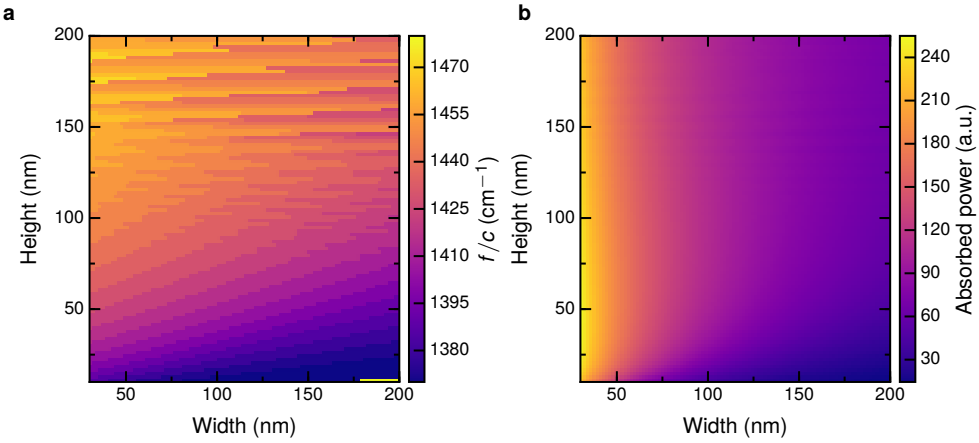

Fig. 9.7.: Analytic model. **a** Geometrical dependence of the peak frequency from the analytical model. **b** Geometrical dependence of the absorbed power from the analytical model.

exhibit different peak frequencies and responsivities and the trend is well captured by the analytically calculated absorption spectra presented in Fig. 9.6c. The peak frequencies are plotted in Fig. 9.6b as a function of the relevant geometrical parameters of the system. These are the stack thickness $d = d_t + d_b$, where d_t and d_b are the bottom and top h-BN thicknesses (Fig. 9.1c), and the split gate gap width $2a$. The tunability of the investigated devices spans over $60\,\mathrm{cm}^{-1}$ and the peak frequencies obtained using both the FDTD simulations and the analytic model match the experimental ones. In Fig. 9.6d we plot the responsivities of the measured devices normalized to the highest one as a function of the peak frequencies. We find that the responsivity follows a bell shaped curve (Fig. 9.6d) suggesting that the optimal geometry would lead to a peak frequency where there is a trade off between low losses and high launching efficiency. Using the analytic model we obtain a theoretical dependence of the frequency and of the absorbed power as a function of the stack thickness and the gap size.

In this simple analytic model the frequency dependence of the gap voltage V_0 (eq. 9.3) is neglected. Thus, the coupling between the far-field light and the split gate is not taken fully into account.[246] This leads to some discrepancy between simple theory and experiment. In collaboration with Jhih-Sheng Wu and Michael M. Fogler we developed a more sophisticated model

9.4.1. Transient device response

We have measured the device time response τ using the quantum cascade laser (Block Engineering LaserScope) as a pulsed light source. In the experiment we record simultaneously the beam reflection on the sample with a MCT detector and the photocurrent of the device. Using a fast oscilloscope (Teledyne Lecroy HDO6104 1GHz High Definition Oscilloscope) to measure the MCT's output we get the laser pulse width $\tau_L = 0.24\,\mu\mathrm{s}$ (Fig. 9.9c). The photoresponse of the device is amplified with a current amplifier (Femto DLPCA-200) and measured with the oscilloscope. In Fig. 9.9c we plot two line traces of

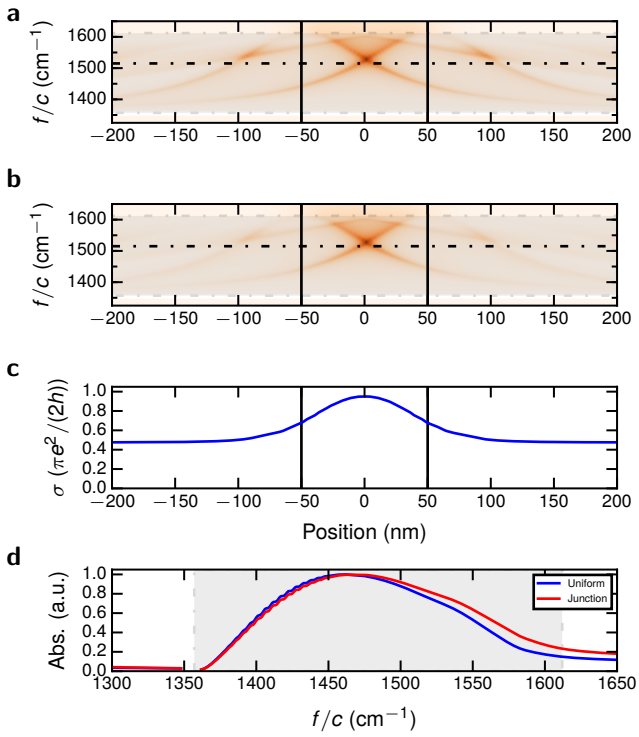

Fig. 9.8.: Position dependent absorption in the graphene. **a** Frequency dependent electric field profile $|E(x)|^2$ simulated with the analytic model. **b** Simulated frequency dependent absorption profile $\sigma(x)|E(x)|^2$. The dashed dotted line indicates where the maximum photocurrent responsivity is observed experimentally. **c** Normalized optical conductivity of the graphene $\sigma(x)$. The doping level is symmetric in the p and n region $E_F = \pm 0.1\,\text{eV}$. **d** Simulated spectra of the absorbed power in the case of uniformly doped graphene ($E_F = 0.1\,\text{eV}$) (blue) and in the case of the pn junction (symmetric doping $E_F = \pm 0.1\,\text{eV}$) but undoped graphene inside the junction.

the photocurrent obtained using two current amplifiers with two different cutoff frequencies of 200 kHz and 500 kHz. These results clearly show that we are limited by the cutoff frequency of the amplifier thus we only get an upper value of the time response $\tau = 2\,\mu\text{s}$.

9.4.2. Noise equivalent power (NEP) estimation

Finally, we will address the photodetection device performance. We remark that the device operates at zero bias, leading to an extremely low noise level ($\sim 4\,\text{nV}/\sqrt{\text{Hz}}$) from which we estimate a noise equivalent power (NEP) of $26\,\text{pW}/\sqrt{\text{Hz}}$. From our simulations we found that the active area is about $2.5\,\mu\text{m}^2$, i.e., only 2.5% of the device area. Thus, the device can be easily scaled to smaller dimensions, with the potential to enhance the performance by another factor of 40 because the total device resistance would be decreased and thus the Johnson-Nyquist noise would decrease as well leading to a lower NEP.

In Fig. 9.9a and b we present respectively the gate dependence of the voltage noise and of the logarithm of the noise equivalent power (log(NEP)). Because graphene pn-junction

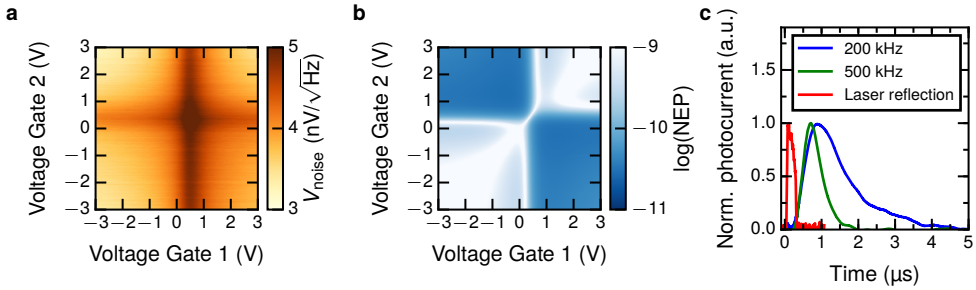

Fig. 9.9.: Gate dependence of resistance and NEP and photocurrent response time. **a** Gate dependence of the Johnson-Nyquist noise. **b** Gate dependence of the log(NEP). **c** Measurement of the device time response. Laser pulse reflection (red). Photocurrent measured using a current amplifier with 500 kHz cutoff frequency (green). Photocurrent measured using a current amplifier with 200 kHz cutoff frequency (blue).

photodetectors operate at zero bias the electrical voltage noise is of thermal Johnson-Nyquist type which can be extracted from the gate dependence resistance map using:

$$S_{\text{noise}} = \sqrt{4k_B T R} \tag{9.7}$$

Where k_B is the Boltzmann constant, $T = 300\,\text{K}$ and $R = 1\,\text{k}\Omega$ is the measured resistance of the full device. The NEP is calculated using:

$$\text{NEP} = S_{\text{noise}}/R_{\text{internal}} \tag{9.8}$$

Where R_{internal} is the internal responsivity. A minimal value of $\text{NEP} = 26\,\text{pW}/\sqrt{\text{Hz}}$ is obtained for $V_{g1} = 1.35\,\text{V}$ and $V_{g2} = -0.48\,\text{V}$, a slightly different gate configuration than for the maximal responsivity. Here $S_{\text{noise}} = 4\,\text{nV}/\sqrt{\text{Hz}}$. The internal responsivity is given by $R_{\text{internal}} = R_{\text{external}}/\eta = 150\,\text{V/W}$ where $R_{\text{external}} = 1\,\text{V/W}$ is the measured responsivity and $\eta = A_{\text{abs}}/A_{\text{spot}} = 0.5\%$ the percentage of absorbed light. $A_{\text{spot}} = 491\,\mu\text{m}^2$ is the laser spot area and $A_{\text{abs}} = \sigma W = 2.5\,\mu\text{m}^2$ is the active area where $\sigma = 250\,\text{nm}$ is the absorption cross section obtained by FDTD simulations and $W = 10\,\mu\text{m}$ is the width of the device.

9.5. Conclusion

We were able to show that hyperbolic phonon polaritons in h-BN can be detected electrically both in the near- and far-field using graphene. We have used a simple analytic model as well as full FDTD simulations to understand the origin of the large photocurrent enhancement observed when launching phonon polaritons. We were able to show how the frequency response of such devices can be tuned. Our novel nano-optoelectronic infrared detectors operate at room temperature, are highly efficient, and can be used for a wide range of on-chip sensing applications.

10. Summary and Outlook

In this thesis we have explored how to engineer the environment for graphene plasmons in such a way that plasmons have long lifetime despite their strong subwavelength confinement (Chapter 3). We have shown that by choosing the right substrate, namely hexagonal boron nitride, graphene plasmons can have a lifetime of up to 500 fs. We have shown that this lifetime is partially limited only by the intrinsic acoustic phonons of the graphene at room temperature, or in other words by the lattice vibrations of the graphene lattice itself. This long lifetime will allow applications of graphene plasmons that were previously extremely difficult or even impossible to achieve such as transformation optics and flat lenses.[20]

In order to take advantage of the long lifetime of graphene plasmons and provide a first proof of principle experiment of flatland transformation optics we have developed a phase modulator for light (Chapter 4). This modulator is able to in situ tune the light phase of the incoming light from 0 to 2π. This is achieved by tuning the graphene plasmon wavelength locally by employing local gates to change the local carrier density. We have provided a simple model of the system, which provides good agreement with the measurement, based on the optical path length of light in a medium in order to provide an easy tool to design such phase modulators. Further more we show that the simple model and data also agree well with a more rigorous scattering theory approach. This experiment provides useful insight into the behaviour of graphene plasmons at charge inhomogeneities and will prove essential for developing flat lenses and other more advanced structures based on graphene plasmons.

In order to extent the scope of conventional s-SNOM we have developed a tool which we called near-field photocurrent nanoscopy (Chapter 7). This allows us to study different optoelectronic properties of graphene at the nanoscale in the mid-infrared region with a resolution of $\sim 100\,\text{nm}$, much below any limitations associated with the 10.6 µm wavelength of the light used for the experiments. Using this technique we gained new insight into the charge density profile of grain boundaries in graphene grown by CVD and imaged charge puddles in exfoliated graphene. We were also able to investigate the charge density profile of graphene encapsulated in hexagonal boron nitride. We gained insight into a previously unknown edge doping mechanism in such devices and showed that by using local conductive gates this type of edge doping could be avoided. This technique will allow new insight into the optoelectronic behaviour of different materials, not only in two dimensions.

We have employed near-field photocurrent nanoscopy to study how graphene plasmons decay into hot carriers and how we are able to detect them directly (Chapter 8). We have used this to study for the first time propagating graphene plasmons in the terahertz frequency range. We have shown experimentally that the graphene plasmon hybridizes with the underlying local metal gates and show an acoustic disperion relation. This will enable studying graphene terahertz physics with a nanoscale resolution as well as on chip graphene plasmonic detectors.

We have then taken advantage of near-field photocurrent nanoscopy to show how we are able to detect phonon polaritons in the reststrahlen band of hexagonal boron nitride electrically (Chapter 9). We combined the near-field technique with far-field scanning photocurrent microscopy and electromagnetic simulations to show the phononic origin of a strong photocurrent enhancement in the graphene in the mid-infrared. Using the photocurrent enhancement we were able to show sensitive, tunable mid-infrared photodetectors based on graphene. This could allow infrared cameras based on such photocurrent enhancement.

To sum up: The works this thesis is based on present significant steps towards applications in such diverse fields as graphene plasmonics and photodetection, exploiting the nano opto-electronic properties of heterostructures of graphene and h-BN.

We provide a possible pathway towards on chip integrated graphene plasmonic devices by significantly advancing the understanding of the lifetime limitations of graphene plasmons and showing that broadband on chip electrical detection of graphene plasmons is possible. We also showed a first device demonstrating the flatland transformation optics capabilities of graphene plasmons and based on this small footprint phase modulator it should be possible to build for example extremely compact interferometers. These different advances add greatly to the toolbox graphene plasmons provide.

We also managed to develop a new nanoscale measurement tool which combines the high spatial resolution of s-SNOM with the optoelectronic insights of scanning photocurrent microscopy. We successfully employed this photocurrent nanoscopy tool to measure different optoelectronic properties of graphene. We used it to study the electrical detection of graphene plasmons in the infrared and terahertz and probed the linear plasmon dispersion for terahertz plasmons close to a metal gate for the first time in real space.

We then employed the tool to show electrical detection of hexagonal boron nitride phonons for the first time. In combination with our far-field measurements and extensive simulations and theory we provide a pathway towards sensitive mid-infrared photodetectors based on graphene.

For future generations of graphene plasmonic devices not only a long propagation length is crucial but also an easy integration without the need for external lasers. This means that it is necessary to eliminate the s-SNOM and the external laser source in the long run to make graphene plasmonic devices a viable competitor for other biological sensing techniques based on graphene or other systems, e.g. compared to using simple electronic readout techniques.[247]

One way to achieve this device miniaturization could be to excite the graphene plasmons fully electrically.[238,248] In other material systems, such as two dimensional electron gases[249–253] and gold nanorods[254] electrical plasmon excitation has already been achieved. Different device geometries could be used for this, such as tunneling junctions where the electrons tunnel form gold or other metals to graphene or graphene/graphene tunnel junctions. In the latter case momentum matching has to be assured by properly aligning the two graphene layers.[255]

Furthermore graphene plasmons could be excited in such a way that their propagation is topologically protected using magnetic fields.[256–258] This would allow even longer plasmon propagation lengths then what is currently possible.

A. Appendices

A.1. h-BN permittivity parameters

Model	l	$\varepsilon_l(\infty)$	$s_{v,l}$	$\hbar\omega_{v,l}$/meV	$\hbar\gamma_{v,l}$/meV
Geick[83]	x, y	4.95	1.868	169.5	3.6
		+	0.209	95.1	3.4
	z	4.10	0.530	97.1	1.0
		+	0.456	187.2	9.9
Cai[259]	x, y	4.87	1.83	170.1	—
	z	2.95	0.61	92.5	—
Caldwell[78]	x, y	4.9	2.001	168.6	0.87
	z	2.95	0.5262	94.2	0.25
Cai "clean"	x, y	4.87	1.83	170.1	0.87
	z	2.95	0.61	92.5	0.25
Cai "damaged"	x, y	4.87	1.83	170.1	6.5
	z	2.95	0.61	92.5	1.9

Table A.1.: Different permittivity models for hexagonal boron nitride. Note that the model of Geick et al. includes two vibrational modes for each direction. Cai et al. do not include any calculations for the losses and thus no parameter $\hbar\gamma_{v,l}$ is given.

The first three models are from the existing literature[78,83,259] and the last two are hybrids that we have constructed in order to fit our experimental results. In future precision studies it may be necessary to take into account (or exploit) the isotope effect of boron which could allow tuning of the resonance frequencies by 3%, or to remove the dielectric loss that originates from the isotope inhomogeneity of natural boron.

The Geick et al. study was performed on a large h-BN sample, and the authours found it necessary to include an additional vibrational mode for each direction, in order to fit their reflectance data. They attributed this necessity to the large degree of axis misalignment among the crystallites, which would mix together the x and z permittivities.[83]

The Cai et al. model in ref. 259 is a theoretical calculation for perfect h-BN. The values of Cai et al. were used successfuly in modelling the propagating phonon polaritons in Ref.[84] (see the supplement of that paper). This study however does not address the expected dielectric losses.

Caldwell et al. present their values in the supplementary material of ref. 78. The permittivity was inferred from reflectance measurements on thin h-BN exfoliated films, originating from the same source as the h-BN films in our study. The parameters obtained are very similar to the Cai et al. values.

Cai "clean" and Cai "damaged" in Table A.1 take the theoretical modes of Ref. 259 and incorporates empirical losses based on refs. 78,83. Cai "clean" uses the losses for pristine

thick films of h-BN as measured in ref. 78. In Cai "damaged" we amplify these losses to appear similar to those observed for thin (<200 nm) h-BN films in the same work. As no data were available on the losses of the z vibrational mode for thin films, we assume that they increase in proportion with the x, y losses.

The model Cai "clean" was used to produced dispersion plots where we have matched the measured plasmon wavelength; its low level of dielectric loss aids the visibility of the modes. This last model, Cai "damaged", was used in our calculations of plasmon damping. The following subsections describe the parameter sets we have considered and how dielectric loss may be modified in thin films of h-BN.

A.2. Electrical phonon detection device parameters

The device parameters used for the simulations of the different devices in chap. 9 as well as the simulation results are shown in table A.2.

d_t (nm)	d_b (nm)	$2a$ (nm)	d_{gate} (nm)	ω_{exp} (cm^{-1})	ω_{sim} (cm^{-1})	E_{F} (meV)
3	30	70	15	1490	1464	72
55	50	100	30	1520	1515	52
9	27	150	15	1460	1447	37
17	60	60	30	1512	1505	82

Table A.2.: Parameters of the experimental devices. The first column is the device number. The dimensions d_t, d_b, and $2a$ are indicated in Fig. 9.1c. Variable d_{gate} is the thickness of the Au split-gate. Frequencies ω_{exp} and ω_{sim} are the positions of thermocurrent maxima in, respectively, experiment and numerical simulations. E_{F} is the Fermi energy of graphene.

Publications

The experimental chapters of this thesis and parts of the introductions are largely based on the following publications:

Chap. 3 A. Woessner,* M.B. Lundeberg,* Y. Gao,* A. Principi, P. Alonso-González, M. Carrega, K. Watanabe, T. Taniguchi, G. Vignale, M. Polini, J. Hone, R. Hillenbrand, F.H.L. Koppens, Highly confined low-loss plasmons in graphene–boron nitride heterostructures, Nature Materials 14, 421-425 (2015)

Chap. 4 A. Woessner,* Y. Gao,* I. Torre, M.B. Lundeberg, C. Tan, K. Watanabe, T. Taniguchi, R. Hillenbrand, M. Polini, J. Hone, F.H.L. Koppens, Voltage-controlled full phase control of infrared light in a 350 nm footprint using graphene plasmons, under review

Chap. 7 A. Woessner, P. Alonso-González,* M.B. Lundeberg,* Y. Gao, J.E. Barrios-Vargas, G. Navickaite, Q. Ma, D. Janner, K. Watanabe, A.W. Cummings, T. Taniguchi, V. Pruneri, S. Roche, P. Jarillo-Herrero, J. Hone, R. Hillenbrand, F.H.L. Koppens, Near-field photocurrent nanoscopy on bare and encapsulated graphene, Nature Communications 7, 10783 (2016)

Chap. 8 M.B. Lundeberg,* Y. Gao,* A. Woessner, C. Tan, P. Alonso-González, K. Watanabe, T. Taniguchi, J. Hone, R. Hillenbrand, F.H.L. Koppens, Thermoelectric detection and imaging of propagating graphene plasmons, Nature Materials 16, 204-207 (2017)
P. Alonso-González, A.Y. Nikitin,* Y. Gao,* A. Woessner,* M.B. Lundeberg, A. Principi, N. Forcellini, W. Yan, S. Vélez, A.J. Huber, K. Watanabe, T. Taniguchi, F. Casanova, L.E. Hueso, M. Polini, J. Hone, F.H.L. Koppens, R. Hillenbrand, Acoustic terahertz graphene plasmons revealed by photocurrent nanoscopy, Nature Nanotechnology 12, 31-35 (2017)

Chap. 9 A. Woessner,* R. Parret,* D. Davydovskaya, Y. Gao, J.-S. Wu, M.B. Lundeberg, S. Nanot, P. Alonso-González, K. Watanabe, T. Taniguchi, R. Hillenbrand, M.M. Fogler, J. Hone, F.H.L. Koppens, Electrical detection of hyperbolic phonon-polaritons in heterostructures of graphene and boron nitride, under review

Other publications by the author (not included as thesis chapters):

M.B. Lundeberg, Y. Gao, R. Asgari, C. Tan, B. Van Duppen, M. Autore, P. Alonso-González, A. Woessner, K. Watanabe, T. Taniguchi, R. Hillenbrand, J. Hone, M. Polini, F.H.L. Koppens, Tuning quantum non-local effects in graphene plasmonics, submitted

F.J. Bezares,* A. De-Sanctis,* J.M. Saavedra,* A. Woessner, P. Alonso-González, I. Amenabar, J. Chen, T.H. Bointon, S. Dai, M.M. Fogler, D.N. Basov, R. Hillenbrand, M.F. Craciun, F.J. García de Abajo, S. Russo, F.H.L. Koppens, Near-field imaging of interaction effects between surface plasmons and intrinsic phonons in highly-doped graphene, in preparation

E. Yoxall, M. Schnell, A.Y. Nikitin, O. Txoperena, A. Woessner, M.B. Lundeberg, F. Casanova, L.E. Hueso, F.H.L. Koppens, R. Hillenbrand, Direct observation of ultra-slow hyperbolic polariton propagation with negative phase velocity, Nature Photonics 9, 674–678 (2015)

K.J. Tielrooij, L. Piatkowski, M. Massicotte, A. Woessner, Q. Ma, K. Myhro, J. Lau, P. Jarillo-Herrero, N.F. van Hulst, F.H.L. Koppens, Femtosecond photovoltage generation through efficient carrier heating in graphene, Nature Nanotechnology 10, 437–443 (2015)

K.J. Tielrooij,* M. Massicotte,* L. Piatkowski, A. Woessner, Q. Ma, P. Jarillo-Herrero, N.F. van Hulst, F.H.L. Koppens, Hot-carrier photocurrent effects at graphene-metal interfaces, Journal of Physics: Condensed Matter 27, 164207 (2015)

A. Principi, M. Carrega, M.B. Lundeberg, A. Woessner, F.H.L. Koppens, G. Vignale, M. Polini, Plasmon losses due to electron-phonon scattering: The case of graphene encapsulated in hexagonal Boron Nitride, Physical Review B 90, 165408 (2014)

M. Badioli, A. Woessner, K.J. Tielrooij, S. Nanot, G. Navickaite, T.Stauber, F.J. García de Abajo, F.H.L. Koppens, Phonon-mediated mid-infrared photoresponse of graphene, Nano Letters 14 (11), 6374–6381 (2014)

*: These authors contributed equally.

Acknowledgements

First and foremost I would like to thank my advisor Frank Koppens for giving me the opportunity to do a PhD in his group. It has been a great ride and I enjoyed it tremendously. Thanks, Frank for helping me to develop professionally to become a more complete scientist. Also, thanks for giving me all of the great opportunities to learn new things, develop and letting me go to all the beautiful conferences.

Next I have to give my thanks to Mark Lundeberg for working with me over most of my PhD. It was a great pleasure working with you in the lab and seeing you write code. There was no piece of code you were not able to write. I was able to learn so much from you scientifically and personally. I also really enjoyed our discussions about politics and economics and all the things that are connected with it.

The work presented in this thesis would not have been possible without the collaboration with the group of James Hone at Columbia University and especially Yuanda Gao. Yuanda fabricated most of the devices used in this thesis. He is a true master of the van der Waals assembly technique and provided us with near bubble-free, perfect encapsulated devices. He fabricated the device finally used for the phase modulation experiment on his last day at Columbia before setting out for a new adventure at Intel. True dedication! Thanks, Yuanda for the great collaboration!

Thanks to Rainer Hillenbrand and Pablo Alonso-González who I had the honour to collaborate with over all of these years. Thanks Pablo for sharing all of your tricks of operating a near-field microscope. I always enjoyed coming to San Sebastian and working with you. And of course I also enjoyed eating pintxos, chuletas and going to a sidrería.

I would like to thank Marko and Michela for introducing me to measurements of graphene devices and always having an open ear whenever I needed some help. Also for all the great nights and days spent in Castelldefels and Barcelona.

Thanks to all the great past and present members of the (quantum) nano-optoelectronics group, who I had the chance to interact with on a personal and professional level (in no particular order): Gabriele, Klaas, Peter, Carlotta, Stijn, Mathieu, Seb, Ivan, Antoine, Francisco, Romain, Fabien, Kevin, Louis, Diana, Niels, David, Sebastian, Greg, Eric, Bernat, Teresa, Tim, Jianbo, Itai, Emre, Carles, Andreas, Uros, Mara, ...

Thanks also to all the other people at ICFO who I enjoyed spending my time with and who made and make ICFO such a great place to work at. If we ever went for a beer or coffee together, you are probably one of them.

A special thanks goes to Jianbo who showed me around beautiful Beijing and set me up with his friends in Xi'An and Nanjing allowing me to experience China from the best side.

A big thanks to my flatmates Kevin and Simon for the BBQs, paellas and all the other things we did together.

Thanks to all the people in Barcelona I could always count on to go for dinner, drinks, concerts, running, swimming, hiking, paella, board games, the beach and all the other fun stuff (in no particular order): Alexandros, Ioannis, Peter, Benni, Barbara, Pau, Nicolas, Nicolas, James, Erin, Francesco, Sergio, Sotiris, Iñigo, Mussie, Anjana, Franky, Jana,

Roland, Lisa, Nicolò, Lara, Juan, Miriam, Inge, Felix, Jonas, Vacys, Arina, Valeriya and the many others I have probably forgotten to mention.

Thanks to Klaas and Simon for proof reading my thesis and to Sebastian for checking my Spanish abstract.

An dieser Stelle auch Vielen Dank an alle meine Freunde in Deutschland. Danke, dass ich nach so vielen Jahren im Ausland immernoch auf Konzerte und Festivals mit euch gehen kann. Und, das obwohl ich eigentlich viel zu selten von mir hören lasse.

Vielen Dank an meine Eltern Karl-Heinz und Conny für das große Vertrauen, die Unterstützung über die Jahre und, dass ich immer tun konnte was ich wollte.

Bibliography

[1] Ozbay, E. Plasmonics: merging photonics and electronics at nanoscale dimensions. *Science* **311**, 189–93 (2006).

[2] Schuller, J. A. et al. Plasmonics for extreme light concentration and manipulation. *Nature Mater.* **9**, 193–204 (2010).

[3] Fernández-Domínguez, A. I., García-Vidal, F. J. & Martín-Moreno, L. Unrelenting plasmons. *Nature Photon.* **11**, 8–10 (2017).

[4] Kik, P. G. & Brongersma, M. L. *Surface Plasmon Nanophotonics* (Springer Netherlands, Dordrecht, 2007).

[5] Shalaev, V. M. Optical negative-index metamaterials. *Nature Photon.* **1**, 41–48 (2007).

[6] Yu, N. & Capasso, F. Flat optics with designer metasurfaces. *Nature Mater.* **13**, 139–150 (2014).

[7] Tame, M. S. et al. Quantum plasmonics. *Nature Phys.* **9**, 329–340 (2013).

[8] Jablan, M., Buljan, H. & Soljačić, M. Plasmonics in graphene at infrared frequencies. *Phys. Rev. B* **80**, 245435 (2009).

[9] Khurgin, J. B. How to deal with the loss in plasmonics and metamaterials. *Nature Nanotech.* **10**, 2–6 (2015).

[10] Geim, A. K. & Novoselov, K. S. The rise of graphene. *Nature Mater.* **6**, 183–91 (2007).

[11] Grigorenko, A. N., Polini, M. & Novoselov, K. S. Graphene plasmonics. *Nature Photon.* **6**, 749–758 (2012).

[12] Garcia de Abajo, F. J. Graphene Nanophotonics. *Science* **339**, 917–918 (2013).

[13] Jablan, M., Soljacic, M. & Buljan, H. Plasmons in Graphene: Fundamental Properties and Potential Applications. *Proc. IEEE* **101**, 1689–1704 (2013).

[14] García de Abajo, F. J. Graphene Plasmonics: Challenges and Opportunities. *ACS Photonics* **1**, 135–152 (2014).

[15] Low, T. & Avouris, P. Graphene plasmonics for terahertz to mid-infrared applications. *ACS Nano* **8**, 1086–1101 (2014).

[16] Basov, D. N., Fogler, M. M. & Garcia de Abajo, F. J. Polaritons in van der Waals materials. *Science* **354**, 1992 (2016).

[17] Low, T. et al. Polaritons in layered two-dimensional materials. *Nature Mater.* 1610.04548 (2016).

[18] Koppens, F. H. L., Chang, D. E., García de Abajo, F. J. & de Abajo, F. J. Graphene Plasmonics: A Platform for Strong Light-Matter Interactions. *Nano Lett.* **11**, 3370–3377 (2011).

[19] Rivera, N., Kaminer, I., Zhen, B., Joannopoulos, J. D. & Solja i, M. Shrinking light to allow forbidden transitions on the atomic scale. *Science* **353**, 263–269 (2016).

[20] Vakil, A. & Engheta, N. Transformation optics using graphene. *Science* **332**, 1291–1294 (2011).

[21] Rodrigo, D. et al. Mid-infrared plasmonic biosensing with graphene. *Science* **349**, 165–168 (2015).

[22] Chakraborty, S. et al. Gain modulation by graphene plasmons in aperiodic lattice lasers. *Science* **351**, 246–248 (2016).

[23] Polini, M. Tuning terahertz lasers via graphene plasmons. *Science* **351**, 229–231 (2016).

[24] Wunsch, B., Stauber, T., Sols, F. & Guinea, F. Dynamical polarization of graphene at finite doping. *New J. Phys.* **8**, 318 (2006).

[25] Hwang, E. H. & Das Sarma, S. Dielectric function, screening, and plasmons in two-dimensional graphene. *Phys. Rev. B* **75**, 205418 (2007).

[26] Principi, A., Polini, M. & Vignale, G. Linear response of doped graphene sheets to vector potentials. *Phys. Rev. B* **80**, 075418 (2009).

[27] Christensen, J., Manjavacas, A., Thongrattanasiri, S., Koppens, F. H. L. & García de Abajo, F. J. Graphene plasmon waveguiding and hybridization in individual and paired nanoribbons. *ACS Nano* **6**, 431–440 (2012).

[28] Gullans, M. et al. Single-Photon Nonlinear Optics with Graphene Plasmons. *Phys. Rev. Lett.* **111**, 247401 (2013).

[29] Fei, Z. et al. Gate-tuning of graphene plasmons revealed by infrared nano-imaging. *Nature* **487**, 82–5 (2012).

[30] Chen, J. et al. Optical nano-imaging of gate-tunable graphene plasmons. *Nature* **487**, 77–81 (2012).

[31] Ju, L. et al. Graphene plasmonics for tunable terahertz metamaterials. *Nature Nanotech.* **6**, 630–634 (2011).

[32] Yan, H. et al. Damping pathways of mid-infrared plasmons in graphene nanostructures. *Nature Photon.* **7**, 394–399 (2013).

[33] Buljan, H., Jablan, M. & Soljačić, M. Graphene plasmonics: Damping of plasmons in graphene. *Nature Photon.* **7**, 346–348 (2013).

[34] Dean, C. R. et al. Boron nitride substrates for high-quality graphene electronics. *Nature Nanotech.* **5**, 722–726 (2010).

[35] Wang, L. et al. One-dimensional electrical contact to a two-dimensional material. *Science* **342**, 614–617 (2013).

[36] Keilmann, F. & Hillenbrand, R. Near-field microscopy by elastic light scattering from a tip. *Phil. Trans. R. Soc. A* **362**, 787–805 (2004).

[37] Castro Neto, A. H., Guinea, F., Peres, N. M. R., Novoselov, K. S. & Geim, A. K. The electronic properties of graphene. *Rev. Mod. Phys.* **81**, 109–162 (2009).

[38] Novoselov, K. S. et al. Electric field effect in atomically thin carbon films. *Science* **306**, 666–669 (2004).

[39] Novoselov, K. S. Nobel Lecture: Graphene: Materials in the Flatland. *Rev. Mod. Phys.* **83**, 837–849 (2011).

[40] Geim, A. K. Nobel Lecture: Random walk to graphene. *Rev. Mod. Phys.* **83**, 851–862 (2011).

[41] Zhang, Y., Tan, Y.-W., Stormer, H. L. & Kim, P. Experimental observation of the quantum Hall effect and Berry's phase in graphene. *Nature* **438**, 201–204 (2005).

[42] Novoselov, K. S. et al. Two-dimensional gas of massless Dirac fermions in graphene. *Nature* **438**, 197–200 (2005).

[43] Das Sarma, S., Adam, S., Hwang, E. H. & Rossi, E. Electronic transport in two-dimensional graphene. *Rev. Mod. Phys.* **83**, 407–470 (2011).

[44] Jang, C. et al. Tuning the effective fine structure constant in graphene: Opposing effects of dielectric screening on short- and long-range potential scattering. *Phys. Rev. Lett.* **101**, 1–4 (2008).

[45] Adam, S., Hwang, E. H., Galitski, V. M. & Das Sarma, S. A self-consistent theory for graphene transport. *Proc. Natl. Acad. Sci.* **104**, 18392–7 (2007).

[46] Du, X., Skachko, I., Barker, A. & Andrei, E. Y. Approaching ballistic transport in suspended graphene. *Nature Nanotech.* **3**, 491–495 (2008).

[47] Hwang, E. & Das Sarma, S. Acoustic phonon scattering limited carrier mobility in two-dimensional extrinsic graphene. *Phys. Rev. B* **77**, 115449 (2008).

[48] Banszerus, L. et al. Ballistic Transport Exceeding 28 μm in CVD Grown Graphene. *Nano Lett.* **16**, 1387–1391 (2016).

[49] Nair, R. R. et al. Fine structure constant defines visual transparency of graphene. *Science* **320**, 1308 (2008).

[50] Li, Z. Q. et al. Dirac charge dynamics in graphene by infrared spectroscopy. *Nature Phys.* **4**, 532–535 (2008).

[51] Mak, K. F. et al. Measurement of the Optical Conductivity of Graphene. *Phys. Rev. Lett.* **101**, 196405 (2008).

[52] Yan, H. et al. Tunable infrared plasmonic devices using graphene/insulator stacks. *Nature Nanotech.* **7**, 330–334 (2012).

[53] Tielrooij, K. J. et al. Generation of photovoltage in graphene on a femtosecond timescale through efficient carrier heating. *Nature Nanotech.* **10**, 437–443 (2015).

[54] Tielrooij, K. J. et al. Hot-carrier photocurrent effects at graphene–metal interfaces. *J. Phys. Condens. Matter* **27**, 164207 (2015).

[55] Blake, P. et al. Making graphene visible. *Appl. Phys. Lett.* **91**, 063124 (2007).

[56] Falkovsky, L. A. & Varlamov, A. A. Space-time dispersion of graphene conductivity. *The European Physical Journal B* **56**, 281–284 (2007).

[57] Falkovsky, L. A. Optical properties of graphene. *J. Phys. Condens. Matter* **129**, 12004 (2008).

[58] Chen, J.-H., Jang, C., Xiao, S., Ishigami, M. & Fuhrer, M. S. Intrinsic and extrinsic performance limits of graphene devices on SiO2. *Nature Nanotech.* **3**, 206–209 (2008).

[59] Martin, J. et al. Observation of electron–hole puddles in graphene using a scanning single-electron transistor. *Nature Phys.* **4**, 144–148 (2007).

[60] Katsnelson, M. I. & Geim, A. K. Electron scattering on microscopic corrugations in graphene. *Phil. Trans. R. Soc. A* **366**, 195–204 (2008).

[61] Bolotin, K. I., Sikes, K. J., Hone, J., Stormer, H. L. & Kim, P. Temperature-Dependent Transport in Suspended Graphene. *Phys. Rev. Lett.* **101**, 096802 (2008).

[62] Moser, J., Barreiro, A. & Bachtold, A. Current-induced cleaning of graphene. *Appl. Phys. Lett.* **91**, 163513 (2007).

[63] Ferrari, A. C. A. A. C. et al. Science and technology roadmap for graphene, related two-dimensional crystals, and hybrid systems. *Nanoscale* **7**, 4598–4810 (2014).

[64] Banszerus, L. et al. Ultrahigh-mobility graphene devices from chemical vapor deposition on reusable copper. *Science Advances* **1**, e1500222–e1500222 (2015).

[65] Xue, J. et al. Scanning tunnelling microscopy and spectroscopy of ultra-flat graphene on hexagonal boron nitride. *Nature Mater.* **10**, 282–285 (2011).

[66] Gan, X. et al. Chip-integrated ultrafast graphene photodetector with high responsivity. *Nature Photon.* **7**, 883–887 (2013).

[67] Phare, C. T., Daniel Lee, Y.-H., Cardenas, J. & Lipson, M. Graphene electro-optic modulator with 30 GHz bandwidth. *Nature Photon.* **9**, 511–514 (2015).

[68] Pizzocchero, F. et al. The hot pick-up technique for batch assembly of van der Waals heterostructures. *Nature Commun.* **7**, 11894 (2016).

[69] Novoselov, K. S., Mishchenko, A., Carvalho, A., Neto, A. H. C. & Road, O. 2D materials and van der Waals heterostructures. *Science* **353**, aac9439 (2016).

[70] Geim, a. K. & Grigorieva, I. V. Van der Waals heterostructures. *Nature* **499**, 419–425 (2013).

[71] Britnell, L. et al. Field-Effect Tunneling Transistor Based on Vertical Graphene Heterostructures. *Science* **335**, 947–950 (2012).

[72] Britnell, L. et al. Electron tunneling through ultrathin boron nitride crystalline barriers. *Nano Lett.* **12**, 1707–1710 (2012).

[73] Britnell, L. et al. Strong Light-Matter Interactions in Heterostructures of Atomically Thin Films. *Science* **340**, 1311–1314 (2013).

[74] Withers, F. et al. Light-emitting diodes by band-structure engineering in van der Waals heterostructures. *Nature Mater.* **14**, 301–306 (2015).

[75] Avsar, A. et al. Air-Stable Transport in Graphene-Contacted, Fully Encapsulated Ultrathin Black Phosphorus-Based Field-Effect Transistors. *ACS Nano* **9**, 4138–4145 (2015).

[76] Castellanos-Gomez, A. et al. Deterministic transfer of two-dimensional materials by all-dry viscoelastic stamping. *2D Materials* **1**, 011002 (2014).

[77] Watanabe, K., Taniguchi, T. & Kanda, H. Direct-bandgap properties and evidence for ultraviolet lasing of hexagonal boron nitride single crystal. *Nature Mater.* **3**, 404–409 (2004).

[78] Caldwell, J. D. et al. Sub-diffraction, Volume-confined Polaritons in the Natural Hyperbolic Material, Hexagonal Boron Nitride. *Nature Commun.* **5**, 5221 (2014).

[79] Dai, S. et al. Graphene on hexagonal boron nitride as a tunable hyperbolic metamaterial. *Nature Nanotech.* **10**, 682–686 (2015).

[80] Yoxall, E. et al. Direct observation of ultraslow hyperbolic polariton propagation with negative phase velocity. *Nature Photon.* **9**, 674–678 (2015).

[81] Dai, S. et al. Subdiffractional focusing and guiding of polaritonic rays in a natural hyperbolic material. *Nature Commun.* **6**, 6963 (2015).

[82] Li, P. et al. Hyperbolic phonon-polaritons in boron nitride for near-field optical imaging and focusing. *Nature Commun.* **6**, 7507 (2015).

[83] Geick, R., Perry, C. & Rupprecht, G. Normal Modes in Hexagonal Boron Nitride. *Physical Review* **146**, 543–547 (1966).

[84] Dai, S. et al. Tunable phonon polaritons in atomically thin van der Waals crystals of boron nitride. *Science* **343**, 1125–1129 (2014).

[85] Li, Y. et al. Graphene plasmon enhanced vibrational sensing of surface- adsorbed layers. *Nano Lett.* **14**, 1573–1577 (2014).

[86] Thongrattanasiri, S., Koppens, F. H. L. & García de Abajo, F. J. Complete Optical Absorption in Periodically Patterned Graphene. *Phys. Rev. Lett.* **108**, 047401 (2012).

[87] Freitag, M. et al. Photocurrent in graphene harnessed by tunable intrinsic plasmons. *Nature Commun.* **4**, 1951 (2013).

[88] Liu, Y., Willis, R. F., Emtsev, K. V. & Seyller, T. Plasmon dispersion and damping in electrically isolated two-dimensional charge sheets. *Phys. Rev. B* **78**, 201403 (2008).

[89] Eberlein, T. et al. Plasmon spectroscopy of free-standing graphene films. *Phys. Rev. B* **77**, 233406 (2008).

[90] Zhou, W. et al. Atomically localized plasmon enhancement in monolayer graphene. *Nature Nanotech.* **7**, 161–165 (2012).

[91] Brar, V. W., Jang, M. S., Sherrott, M., Lopez, J. J. & Atwater, H. a. Highly confined tunable mid-infrared plasmonics in graphene nanoresonators. *Nano Lett.* **13**, 2541–7 (2013).

[92] Jang, M. S. et al. Tunable large resonant absorption in a midinfrared graphene Salisbury screen. *Phys. Rev. B* **90**, 165409 (2014).

[93] Fang, Z. et al. Gated tunability and hybridization of localized plasmons in nanostructured graphene. *ACS Nano* **7**, 2388–95 (2013).

[94] Brar, V. W. et al. Hybrid Surface-Phonon-Plasmon Polariton Modes in Graphene/Monolayer h-BN Heterostructures. *Nano Lett.* **14**, 3876–3880 (2014).

[95] Fei, Z. et al. Infrared nanoscopy of dirac plasmons at the graphene-SiO2 interface. *Nano Lett.* **11**, 4701–4705 (2011).

[96] Fei, Z. et al. Electronic and plasmonic phenomena at graphene grain boundaries. *Nature Nanotech.* **8**, 821–825 (2013).

[97] Chen, J. et al. Strong plasmon reflection at nanometer-size gaps in monolayer graphene on SiC. *Nano Lett.* **13**, 6210–6215 (2013).

[98] Alonso-González, P. et al. Controlling graphene plasmons with resonant metal antennas and spatial conductivity patterns. *Science* **344**, 1369–1373 (2014).

[99] Schnell, M., Carney, P. S. & Hillenbrand, R. Synthetic optical holography for rapid nanoimaging. *Nature Commun.* **5**, 3499 (2014).

[100] Woessner, A. et al. Highly confined low-loss plasmons in graphene–boron nitride heterostructures. *Nature Mater.* **14**, 421–425 (2015).

[101] Nikitin, A. Y. et al. Real-space mapping of tailored sheet and edge plasmons in graphene nanoresonators. *Nature Photon.* **10**, 239–243 (2016).

[102] Ni, G. X. et al. Ultrafast optical switching of infrared plasmon polaritons in high-mobility graphene. *Nature Photon.* **10**, 244–247 (2016).

[103] Shi, Z. et al. Observation of a Luttinger-liquid plasmon in metallic single-walled carbon nanotubes. *Nature Photon.* **9**, 515–519 (2015).

[104] Goncalves, P. A. D. & Peres, N. M. R. *An Introduction to Graphene Plasmonics* (World Scientific, Singapore, 2016).

[105] Born, M. & Wolf, E. *Principles of Optics* (Cambridge Univ. Press, Cambridge, 1999), 7th edn.

[106] Markoš, P. & Soukoulis, C. M. *Wave Propagation: From Electrons to Photonic Crystals and Left-Handed Materials* (Princeton University Press, Princeton, NJ, 2008).

[107] Zhan, T., Shi, X., Dai, Y., Liu, X. & Zi, J. Transfer matrix method for optics in graphene layers. *J. Phys. Condens. Matter* **25**, 215301 (2013).

[108] Lundeberg, M. B. Transfer matrix method calculator background. *unpublished* (2016).

[109] Palik, E. D. *Handbook of Optical Constants of Solids* (Elsevier, New York, 1997).

[110] Principi, A., Vignale, G., Carrega, M. & Polini, M. Impact of disorder on Dirac plasmon losses. *Phys. Rev. B* **88**, 121405 (2013).

[111] Principi, A. et al. Plasmon losses due to electron-phonon scattering: The case of graphene encapsulated in hexagonal boron nitride. *Phys. Rev. B* **90**, 165408 (2014).

[112] Principi, A., Vignale, G., Carrega, M. & Polini, M. Intrinsic lifetime of Dirac plasmons in graphene. *Phys. Rev. B* **88**, 195405 (2013).

[113] Yang, H. U., Hebestreit, E., Josberger, E. E. & Raschke, M. B. A cryogenic scattering-type scanning near-field optical microscope. *Rev. Sci. Instrum.* **84** (2013).

[114] Huber, A. J., Keilmann, F., Wittborn, J., Aizpurua, J. & Hillenbrand, R. Terahertz near-field nanoscopy of mobile carriers in single semiconductor nanodevices. *Nano Lett.* **8**, 3766–3770 (2008).

[115] Hecht, B., Bielefeldt, H., Novotny, L., Inouye, Y. & Pohl, D. Local Excitation, Scattering, and Interference of Surface Plasmons. *Phys. Rev. Lett.* **77**, 1889–1892 (1996).

[116] Alonso-González, P. et al. Acoustic terahertz graphene plasmons revealed by photocurrent nanoscopy. *Nature Nanotech.* **12**, 31–35 (2016).

[117] Ocelic, N., Huber, A. & Hillenbrand, R. Pseudoheterodyne detection for background-free near-field spectroscopy. *Appl. Phys. Lett.* **89**, 101124 (2006).

[118] Rotenberg, N. & Kuipers, L. Mapping nanoscale light fields. *Nature Photon.* **8**, 919–926 (2014).

[119] Gerber, J. A., Berweger, S., O'Callahan, B. T. & Raschke, M. B. Phase-Resolved Surface Plasmon Interferometry of Graphene. *Phys. Rev. Lett.* **113**, 055502 (2014).

[120] Nikitin, A. Y., Low, T. & Martin-Moreno, L. Anomalous reflection phase of graphene plasmons and its influence on resonators. *Phys. Rev. B* **90**, 041407 (2014).

[121] Fang, Z. et al. Active tunable absorption enhancement with graphene nanodisk arrays. *Nano Lett.* **14**, 299–304 (2014).

[122] Yankowitz, M. et al. Emergence of superlattice Dirac points in graphene on hexagonal boron nitride. *Nature Phys.* **8**, 382–386 (2012).

[123] Tomadin, A., Guinea, F. & Polini, M. Generation and morphing of plasmons in graphene superlattices. *Phys. Rev. B* **90**, 10 (2014).

[124] Ni, G. X. et al. Plasmons in graphene moiré superlattices. *Nature Mater.* **14**, 1217–1222 (2015).

[125] Poddubny, A., Iorsh, I., Belov, P. & Kivshar, Y. Hyperbolic metamaterials. *Nature Photon.* **7**, 948–957 (2013).

[126] Ju, L. et al. Photoinduced doping in heterostructures of graphene and boron nitride. *Nature Nanotech.* **9**, 348–52 (2014).

[127] Zhang, L., Fu, X. & Yang, J. Excitation of Propagating Plasmons in Semi-Infinite Graphene Layer by Free Space Photons. *Commun. Theor. Phys.* **61**, 751–754 (2014).

[128] Johnson, P. B. P. & Christy, R. W. Optical constants of the noble metals. *Phys. Rev. B* **6**, 4370–4379 (1972).

[129] McLeod, A. S. et al. Nanotextured phase coexistence in the correlated insulator V2O3. *Nature Phys.* (2016).

[130] Li, Y. et al. Graphene plasmon enhanced vibrational sensing of surface-adsorbed layers. *Nano Lett.* **14**, 1573–1577 (2014).

[131] Nikitin, A. Y., Guinea, F., Garcia-Vidal, F. J. & Martin-Moreno, L. Surface plasmon enhanced absorption and suppressed transmission in periodic arrays of graphene ribbons. *Phys. Rev. B* **85**, 081405(R) (2012).

[132] Huidobro, P. A., Nikitin, A. Y., González-Ballestero, C., Martín-Moreno, L. & García-Vidal, F. J. Superradiance mediated by graphene surface plasmons. *Phys. Rev. B* **85**, 155438 (2012).

[133] Dickey, F. M. *Laser Beam Shaping: Theory and Techniques* (CRC Press, Boca Raton, 2014), 2nd ed. edn.

[134] Pendry, J. B., Schurig, D. & Smith, D. R. Controlling Electromagnetic Fields. *Science* **312**, 1780–1782 (2006).

[135] Sun, J., Timurdogan, E., Yaacobi, A., Hosseini, E. S. & Watts, M. R. Large-scale nanophotonic phased array. *Nature* **493**, 195–9 (2013).

[136] Takeda, M., Ina, H. & Kobayashi, S. Fourier-transform method of fringe-pattern analysis for computer-based topography and interferometry. *J. Opt. Soc. Am.* **72**, 156 (1982).

[137] Reed, G. T., Mashanovich, G., Gardes, F. Y. & Thomson, D. J. Silicon optical modulators. *Nature Photon.* **4**, 518–526 (2010).

[138] Liu, K., Ye, C. R., Khan, S. & Sorger, V. J. Review and perspective on ultrafast wavelength-size electro-optic modulators. *Laser Photon. Rev.* **9**, 172–194 (2015).

[139] Miller, D. A. B. Attojoule Optoelectronics for Low-Energy Information Processing and Communications – a Tutorial Review. *J. Lightwave Technol.* **4088**, 1–1 (2017).

[140] Kildishev, A. V., Boltasseva, A. & Shalaev, V. M. Planar Photonics with Metasurfaces. *Science* **339**, 1232009 (2013).

[141] Dionne, J., Diest, K., Sweatlock, L. & Atwater, H. PlasMOStor: a metal-oxide-Si field effect plasmonic modulator. *Nano Lett.* **9**, 897 (2009).

[142] Mohsin, M. et al. Experimental verification of electro-refractive phase modulation in graphene. *Sci. Rep.* **5**, 10967 (2015).

[143] Sun, Z., Martinez, A. & Wang, F. Optical modulators with 2D layered materials. *Nature Photon.* **10**, 227–238 (2016).

[144] Huber, A., Ocelic, N., Kazantsev, D. & Hillenbrand, R. Near-field imaging of mid-infrared surface phonon polariton propagation. *Appl. Phys. Lett.* **87**, 16–18 (2005).

[145] Torre, I., Katsnelson, M. I., Diaspro, A., Pellegrini, V. & Polini, M. Lippmann-Schwinger theory for two-dimensional plasmon scattering. *arXiv* 1702.04925 (2017).

[146] Wang, G., Liu, X., Lu, H. & Zeng, C. Graphene plasmonic lens for manipulating energy flow. *Sci. Rep.* **4**, 1–7 (2014).

[147] Phillips, P. L., Knight, J. C., Pottage, J. M., Kakarantzas, G. & Russell, P. S. J. Direct measurement of optical phase in the near field. *Appl. Phys. Lett.* **76**, 541 (2000).

[148] Balistreri, M. L. M., Korterik, J. P., Kuipers, L. & Van Hulst, N. F. Local observations of phase singularities in optical fields in waveguide structures. *Phys. Rev. Lett.* **85**, 294–297 (2000).

[149] Li, Z. et al. Graphene Plasmonic Metasurfaces to Steer Infrared Light. *Sci. Rep.* **5**, 12423 (2015).

[150] Polini, M. et al. Plasmons and the spectral function of graphene. *Phys. Rev. B* **77**, 81411 (2008).

[151] Liu, M.-H. Theory of carrier density in multigated doped graphene sheets with quantum correction. *Phys. Rev. B* **87**, 125427 (2013).

[152] Garcia-Pomar, J. L., Nikitin, A. Y. & Martin-Moreno, L. Scattering of graphene plasmons by defects in the graphene sheet. *ACS Nano* **7**, 4988–4994 (2013).

[153] Haffner, C. et al. All-plasmonic Mach–Zehnder modulator enabling optical high-speed communication at the microscale. *Nature Photon.* **9**, 525–528 (2015).

[154] Tielrooij, K. J. et al. Electrical control of optical emitter relaxation pathways enabled by graphene. *Nature Phys.* **11**, 281–287 (2015).

[155] Wang, Z. et al. Experimental demonstration of graphene plasmons working close to the near-infrared window. *Opt. Lett.* **41**, 5345 (2016).

[156] Gómez-Díaz, J. S. & Perruisseau-Carrier, J. Graphene-based plasmonic switches at near infrared frequencies. *Opt. Express* **21**, 15490 (2013).

[157] Bonaccorso, F., Sun, Z., Hasan, T. & Ferrari, A. C. Graphene Photonics and Optoelectronics. *Nature Photon.* **4**, 611–622 (2010).

[158] Koppens, F. H. L. et al. Photodetectors based on graphene, other two-dimensional materials and hybrid systems. *Nature Nanotech.* **9**, 780–793 (2014).

[159] Xia, F., Mueller, T., Lin, Y.-m., Valdes-Garcia, A. & Avouris, P. Ultrafast graphene photodetector. *Nature Nanotech.* **4**, 839–843 (2009).

[160] Konstantatos, G. et al. Hybrid graphene-quantum dot phototransistors with ultra-high gain. *Nature Nanotech.* **7**, 363–368 (2012).

[161] Liu, N. et al. Large-Area, Transparent, and Flexible Infrared Photodetector Fabricated Using P-N Junctions Formed by N-Doping Chemical Vapor Deposition Grown Graphene. *Nano Lett.* **14**, 3702–3708 (2014).

[162] Gabor, N. M. et al. Hot carrier-assisted intrinsic photoresponse in graphene. *Science* **334**, 648–52 (2011).

[163] Herring, P. K. et al. Photoresponse of an electrically tunable ambipolar graphene infrared thermocouple. *Nano Lett.* **14**, 901–907 (2014).

[164] Badioli, M. et al. Phonon-Mediated Mid-Infrared Photoresponse of Graphene. *Nano Lett.* **14**, 6374–6381 (2014).

[165] Xu, X., Gabor, N. M., Alden, J. S., van der Zande, A. M. & McEuen, P. L. Photo-Thermoelectric Effect at a Graphene Interface Junction. *Nano Lett.* **10**, 562–566 (2009).

[166] Lemme, M. C. et al. Gate-Activated Photoresponse in a Graphene p–n Junction. *Nano Lett.* **11**, 4134–4137 (2011).

[167] Song, J. C. W., Rudner, M. S., Marcus, C. M. & Levitov, L. S. Hot carrier transport and photocurrent response in graphene. *Nano Lett.* **11**, 4688–4692 (2011).

[168] Song, J. C. W. & Levitov, L. S. Shockley-Ramo theorem and long-range photocurrent response in gapless materials. *Phys. Rev. B* **90**, 075415 (2014).

[169] Cutler, M. & Mott, N. F. Observation of Anderson localization in an electron gas. *Phys. Rev.* **181**, 1336–1340 (1969).

[170] Zuev, Y. M., Chang, W. & Kim, P. Thermoelectric and Magnetothermoelectric Transport Measurements of Graphene. *Phys. Rev. Lett.* **102**, 96807 (2009).

[171] Kampfrath, T., Perfetti, L., Schapper, F., Frischkorn, C. & Wolf, M. Strongly coupled optical phonons in the ultrafast dynamics of the electronic energy and current relaxation in graphite. *Phys. Rev. Lett.* **95**, 26–29 (2005).

[172] Hesp, N. C. Hot-carrier dynamics in hBN-encapsulated graphene. *ICFO - The Institute of Photonic Sciences* Master thesis (2016).

[173] Low, T., Perebeinos, V., Kim, R., Freitag, M. & Avouris, P. Cooling of photoexcited carriers in graphene by internal and substrate phonons. *Phys. Rev. B* **86**, 1–15 (2012).

[174] Principi, A. et al. Super-Planckian electron cooling in a van der Waals stack. *arXiv* 1608.01516 (2016).

[175] Betz, A. C. et al. Supercollision cooling in undoped graphene. *Nature Phys.* **9**, 109–112 (2012).

[176] Graham, M. W., Shi, S.-F., Ralph, D. C., Park, J. & McEuen, P. L. Photocurrent measurements of supercollision cooling in graphene. *Nature Phys.* **9**, 103–108 (2012).

[177] Song, J. C. W., Reizer, M. Y. & Levitov, L. S. Disorder-Assisted Electron-Phonon Scattering and Cooling Pathways in Graphene. *Phys. Rev. Lett.* **109**, 106602 (2012).

[178] Bistritzer, R. & MacDonald, A. H. Electronic Cooling in Graphene. *Phys. Rev. Lett.* **102**, 206410 (2009).

[179] Yan, J. et al. Dual-gated bilayer graphene hot-electron bolometer. *Nature Nanotech.* **7**, 472–478 (2012).

[180] Freitag, M. et al. Substrate-sensitive mid-infrared photoresponse in graphene. *ACS Nano* **8**, 8350–8356 (2014).

[181] Yao, Y. et al. High responsivity mid infrared graphene detectors with antenna enhanced photocarrier generation and collection. *Nano Lett.* **14**, 3749–3754 (2014).

[182] Hsu, A. L. et al. Graphene-Based Thermopile for Thermal Imaging Applications. *Nano Lett.* **15**, 7211–7216 (2015).

[183] Duong, D. L. et al. Probing graphene grain boundaries with optical microscopy. *Nature* **490**, 235–239 (2012).

[184] Yu, Q. et al. Control and characterization of individual grains and grain boundaries in graphene grown by chemical vapour deposition. *Nature Mater.* **10**, 443–449 (2011).

[185] Huang, P. Y. et al. Grains and grain boundaries in single-layer graphene atomic patchwork quilts. *Nature* **469**, 389–92 (2011).

[186] Yasaei, P. et al. Bimodal Phonon Scattering in Graphene Grain Boundaries. *Nano Lett.* **15**, 4532–4540 (2015).

[187] Deshpande, A., Bao, W., Miao, F., Lau, C. & LeRoy, B. Spatially resolved spectroscopy of monolayer graphene on SiO2. *Phys. Rev. B* **79**, 205411 (2009).

[188] Gibertini, M., Tomadin, A., Guinea, F., Katsnelson, M. I. & Polini, M. Electron-hole puddles in the absence of charged impurities. *Phys. Rev. B* **85**, 201405 (2012).

[189] Cho, S. et al. Thermoelectric imaging of structural disorder in epitaxial graphene. *Nature Mater.* **12**, 913–918 (2013).

[190] Ferrari, A. C. & Basko, D. M. Raman spectroscopy as a versatile tool for studying the properties of graphene. *Nature Nanotech.* **8**, 235–246 (2013).

[191] Mueller, T., Xia, F., Freitag, M., Tsang, J. & Avouris, P. Role of contacts in graphene transistors: A scanning photocurrent study. *Phys. Rev. B* **79**, 245430 (2009).

[192] Mauser, N. & Hartschuh, A. Tip-enhanced near-field optical microscopy. *Chem. Soc. Rev.* **43**, 1248–1262 (2014).

[193] Mauser, N. et al. Antenna-enhanced optoelectronic probing of carbon nanotubes. *Nano Lett.* **14**, 3773–3778 (2014).

[194] Grover, S., Dubey, S., Mathew, J. P. & Deshmukh, M. M. Limits on the bolometric response of graphene due to flicker noise. *Appl. Phys. Lett.* **106**, 051113 (2015).

[195] Woessner, A. et al. Near-field photocurrent nanoscopy on bare and encapsulated graphene. *Nature Commun.* **7**, 10783 (2016).

[196] Li, X. et al. Large-Area Synthesis of High-Quality and Uniform Graphene Films on Copper Foils. *Science* **324**, 1312–1314 (2009).

[197] Reina, A. et al. Large area, few-layer graphene films on arbitrary substrates by chemical vapor deposition. *Nano Lett.* **9**, 30–35 (2009).

[198] Bae, S. et al. Roll-to-roll production of 30-inch graphene films for transparent electrodes. *Nature Nanotech.* **5**, 574–578 (2010).

[199] Bonaccorso, F. et al. Production and processing of graphene and 2d crystals. *Mater. Today* **15**, 564–589 (2012).

[200] Ren, W. & Cheng, H.-M. The global growth of graphene. *Nature Nanotech.* **9**, 726–730 (2014).

[201] Lee, J.-H. J.-H. et al. Wafer-Scale Growth of Single-Crystal Monolayer Graphene on Reusable Hydrogen-Terminated Germanium. *Science* **344**, 286–289 (2014).

[202] Gao, L. et al. Face-to-face transfer of wafer-scale graphene films. *Nature* **505**, 190–194 (2014).

[203] de Heer, W. a. et al. Large area and structured epitaxial graphene produced by confinement controlled sublimation of silicon carbide. *Proc. Natl. Acad. Sci.* **108**, 16900–16905 (2011).

[204] Akinwande, D., Petrone, N. & Hone, J. Two-dimensional flexible nanoelectronics. *Nature Commun.* **5**, 5678 (2014).

[205] Yazyev, O. V. & Louie, S. G. Electronic transport in polycrystalline graphene. *Nature Mater.* **9**, 806–9 (2010).

[206] Cummings, A. W. et al. Charge transport in polycrystalline graphene: challenges and opportunities. *Adv. Mater.* **26**, 5079–5094 (2014).

[207] Yazyev, O. V. & Chen, Y. P. Polycrystalline graphene and other two-dimensional materials. *Nature Nanotech.* **9**, 755–767 (2014).

[208] Zhang, Y., Brar, V. W., Girit, C., Zettl, A. & Crommie, M. F. Origin of spatial charge inhomogeneity in graphene. *Nature Phys.* **5**, 722–726 (2009).

[209] Decker, R. et al. Local electronic properties of graphene on a BN substrate via scanning tunneling microscopy. *Nano Lett.* **11**, 2291–2295 (2011).

[210] Burson, K. M. et al. Direct imaging of charged impurity density in common graphene substrates. *Nano Lett.* **13**, 3576–3580 (2013).

[211] Kretinin, A. V. et al. Electronic properties of graphene encapsulated with different two-dimensional atomic crystals. *Nano Lett.* **14**, 3270–3276 (2014).

[212] Chen, S. Y., Ho, P. H., Shiue, R. J., Chen, C. W. & Wang, W. H. Transport/magnetotransport of high-performance graphene transistors on organic molecule-functionalized substrates. *Nano Lett.* **12**, 964–969 (2012).

[213] Tsen, A. W. et al. Tailoring electrical transport across grain boundaries in polycrystalline graphene. *Science* **336**, 1143–1146 (2012).

[214] Van Tuan, D. et al. Scaling properties of charge transport in polycrystalline graphene. *Nano Lett.* **13**, 1730–1735 (2013).

[215] Wei, P., Bao, W., Pu, Y., Lau, C. N. & Shi, J. Anomalous thermoelectric transport of dirac particles in graphene. *Phys. Rev. Lett.* **102**, 1–4 (2009).

[216] Lee, E. J. H., Balasubramanian, K., Weitz, R. T., Burghard, M. & Kern, K. Contact and edge effects in graphene devices. *Nature Nanotech.* **3**, 486–490 (2008).

[217] Ben Shalom, M. et al. Quantum oscillations of the critical current and high-field superconducting proximity in ballistic graphene. *Nature Phys.* **12**, 318–322 (2015).

[218] Allen, M. T. et al. Spatially resolved edge currents and guided-wave electronic states in graphene. *Nature Phys.* **12**, 128–133 (2015).

[219] Torre, I., Tomadin, A., Krahne, R., Pellegrini, V. & Polini, M. Electrical plasmon detection in graphene waveguides. *Phys. Rev. B* **91**, 081402(R) (2014).

[220] Gramotnev, D. K. & Bozhevolnyi, S. I. Plasmonics beyond the diffraction limit. *Nature Photon.* **4**, 83–91 (2010).

[221] Dyakonov, M. & Shur, M. Detection, mixing, and frequency multiplication of terahertz radiation by two-dimensional electronic fluid. *IEEE Trans. Electron Dev.* **43**, 380–387 (1996).

[222] Ditlbacher, H. et al. Organic diodes as monolithically integrated surface plasmon polariton detectors. *Appl. Phys. Lett.* **89**, 161101 (2006).

[223] Neutens, P., Van Dorpe, P., De Vlaminck, I., Lagae, L. & Borghs, G. Electrical detection of confined gap plasmons in metal–insulator–metal waveguides. *Nature Photon.* **3**, 283–286 (2009).

[224] Falk, A. L. et al. Near-field electrical detection of optical plasmons and single-plasmon sources. *Nature Phys.* **5**, 475–479 (2009).

[225] Heeres, R. W. et al. On-chip single plasmon detection. *Nano Lett.* **10**, 661–664 (2010).

[226] Dufaux, T., Dorfmüller, J., Vogelgesang, R., Burghard, M. & Kern, K. Surface plasmon coupling to nanoscale Schottky-type electrical detectors. *Appl. Phys. Lett.* **97**, 1–4 (2010).

[227] Goykhman, I., Desiatov, B., Khurgin, J. & Shappir. . . , J. Locally Oxidized Silicon Surface-Plasmon Schottky Detector for Telecom Regime. *Nano Lett.* 2219–2224 (2011).

[228] Goodfellow, K. M., Chakraborty, C., Beams, R., Novotny, L. & Vamivakas, A. N. Direct On-Chip Optical Plasmon Detection with an Atomically Thin Semiconductor. *Nano Lett.* **15**, 5477–5481 (2015).

[229] Brongersma, M. L., Halas, N. J. & Nordlander, P. Plasmon-induced hot carrier science and technology. *Nature Nanotech.* **10**, 25–34 (2015).

[230] Innes, R. & Sambles, J. Simple thermal detection of surface plasmon-polaritons. *Solid State Commun.* **56**, 493–496 (1985).

[231] Weeber, J. C. et al. Thermo-electric detection of waveguided surface plasmon propagation. *Appl. Phys. Lett.* **99** (2011).

[232] Cai, X. et al. Plasmon-Enhanced Terahertz Photodetection in Graphene. *Nano Lett.* **15**, 4295–4302 (2015).

[233] Lundeberg, M. B. et al. Thermoelectric detection and imaging of propagating graphene plasmons. *Nature Mater.* **16**, 204–207 (2017).

[234] Diaconescu, B. et al. Low-energy acoustic plasmons at metal surfaces. *Nature* **448**, 57–59 (2007).

[235] Principi, A., Asgari, R. & Polini, M. Acoustic plasmons and composite hole-acoustic plasmon satellite bands in graphene on a metal gate. *Solid State Commun.* **151**, 1627–1630 (2011).

[236] Stauber, T. & Gómez-Santos, G. Plasmons in layered structures including graphene. *New J. Phys.* **14**, 105018 (2012).

[237] Gu, X., Lin, I.-T. & Liu, J.-M. Extremely confined terahertz surface plasmon-polaritons in graphene-metal structures. *Appl. Phys. Lett.* **103**, 071103 (2013).

[238] Svintsov, D., Devizorova, Z., Otsuji, T. & Ryzhii, V. Plasmons in tunnel-coupled graphene layers: Backward waves with quantum cascade gain. *Phys. Rev. B* **94**, 115301 (2016).

[239] Giles, A. J. J. et al. Imaging of Anomalous Internal Reflections of Hyperbolic Phonon-Polaritons in Hexagonal Boron Nitride. *Nano Lett.* **16**, 3858–3865 (2016).

[240] Liang, X. et al. Toward clean and crackless transfer of graphene. *ACS Nano* **5**, 9144–9153 (2011).

[241] Sassi, U. et al. Graphene-based mid-infrared room-temperature pyroelectric bolometers with ultrahigh temperature coefficient of resistance. *Nature Commun.* **8**, 14311 (2017).

[242] Gopalan, K. K. et al. Mid-Infrared Pyroresistive Graphene Detector on LiNbO_3. *Adv. Optical Mater.* 1600723 (2017).

[243] Huber, A. J., Deutsch, B., Novotny, L. & Hillenbrand, R. Focusing of surface phonon polaritons. *Appl. Phys. Lett.* **92**, 203104 (2008).

[244] Wu, J.-S., Basov, D. N. & Fogler, M. M. Topological insulators are tunable waveguides for hyperbolic polaritons. *Phys. Rev. B* **92**, 205430 (2015).

[245] Woessner, A. et al. Electrical detection of hyperbolic phonon-polaritons in heterostructures of graphene and boron nitride. *unpublished* (2017).

[246] Alù, A., Engheta, N., Alu, A. & Engheta, N. Tuning the scattering response of optical nanoantennas with nanocircuit loads. *Nature Photon.* **2**, 307–310 (2008).

[247] Heerema, S. J. & Dekker, C. Graphene nanodevices for DNA sequencing. *Nature Nanotech.* **11**, 127–136 (2016).

[248] Ooi, K. J. A., Chu, H. S., Hsieh, C. Y., Tan, D. T. H. & Ang, L. K. Highly Efficient Midinfrared On-Chip Electrical Generation of Graphene Plasmons by Inelastic Electron Tunneling Excitation. *Phys. Rev. Applied* **3**, 054001 (2015).

[249] Duke, C. B. Plasmon excitation by electron tunneling. *Physical Review* **186**, 588–590 (1969).

[250] Duke, C. B., Rice, M. J. & Steinrisser, F. Tunneling measurement of electron-plasmon interaction in degenerate semiconductors. *Phys. Rev.* **181**, 733–742 (1969).

[251] Tsui, D. C. Observations of Surface Plasmon Excitation by Tunneling Electrons in GaAs-Pb Tunnel Junctions. *Phys. Rev. Lett.* **22**, 293–295 (1969).

[252] Tsui, D. C. & Barker, a. S. Surface-plasmon excitation by tunneling electrons in GaAs-Pb Tunnel junctions. *Physical Review* **186**, 590–591 (1969).

[253] Economou, E. N. & Ngai, K. L. Surface-plasmon excitation by electron tunneling. *Phys. Rev. B* **4**, 4105–4108 (1971).

[254] Bharadwaj, P., Bouhelier, A. & Novotny, L. Electrical excitation of surface plasmons. *Phys. Rev. Lett.* **106**, 1–4 (2011).

[255] Britnell, L. et al. Resonant tunnelling and negative differential conductance in graphene transistors. *Nature Commun.* **4**, 1794 (2013).

[256] Jin, D. et al. Topological magnetoplasmon. *Nature Commun.* **7**, 13486 (2016).

[257] Pan, D., Yu, R., Xu, H. & de Abajo, F. J. G. Topologically protected Dirac plasmons in graphene. *arXiv* 1702.00036 (2017).

[258] Jin, D. et al. Infrared Topological Plasmons in Graphene. *arXiv* 1702.02553 (2017).

[259] Cai, Y., Zhang, L., Zeng, Q., Cheng, L. & Xu, Y. Infrared reflectance spectrum of BN calculated from first principles. *Solid State Commun.* **141**, 262–266 (2007).